NASA Technical Memorandum 103856

IN-34
48395
P87

The Three-Dimensional Evolution of a Plane Mixing Layer
Part 1. The Kelvin-Helmholtz Roll-Up

Michael M. Rogers and Robert D. Moser

(NASA-TM-103856) THE THREE-DIMENSIONAL
EVOLUTION OF A PLANE MIXING LAYER. PART 1:
THE KELVIN-HELMHOLTZ ROLL-UP (NASA) 87 p
CSCL 20D
N92-11303
Unclas
G3/34 0048395

September 1991

NASA
National Aeronautics and
Space Administration

NASA Technical Memorandum 103856

The Three-Dimensional Evolution of a Plane Mixing Layer
Part 1. The Kelvin-Helmholtz Roll-Up

Michael M. Rogers and Robert D. Moser, Ames Research Center, Moffett Field, California

September 1991

National Aeronautics and
Space Administration

Ames Research Center
Moffett Field, California 94035-1000

CONTENTS

SUMMARY

The Kelvin–Helmholtz roll-up of three-dimensional, temporally evolving, plane mixing layers has been simulated numerically. All simulations were begun from a few low-wavenumber disturbances, usually derived from linear stability theory, in addition to the mean velocity profile. The spanwise disturbance wavelength was taken to be less than or equal to the streamwise wavelength associated with the Kelvin–Helmholtz roll-up. A standard set of "clean" structures develop in most of the simulations. The spanwise vorticity rolls up into a corrugated spanwise roller, with vortex stretching creating strong spanwise vorticity in a cup-shaped region at the bends of the roller. Predominantly streamwise rib vortices develop in the braid region between the rollers. For sufficiently strong initial three-dimensional disturbances, these ribs "collapse" into compact axisymmetric vortices. The rib vortex lines connect to neighboring ribs and are kinked in the opposite direction of the roller vortex lines. Because of this, these two sets of vortex lines remain distinct. For certain initial conditions, persistent ribs do not develop. In such cases the development of significant three-dimensionality is delayed. When the initial three-dimensional disturbance energy is about equal to, or less than, the two-dimensional fundamental disturbance energy, the evolution of the three-dimensional disturbance is nearly linear (with respect to the mean and the two-dimensional disturbances), at least until the first Kelvin–Helmholtz roll-up is completed. This includes cases in which the three-dimensional disturbance is strong enough to result in "collapsed" rib vortices of the type visualized in experiments. Because of this, the evolution of infinitesimal three-dimensional perturbations on the developing two-dimensional base flow contains many of the same features present in the full three-dimensional simulations. Nonlinear effects are important in the rib collapse process, in the generation of the strong cup vorticity at the bends of the roller, and late in the flow evolution after the two-dimensional modes have saturated. The appearance of collapsed rib vortices and strong cup vorticity will be shown in Part 2 of this report (to be published as a NASA TM) to be the first step in the transition to turbulence.

1 INTRODUCTION

The mixing layer that forms between two fluid streams moving with different velocities is an important model problem for the study of turbulence in free shear layers. It is particularly interesting in the context of scalar mixing and chemical reaction since many practical chemically reacting flows are free shear flows. However, here we are concerned with the hydrodynamic evolution of an incompressible plane mixing layer in the belief that a thorough understanding of the hydrodynamics is a prerequisite to the study of scalar mixing in such a flow.

1.1 Experimental Observations

A variety of experimental studies have shown that the spatially developing mixing layer starting at the trailing edge of a splitter-plate between two streams is dominated by large, predominantly two-dimensional, spanwise vortex structures that arise from the Kelvin–Helmholtz instability of the layer. These two-dimensional structures have been observed even at very high Reynolds numbers in fully turbulent mixing layers (Brown and Roshko 1971, 1974). Dye visualizations in water by Winant and Browand (1974) demonstrated that the spreading of the mixing layer was due primarily to pairing, the co-rotation and merging of individual spanwise vortices created by the initial Kelvin–Helmholtz instability or by previous pairings. This mechanism is consistent with the amalgamation process observed by Brown and Roshko (1974) at much higher Reynolds numbers.

The universality of the Brown–Roshko structures has often been questioned. Indeed, in more turbulent environments, mixing-layer evolution can be apparently more complex. Smoke visualizations by Chandrsuda et al. (1978) indicated that more complex pairing processes with significant spanwise variation can also occur, leading to "helical" patterns. Also, dislocations in an otherwise two-dimensional array of spanwise rollers (Browand and Troutt 1980) and highly three-dimensional roller vortices (Nygaard and Glezer 1990) have been observed.

Plan views of turbulent mixing layers by Brown and Roshko (1974), Konrad (1976), and Breidenthal (1981) indicated that a streamwise streaky structure coexisted with the predominantly two-dimensional spanwise rollers. Further investigation of the structures by Bernal (1981) and Bernal and Roshko (1986) confirmed that these streaks were due to pairs of counterrotating, predominantly streamwise vortices (called "ribs," following Hussain (1983)) that form in the so-called braid region between the spanwise rollers. Examination of planes normal to the flow direction by laser-induced fluorescence showed mushroom-shaped patterns resulting from the induced motion of the streamwise vortex pairs. The spanwise location of these streamwise vortices has been found to correlate with upstream disturbances in the experimental facility (Jimenez 1983; Bernal and Roshko 1986; Bell and Mehta 1989a). However, beyond a certain downstream location a reorganization may occur, increasing the characteristic spanwise spacing between "streaks" and apparently uncoupling them from the inlet disturbances (Bernal and Roshko 1986). The circulation of the streamwise rib vortices was estimated by Jimenez (1983) and by Bell and Mehta (1990). Remarkably, they found similar values of this circulation during the early development of the layer ($0.1\Gamma_z$ and $0.07\Gamma_z$, respectively, where Γ_z is the initial spanwise roller circulation).

There have been many recent efforts to study the origin and behavior of the basic structures present in the turbulent mixing layer. Many of these studies have concentrated on the development of three-dimensionality in an essentially laminar mixing layer as a simplified model of mechanisms that may exist in the turbulent case. Since most spatially developing mixing layers are only convectively unstable (Huerre and Monkewitz 1985), they are sensitive to inlet conditions. Several studies have tried to control inlet conditions through forcing (e.g., Ho and Huang 1982; Nygaard and Glezer 1991, Evolution of Streamwise Vortices and Generation of Small-Scale Motion in a Plane Mixing Layer, J. Fluid Mech., in press) or through modification of the splitter-plate (e.g., the corrugated and serrated trailing edges of Lasheras and Choi (1988)). These experiments are typically done in water at low Reynolds numbers and produce "clean," well-ordered structures. Lasheras, Cho and Maxworthy (1986) and Lasheras and Choi (1988) used extensive flow visualization of such clean flows to study the evolution of the streamwise vortices. Their study examines the Kelvin–Helmholtz roll-up into spanwise rollers and the associated streamwise vortex evolution up to the first pairing, beyond which the flow field becomes too complex for their flow-visualization method. In a related investigation at much higher Reynolds number, Huang and Ho (1990) carefully studied the streamwise vortices with the goal of understanding the transition to "random small-scale turbulence."

1.2 Theoretical and Computational Observations

The linear stability of mixing-layer velocity profiles (usually hyperbolic tangent or error function) has been well documented (Michalke 1964; Monkewitz and Huerre 1982; Huerre and Monkewitz 1985). Kelly (1967) and Pierrehumbert and Widnall (1982) found a two-dimensional secondary instability that leads to pairing as observed by Winant and Browand (1974). Recognizing the importance of predicting the instabilities of the two-dimensional Kelvin–Helmholtz rollers to the onset of three-dimensionality, Pierrehumbert and Widnall (1982) used linear theory to examine instabilities of a periodic array of Stuart (1967) vortices. The Stuart vortices, which are solutions to the incompressible Euler equations, provide a reasonable approximation to real mixing layers for certain values of a free parameter. The analysis of Pierrehumbert and Widnall (1982) shows that such an array of vortices is unstable to various three-dimensional disturbances, as well as to the subharmonic pairing disturbance mentioned above. They used the term "translative instability" to describe the instability arising from a three-dimensional disturbance that has the same streamwise wavelength as the two-dimensional fundamental. They also hypothesized that oblique disturbances with the same wavelength as the two-dimensional subharmonic could lead to "helical" pairing. The most unstable spanwise wavelength for their translative instability is two thirds the separation between Kelvin–Helmholtz rollers. However, the growth rate as a function of spanwise wavelength has a broad peak. Corcos and Lin (1984) extended this analysis by studying the three-dimensional instabilities of an evolving two-dimensional base flow, this base flow being computed numerically. Their findings are similar to those of Pierrehumbert and Widnall (1982) in that they predict a wide range of unstable spanwise disturbances.

In another study of three-dimensionality in a mixing layer, Lin and Corcos (1984) computed the behavior of a vortex array being stretched along its axis by a plane strain. This two-dimensional problem is expected to be a good model of the rib vortices in the braid region of the mixing layer, once the Kelvin–Helmholtz roll-up is substantially complete and the braid region has been depleted of spanwise vorticity. This model problem was also attacked analytically by Neu (1984). They found that if the circulation associated with the streamwise rib vortices is large enough (relative to their spanwise spacing and viscosity, see sec. 4.3.1), the streamwise vorticity in the braid region collapses into a compact, roughly axisymmetric vortex. They also showed that it is such collapsed vortices that are responsible for the "streaks" and mushroom shapes observed in the flow-visualization experiments described above. Pullin and Jacobs (1986) simulated the same flow using the contour-dynamics method and found "tertiary instabilities" of the collapsing rib vortices.

Although many numerical studies of the two-dimensional plane mixing layer have been undertaken (e.g., Acton 1976; Patnaik, Sherman, and Corcos 1976; Riley and Metcalfe 1980; Corcos and Sherman 1984), few three-dimensional simulations are available because of their computational expense. Such simulations are usually of time-developing mixing layers rather than the spatially developing mixing layers common in experiments (see sec. 2.1). Pioneering three-dimensional large-eddy simulations of initially turbulent mixing layers were performed by Mansour, Ferziger, and Reynolds (1978) and by Cain, Reynolds, and Ferziger (1981). Spanwise rollers and evidence of rib vortices were observed in both these studies. Mansour, Ferziger, and Reynolds also found that their computed flow fields more closely resembled experimental results when two-dimensional rollers were included in the initial conditions. Riley and Metcalfe (1980) used direct numerical simulation to simulate a few three-dimensional mixing layers through the first roll-up, in addition to the two-dimensional cases mentioned above. They compared cases begun from "turbulent" initial conditions with both a laminar roll-up and with "turbulent" cases that were "forced" by an additional two-dimensional fundamental disturbance. Results were found to be in agreement with laboratory experiments on forced mixing layers.

In recent work by Metcalfe et al. (1987), three-dimensional numerical simulations were used to address many issues of mixing-layer instability as well as to simulate several three-dimensional layers begun from "turbulent" initial conditions. These simulated fields contain many features found in experimental flow visualizations. In particular, the predominantly streamwise rib vortices are found in their computations started both from controlled and "turbulent" initial conditions. In the "turbulent" cases, either two-dimensional eigenfunctions were added to the random initial conditions, or the initial fluctuating energy was very small to allow the most unstable two-dimensional mode to dominate through a long linear development. In either case, the effect was the same as the explicit two-dimensional rollers added to the simulations of Mansour, Ferziger, and Reynolds and the "forcing" used by Riley and Metcalfe.

The more difficult computational task of simulating spatially evolving shear layers (see sec. 2.1) was undertaken by Lowery and Reynolds (1986) and by Buell and Mansour (1989a, 1989b). Some of the simulations by Lowery and Reynolds were made with "turbulent" inlet conditions. These simulations have been used to isolate two-dimensional, spatially developing effects like the phase decorrelation of a forced mixing layer after the first pairing (Ho et al. 1988), and for detailed comparison of spatially and temporally evolving mixing layers (see sec. 2.1, and Buell, Moser, and Rogers, to be published). The greater difficulty of spatially developing mixing layer simulations has limited these studies to low Reynolds numbers.

The computations described above used primarily spectral methods in Eulerian reference frames. An alternative means of simulating three-dimensional mixing layers was used by Ashurst and Meiburg (1988). They examined the development of an inviscid mixing layer by discretizing the vorticity field into vortex filaments and tracking the evolution of these filaments numerically. This is an attractive approach for the mixing layer, because most of the early development is driven by inviscid mechanisms. Their computations reproduced the experimentally observed rib vortices and indicated that the roller is only mildly three-dimensional.

1.3 Unanswered Questions

Despite the extensive research that has been directed at the plane mixing layer in the past 20 years, many important unanswered questions remain; some of them are described below. Of particular interest in the current work is the early development of the mixing layer. Although the "standard" structures (rib vortices and spanwise rollers) have been observed in many experimental and numerical studies, the details of these structures and how they interact are not known. For example, the way in which the rib vortices are connected to the spanwise rollers has been a matter of great speculation (Hussain 1983; Bernal and Roshko 1986). Also, the degree to which the spanwise roller becomes three-dimensional and how this three-dimensionality occurs is not well understood. Virtually nothing is known about the evolution of the three-dimensional ribs and rollers during a pairing. Moreover, the mechanism by which a laminar mixing layer ultimately becomes turbulent has not been determined.

Another matter of concern is the apparent contradiction between the known sensitivity of the mixing layer to inlet or initial conditions, and the experimental and numerical observations of a standard set of structures. This has led to the speculation that experimental facilities may have similar disturbance environments. However, alternative flow developments have been identified (e.g., Chandrsuda et al. 1978; Browand and Troutt 1980), and the extent to which the standard structures are robust to changes in inlet conditions is not known.

There has also been disagreement as to whether the "secondary instability," which leads to the formation of rib vortices and three-dimensionality, is a "core instability" or a "braid instability." Some investigators, such as Nygaard and Glezer (1990), view the ribs as a consequence of the bending roller core. Others, such as Ashurst and Meiburg (1988), Lasheras and Choi (1988), and Bell and Mehta (1989b), conclude that the ribs arise from a braid region instability related to the mechanism investigated by Lin and Corcos (1984).

The work described here and in Part 2 of this report (to be published as a NASA TM) was undertaken to address these questions. In this paper, we investigate the initial roll-up of the mixing layer and the development of three-dimensionality. In Part 2, the effects of pairing and the transition to turbulence are examined. Some preliminary results of this study have appeared in Rogers and Moser (1989) and Moser and Rogers (1991).

1.4 Current Approach

The primary tool we have applied to the problems outlined above is direct numerical simulation of the time-developing mixing layer. Numerical simulation has two overwhelming advantages in addressing the questions outlined above. First, the initial (inlet) conditions can be precisely specified, and second, the simulations provide a complete description of the flow field at any time, including velocity and vorticity at all spatial locations.

All of the numerical simulations described both in this paper and in Part 2 were begun from simple low-wavenumber disturbances to the mean profile. They are thus necessarily "clean" initially. It is expected that a thorough understanding of the vortex dynamics of such clean flows will enable one to understand the development of mixing layers in the more general case of uncontrolled disturbances. These flows may be considered to be "deterministic models" of mixing layer development, similar to the work of Corcos and Sherman (1984), Corcos and Lin (1984), and Lin and Corcos (1984). Despite the initially clean nature of these simulated mixing layers (i.e., near the splitter-plate) the flows ultimately become quite complex and in some cases (discussed in Part 2) undergo a transition to turbulence. In such cases the origins of the post-transition flow structures can no longer be traced back to their pre-transition counterparts. Presumably, at this point the exact nature of the initial/inlet condition is largely irrelevant.

It is impossible to explore the entire infinite-dimensional space of possible initial conditions. Therefore, the selection of initial conditions must be guided by their relevance to experimental flows. Initial conditions for the baseline simulations reported here (secs. 3.2 and 4.2) were chosen to correspond to the types of disturbances that are expected in experimental mixing-layer facilities. In this way, a simple computational model of the evolution of a typical mixing layer can be developed. In particular, it is expected that the trailing edge of the splitter-plate will promote predominantly two-dimensional disturbances (Ho and Huerre 1984), and such disturbances are included in the initial conditions. Also, wind-tunnel imperfections are expected to introduce streamwise vorticity into the splitter-plate boundary layers (Jimenez 1983; Bernal and Roshko 1986). This is modeled in our initial conditions as initial streamwise-invariant vorticity disturbances. Linear theory is used to determine the disturbance wavelengths, and in many cases linear eigenfunctions are used for the functional form of the disturbances. Unfortunately, since the inlet conditions of experimental mixing layers are generally not documented, the only measure of our success in modeling experimental conditions is the qualitative agreement of the computed flow structures with those observed experimentally.

Other initial conditions were also used to explore the sensitivity of the resulting structures. Included in the sensitivity study are the amplitude, phase, wavenumber, and functional form of the disturbances. In addition, different types of three-dimensional disturbances, including oblique modes, were studied. A few of the simulations performed as part of the sensitivity study result in flow developments that are radically different from the rest.

All the simulations described here and in Part 2 have limited spanwise-domain extents (up to one streamwise instability wavelength here, and up to 2.4 wavelengths in Part 2). This is because the simulations were designed to study the standard structures and their variants, which have a relatively narrow spanwise extent. We do not examine long-spanwise-wavelength phenomena such as the dislocations studied by Browand and Troutt (1980), slow spanwise variations of the mean profile (Rogers et al. 1988), spanwise variation of the phase of the fundamental disturbance (Nygaard and Glezer 1990) or the possible "helical" pairing studied by Chandrsuda et al. (1978).[1]

In section 2 some background information on the simulations and numerical method is presented. Results from two-dimensional simulations of plane mixing layers are given in section 3, the evolution of a variety of three-dimensional mixing layers is described in detail in section 4, summary and discussion appear in section 5, and brief conclusions are given in section 6.

Much of this work was begun in collaboration with visiting scientists at the 1988 Center for Turbulence Research Summer School Program. In particular, we are grateful for discussions with Professors C.-M. Ho, F. Hussain, and J. Riley. In addition, we have benefited from comparisons with the spatially developing mixing-layer work of Dr. J. Buell and the compressible shear layer work of Prof. S. K. Lele, and from Prof. E. Broadwell's vast experience with experimental mixing layers. Helpful comments provided by Dr. N. Mansour on a draft of this paper are also appreciated. Some of the computations were performed on the NAS supercomputers at Ames Research Center.

---

[1] Note, however, that Part 2 does include simulations with disturbances of the type that Pierrehumbert and Widnall (1982) felt could lead to helical pairing.

2 PRELIMINARIES

2.1 The Temporally Evolving Plane Mixing Layer

In experimental wind tunnels and in many technological applications, the plane mixing layers of interest are spatially developing. Typically, two free streams of unequal velocity merge downstream of a splitter-plate that physically separates them. The vorticity at the interface between the two streams then rolls up as a result of the well-known Kelvin–Helmholtz instability. If one were to observe the resulting mixing layer in a reference frame moving at the average of the two free-stream velocities, the evolution of a single Kelvin–Helmholtz roller could be observed. In this frame of reference the flow appears to develop in time. For free-stream velocity ratios near 1, there is little difference in the eddies upstream and downstream of any particular point. This suggests the alternative temporally evolving form of a plane mixing layer, in which the flow is homogeneous in the streamwise direction and evolves in time from a prescribed initial condition rather than in space from upstream inlet conditions. It can be shown (Buell, Moser, and Rogers, to be published) that in the limit of equal free-stream velocities, the spatially and temporally developing mixing layers are identical. Although only an approximation to a spatially developing mixing layer, the temporally evolving layer is also of interest as a good model of geophysical mixing layers, which form in the absence of a splitter-plate (Turner 1973), and of the stratified tilting-tank experiments of Thorpe (1968, 1971, 1973, 1985).

The temporally evolving formulation has many advantages for direct numerical simulation, and for this reason it has been used often in the study of mixing layers. The greatest advantage is that the computational domain need only capture a few Kelvin–Helmholtz roll-ups rather than the entire flow evolution from the splitter-plate to the outflow boundary. This permits the use of finer meshes and, therefore, the simulation of higher Reynolds numbers (or more pairings at a given Reynolds number). Even with the best computers available today, the study of mixing transition (see Part 2) is simply not feasible in a spatially developing simulation. Another advantage of the temporal formulation for numerical simulation is that periodic boundary conditions may be used in the streamwise direction, eliminating the need for inflow and outflow boundary conditions. Current spatially developing flow simulations cannot entirely eliminate forcing of the inlet by unphysical signals reflected from the downstream outflow boundary (Buell and Huerre 1988).

The major goal of the work reported here is to study three-dimensionality in plane mixing layers, and in particular to understand the mechanisms leading to the "mixing transition." Therefore, well-resolved, high-Reynolds-number, three-dimensional simulations are required. This can only be accomplished for the temporally evolving problem and, therefore, that is the formulation studied here. To ensure that the flows simulated do indeed resemble their spatially evolving counterparts, many of the results of this work, and of the work reported in Part 2, have been compared with the spatially developing simulations of Buell and Mansour (1989a) (at a velocity ratio of 0.2). In all the comparisons it was found that the dynamic mechanisms that occur in the time-developing layer also occur in the spatially developing layer.[2] Two important ways in which the temporally and spatially developing mixing layers do differ are outlined below.

---

[2] A thorough comparison will be available in a report by Buell, Moser, and Rogers (to be published).

In an incompressible spatially developing layer, any structure can affect the evolution of all other eddies in the flow, both upstream and downstream. In the temporally developing flow, events in the present cannot change those that have already occurred. Thus, when considering the evolution in time as an approximation to the evolution in space of a spatially developing layer, the elliptic nature of the flow development is not represented. This might seem to be a severe limitation of the temporal approximation, but in practice the vortex dynamics of the developing mixing layer appear to be dominated by local interactions and not to be strongly affected by the streamwise inhomogeneity.

Another difference between temporally evolving and spatially evolving mixing layers is the entrainment of free-stream fluid. Because of the streamwise homogeneity in the temporally evolving case, as much free-stream fluid enters the domain from upstream as leaves downstream. The mean-flow continuity equation then requires that the mean vertical velocity be a constant; to fix the layer location, this constant is taken to be zero. Thus, in the temporal problem there is no inflow at infinity. In the spatially developing problem the amount of free-stream fluid leaving the domain need not equal the amount entering it, and a mean inflow from infinity (on both sides of the layer) is possible. Moreover, it is well known that a spatially developing mixing layer entrains more fluid from the high-speed side. These entrainment characteristics are not reproduced in a temporally developing mixing layer.

Finally, there is an important subtlety in comparing statistical properties of spatially developing and simulated time-developing mixing layers. In an experimental spatially developing mixing layer, average properties are obtained by time-averaging the signal from a fixed probe. If the inlet conditions are stochastic, a variety of different structures will pass the fixed probe and contribute to the average. The analogous situation in the time-developing mixing layer is to use stochastic initial conditions in a very large spatial domain and average in the streamwise direction. However, using a large spatial domain obviates one of the main advantages of a time-developing simulation. Instead, a small spatial domain is used, and the averages only include the contribution of a few structures. This is analogous to providing a time-periodic (nonstochastic or forced) inlet condition in a spatially developing mixing layer. The resulting statistics can be qualitatively different. For example, in a natural spatially developing mixing layer (stochastic inlet), the layer thickness grows linearly in the streamwise direction, whereas in our simulations and in forced spatially developing layers (e.g., Ho and Huang 1982) the thickness may even grow nonmonotonically (see secs. 3.2 and 4.2.1). Since our major concern in the current work is the characterization and evolution of the commonly observed structures in the mixing layer, the inclusion of just a few structures in average quantities is not a concern.

2.2 Governing Equations and Numerical Considerations

The simulations reported here were obtained by solving the vorticity equation derived from the incompressible Navier–Stokes equations:

$$\frac{\partial \boldsymbol{\omega}}{\partial t} + \nabla \times (\boldsymbol{\omega} \times \mathbf{U}) = \frac{1}{Re} \nabla^2 \boldsymbol{\omega} \qquad (1)$$

where $\mathbf{U}(x, y, z, t)$ is the velocity vector (with components u, v, and w), and $\boldsymbol{\omega} \equiv \nabla \times \mathbf{U}$ is the vorticity vector. Here, U (the half-velocity difference) and δ_ω^0 (the initial vorticity thickness of the layer, see eq. (4)) have been used to nondimensionalize the equations and form the Reynolds number $Re = U\delta_\omega^0/\nu$ (ν is the kinematic viscosity). Throughout the paper this nondimensionalization is used. In addition, the evolution of a passive scalar T is computed using the scalar equation

$$\frac{\partial T}{\partial t} + \mathbf{U} \cdot \nabla T = \frac{1}{Pe} \nabla^2 T \tag{2}$$

where the Peclet number is given by $Pe = ReSc$ and the Schmidt number by $Sc = \nu/\gamma$ (where γ is the molecular diffusivity of the scalar).

The above equations are solved using periodic boundary conditions with periods L_x and L_z in the streamwise (x) and spanwise (z) spatial directions.[3] In the cross-stream (y) direction, ω and $T - \overline{T}$ (where $\overline{T}$ is the average mean scalar profile in y) go to zero as $y \rightarrow \pm\infty$. The x- and z-dependence of the independent variables is represented by finite Fourier series, and the y-dependence is represented as a polynomial expansion in the mapped variable $\eta = \tanh(y/y_0)$, where y_0 is a mapping parameter (usually set to be of the order of the final layer thickness). In addition, the y-dependence of the velocity $\mathbf{U}$ is represented using special expansion functions that exactly represent the slow decay of velocity perturbations at $\pm\infty$. The computational method was developed specifically for the simulation of three-dimensional free shear layers. It is a spectral Galerkin method and exhibits "infinite-order" accuracy of the spatial discretization. A detailed description of the method can be found in Spalart, Moser, and Rogers (1991). The equations were advanced in time using a compact third-order Runge-Kutta scheme of the form proposed by Wray (personal communication; see Spalart, Moser, and Rogers (1991) for details). The Galerkin quadratures involving the nonlinear terms are computed using a Gauss quadrature with sufficient points to eliminate aliasing.

2.3 Specification of Initial Conditions

The self-similar solution for the streamwise velocity profile of the laminar, temporal, plane mixing layer is a viscously spreading error function. Thus, an error function,

$$\overline{U} = U \mathrm{erf}(\sqrt{\pi} y / \delta_\omega^0) \tag{3}$$

is used for the initial mean streamwise velocity profile in most of the simulations discussed here. Note that this profile has a vorticity thickness

$$\delta_\omega \equiv \frac{2U}{(\partial \overline{U}/\partial y)|_{\mathrm{max}}} \tag{4}$$

of δ_ω^0. Other initial mean streamwise velocity profiles were also used for a few simulations. Hyperbolic tangent profiles result in flows that are similar to those resulting from the error function profile (eq. (3)). Initial mean profiles containing a splitter-plate wake component (discussed in sec. 4.3.7) were also used. Such profiles break the symmetry of the error function profile and can lead to more complex flows. In all cases the initial mean passive scalar profile is given by

$$\overline{T} = \frac{1}{2}[1 + \mathrm{erf}(\sqrt{\pi} y)] \tag{5}$$

---

[3] Note that spanwise periodicity precludes the possibility of studying end-wall effects, that is, side-wall boundary layers, etc.

where the magnitude of the scalar is arbitrary since the passive scalar governing equation is linear in the scalar quantity T (see eq. (2)).

In addition to the mean velocity, simple perturbations are included in the initial conditions. These perturbations include just one or a few of the x- and z-Fourier modes of the solution. Streamwise and spanwise fundamental wavelengths (λ_x and λ_z) are chosen (usually the most unstable wavelengths from linear theory; see secs. 3.1, 4.1) and perturbations with these wavelengths are used. To accommodate these perturbations, the computational domain must be an integer multiple of these wavelengths in the x- and z-directions. Thus, in general, $L_x = N\lambda_x$ and $L_z = M\lambda_z$, and N and M are 1 for all cases reported here (they are as large as 8 for cases in Part 2).

To specify the initial conditions and to facilitate discussion throughout this paper it is necessary to refer to specific wavenumbers; they will be referred to in ordered pairs

$$(\alpha,\beta) = \left(k_x\lambda_x/(2\pi), k_z\lambda_z/(2\pi)\right) \tag{6}$$

Thus, the perturbations discussed above have energy in modes with α or β or both equal to 1. In general, the simulations include wavenumbers with $\alpha = \pm j/N$ for $j = 0, 1, 2, \ldots, (N_x - 2)/2$ and $\beta = \pm l/M$ for $l = 0, 1, 2, \ldots, (N_z - 2)/2$, where N_x and N_z are the (even) number of Fourier modes in the x- and z-directions, respectively. Note that because the quantities under consideration are real, the (α, β) mode of their Fourier transform is the complex conjugate (denoted by *) of the $(-\alpha, -\beta)$ mode. Thus, in most cases we may consider only modes with $\alpha \geq 0$.

In addition to its wavenumber, an initial perturbation requires specification of its functional form, an amplitude, and a phase to be completely determined. In the simulations reported here perturbations with four different functional forms were used. The simplest form used here is a Gaussian in y ($e^{-\pi y^2}$) for either a vorticity component or the vertical velocity; these are referred to as ω-Gaussian (ωG) and v-Gaussian (vG), respectively. The most unstable eigenfunctions of the linear disturbance equation for the Fourier mode under consideration were also used. Both viscous eigenfunctions (VE, from the Orr–Sommerfeld equation) and inviscid eigenfunctions (IE, from the Rayleigh equations) were used.

The amplitude of a given Fourier mode (of an initial perturbation or in the evolved field) can be measured by the integrated (in y) rms velocity of the mode. Thus, we define

$$A^{\pm}_{\alpha\beta} = \sqrt{\int_{-\infty}^{+\infty} 2\hat{u}_i(\alpha, \pm\beta)\hat{u}_i^*(\alpha, \pm\beta)\, dy} \quad \alpha \geq 0 \text{ and } \beta \geq 0 \tag{7}$$

where $\hat{u}_i(\alpha, \beta)$ is the (α, β) Fourier mode of the velocity component u_i. Note that $A^{\pm}_{\alpha\beta}$ has only been defined for non-negative α and β. Negative α is not necessary, because of the conjugate symmetry of the Fourier transform, and negative β is represented by $A^{-}_{\alpha\beta}$. Note also that the factor of 2 in the integrand is to account for the energy in the conjugate symmetric mode $(-\alpha, \mp\beta)$, and that $A^{+}_{\alpha\beta} = A^{-}_{\alpha\beta}$ when α or β is zero. It will also be convenient to define a combined amplitude $A_{\alpha\beta}$, which includes both the positive and negative β modes, thus:

$$A_{\alpha\beta} = \begin{cases} A^{+}_{\alpha\beta} & \text{if } \alpha = 0 \text{ or } \beta = 0 \\ \sqrt{(A^{+}_{\alpha\beta})^2 + (A^{-}_{\alpha\beta})^2} & \text{otherwise} \end{cases} \tag{8}$$

Throughout this report, $A_{\alpha\beta}$ is quoted normalized by $U\sqrt{\delta_\omega^0}$. Also, the superscript *sat* is used to indicate the saturation amplitude of a given Fourier mode (the level of the first maximum of $A_{\alpha\beta}$ in time).

Finally, the absolute phase of a given perturbation Fourier mode is not generally relevant, because of homogeneity in x and z. Phases have usually been chosen to conveniently position the resulting flow structures in the computational domain (e.g., place the Kelvin–Helmholtz roller in the center of the domain). However, the *relative* phase between different Fourier modes in the perturbation can be important. When this is the case the relative phases for the case under consideration will be described (sec. 4.4).

3 TWO-DIMENSIONAL ROLL-UP

To determine how a three-dimensional mixing layer departs from its two-dimensional counterpart, it is necessary to consider two-dimensional flows as a basis for comparison. In addition to determining the amount of "three-dimensionality" present in the three-dimensional flows, such simulations enable one also to study important phenomena that are essentially two-dimensional. The Kelvin–Helmholtz roll-up of spanwise vorticity into rollers, the pairing of these rollers, and the rate of spanwise vorticity depletion in the braid region between these rollers (as well as its reentry into the braid region at late times) are examples of two-dimensional phenomena that are relevant to three-dimensional flows. Two-dimensional simulations also provide a quick way to determine the effect of varying the two-dimensional parameters (at least while the three-dimensional disturbances are relatively weak). Changes brought about by varying such parameters (i.e., wavelength, form, and amplitude of a two-dimensional disturbance) and by varying the Reynolds number are described below. A list of the two-dimensional simulations for which data are presented is given in table 1. Many other two-dimensional simulations were also performed to corroborate conclusions drawn in the text. In all these simulations the only initial disturbance was in the $(1,0)$ mode.

Table 1. Parameters of the two-dimensional simulations[a]

Simulation	Re_0	τ_r	τ_o	Disturbance	A_{10}
2D100	100	10.5	14.4	VE	0.10
2D250	250	10.3	14.5	VE	0.10
2D500	500	10.1	14.6	VE	0.10
2D500vG	500	11.3	17.8	vG	0.10
2D500ωG	500	11.2	18.2	ωG	0.10
2D1000	1000	10.0	14.8	VE	0.10
2D2000	2000	10.0	14.9	VE	0.10

[a] $Pr = 1.0$ and $\lambda_x = 1.16(2\pi)$ for all cases.

3.1 Variation and Selection of Initial Conditions

For the vast majority of the simulations described in this paper and in Part 2, the initial instability wavelength λ_x was taken to be the most unstable wavelength in the absence of viscosity of the initial error function profile given by equation (3). Linear stability calculations for this case show the most unstable wavenumber to be $k_x = 2\pi/\lambda_x = 0.86$ (Monkewitz and Huerre 1982, verified by the computational method used here). Neither the linear growth rate nor the structure of the resulting flow is sensitive to variations in the wavenumber near the most unstable wavenumber. Likewise, changes in the growth rate resulting from the presence of viscosity are small at moderate Re_0: a 5% reduction from the inviscid value for $Re_0 = 250$. Large departures from the most unstable wavelength can result in different distributions of spanwise vorticity, different saturation energy levels of the fundamental disturbance, and different amounts of time required to reach this saturation.

For the initial disturbance levels considered here, all functional forms (see sec. 2.3) of the fundamental two-dimensional perturbation ((1, 0) mode) lead to qualitatively the same behavior.[4] This is not surprising, because initial disturbances that are small enough for linear theory to apply will all evolve to the viscous eigensolution regardless of the initial form. However, some quantitative differences between the different functional forms can be detected. In particular, disturbances of different forms with the same amplitude (A_{10}) will have different initial enstrophy ($\omega_i \omega_i$) levels. Also, the flow resulting from an initial Gaussian disturbance will develop less rapidly than a flow resulting from a VE disturbance with the same amplitude (see fig. 1(a)). The reason for this is simply that the Gaussian disturbances have a smaller projection on the unstable eigenfunction. The effect is similar to reducing the initial amplitude of the VE disturbance and can be approximated by a shift in the time axis as expected from linear theory. Another effect of varying the disturbance functional form is that the initial peak magnitude of the vorticity varies. In a two-dimensional flow, there is no vortex stretching and the vorticity extrema are bounded by their initial values; in the absence of viscosity, the extrema are constant. Because of the relatively high Reynolds number ($Re_0 = 500$) of the cases under consideration, there is little decay of the peak vorticity level for the duration of the simulations. The disparity in vorticity extrema among the cases with different disturbance forms is thus "locked in" (see fig. 1(b)).

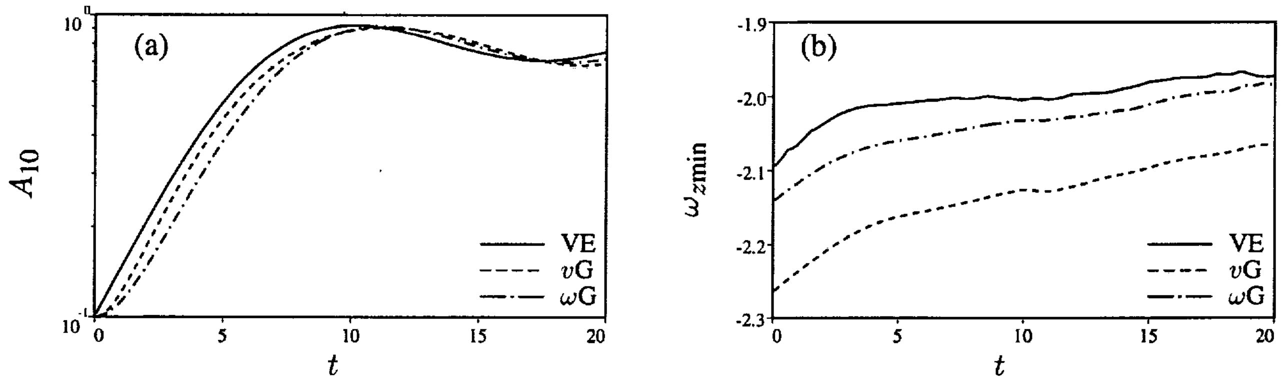

Figure 1. Time development of (a) A_{10} and (b) spanwise vorticity extrema at $Re_0 = 500$ for various initial two-dimensional disturbance profiles.

---

[4] For the Reynolds numbers used here the IE initialization leads to results that are nearly identical to those obtained from VE initialization, with only slight differences during a short adjustment period. The vG and ωG initializations result in slightly more significant quantitative differences.

Finally, the amplitude of the initial disturbance must be specified. If the disturbances present in experiments were truly infinitesimal, they would grow according to linear theory until nonlinearity became significant. By using viscous eigensolutions with an initial amplitude just slightly less than that at the onset of nonlinearity, we can avoid simulating the linear regime. In practice, some linear development is simulated to allow any necessary adjustments (i.e., the adjustment of nonviscous eigenfunction vertical profiles and, in three-dimensional simulations, the development of vorticity components that were not initialized). Also, because the mixing layer is thickening by viscous diffusion, it is important that the initial disturbance amplitude not be too small. An excessively weak initial disturbance will permit the layer to grow by diffusion to the point at which λ_x is no longer a good approximation to the most unstable wavelength. It was found that an initial amplitude A_{10} of 0.1 met the requirements outlined above, and this amplitude was used for most of the simulations reported here. Cases with disturbance levels as low as 0.01 have also been simulated, with the box size L_x increased to accommodate the longer instability wavelengths associated with the viscously thickened layer. Comparisons of various quantities of interest between runs of different initial disturbance amplitudes show that the dominant effect of this variation is simply a shift in time without a significant change in the character of the time development. In conclusion, it should be noted that the effort to match the growth of infinitesimal disturbances is somewhat arbitrary since experimental disturbances are not infinitesimal.

3.2 Time Development and Reynolds Number Variation

Based on the discussion in section 3.1, an initial perturbation consisting of a viscous eigenfunction in the (1,0) mode with amplitude $A_{10} = 0.1$ was selected as the baseline two-dimensional disturbance. In this section, several simulations with a range of Reynolds numbers from 100 to 2000 will be examined, to describe the two-dimensional evolution of the flow and to determine the effects of Reynolds number variation.

As the flow evolves from the initial VE disturbance in the (1,0) mode, the amplitude A_{10} of that Fourier mode grows exponentially for a time at a rate consistent with linear theory (fig. 2). The Fourier amplitude ultimately saturates, reaching a maximum at the "roll-up time" τ_r (reported in table 1). This definition is arbitrary, but other definitions (such as the time to reach the peak enstrophy level of the (1,0) mode) yield similar values. It is apparent in figure 2 that the lower Reynolds number simulations (100 and 250) have a lower saturation amplitude (A_{10}^{sat}) and a larger τ_r. However, for $Re_0 \geq 500$, the amplitude evolutions are nearly identical.

As the disturbance is growing, the spanwise vorticity is collecting into a spanwise roller at the expense of the vorticity in the braid regions located between a roller and its periodic images (fig. 3). By τ_r (fig. 3(b)), the roller is roughly circular, and the vorticity is largely depleted from the braid region. Since there is no subharmonic mode $(\frac{1}{2},0)$, the rollers cannot pair, but become elliptical in shape (fig. 3(c)). As they become more elliptical, they extend further into the braid region so that spanwise vorticity reenters this region. Similar development is observed in experimental mixing layers when the inlet conditions are forced periodically at a single (fundamental) frequency (see, for example, fig. 2 of Ho and Huang 1982 and Nygaard and Glezer 1991). In this "oversaturated" state, some vorticity will eventually cross the plane halfway between the roller and its periodic image (the edge of the domain in this case), later to be absorbed by the periodic image roller.

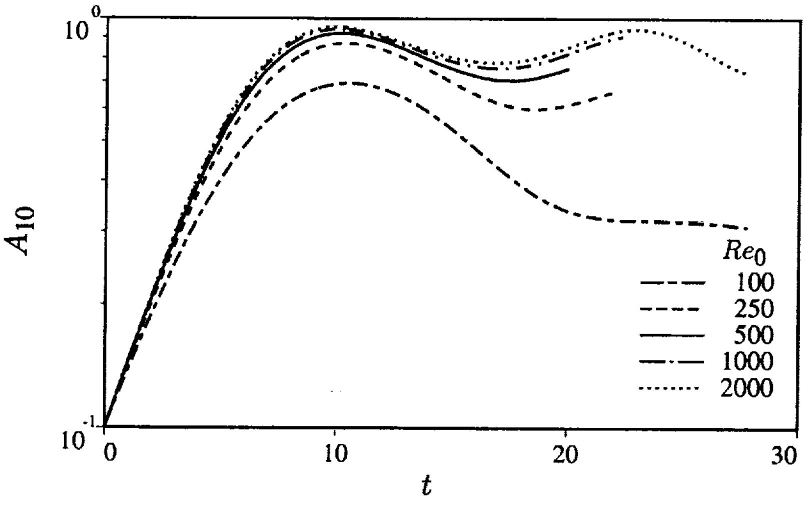

Figure 2. Time development of A_{10} at various Reynolds numbers (viscous eigenfunction disturbance profiles were used).

The depletion of vorticity from, and the ultimate reentry of vorticity into, the braid region can be tracked in time by monitoring ω_b, the strongest vorticity in the mid-plane between the rollers (fig. 4(a)). The magnitude of ω_b declines steadily as vorticity is depleted from the braid region, but suddenly increases at time τ_o (oversaturation time, also reported in table 1), corresponding to the reentry of vorticity into the braid region as discussed above. This oversaturation has important consequences in three-dimensional mixing-layer evolution. Shortly after τ_o, the magnitude of ω_b again decreases. For large enough Re_0, the oversaturated eddy may again eject vorticity into the braid region. This second reentry of spanwise vorticity into the mid-braid region occurs in the $Re_0 = 2000$ case at $t = \tau_{oo} = 25.6$ (fig. 4(a)).

As can be seen in figure 4(a), increasing the Reynolds number delays the removal of vorticity from the mid-braid region (presumably because viscous thickening reduces the vorticity levels in the braid region, an effect present even in the absence of roll-up). Despite this, τ_o is nearly the same for all the cases shown. The minimum magnitude of ω_b reached at τ_o does not exhibit a monotonic trend with Re_0. For $Re_0 = 100$, the relatively large viscosity limits the ability of the rollers to deplete vorticity from the braid region, and for large Re_0 the delayed depletion results in a larger ω_b at τ_o. The lowest magnitude of ω_b is achieved for a Reynolds number between 250 and 500. The magnitude of the spanwise vorticity brought back into the braid region for $t > \tau_o$ is greater for larger Re_0. At $Re_0 = 100$, ω_b exhibits behavior qualitatively different from that at the higher Reynolds numbers. The decay of ω_b is rapid, a result of viscous thickening, and there is no second period of braid vorticity depletion after τ_o.

As the vorticity is extracted from the braid region, this region becomes dominated by plane strain. The evolution of the braid strain-rate is also important in three-dimensional flows. The evolution of the maximum principal strain-rate in the mid-plane between the rollers is shown in figure 4(b). At early times the maximum strain-rate is nearly 1, because it is dominated by the mean velocity gradient. As the mixing layer rolls up, the strain-rate decreases to a plateau level of about 0.5 by τ_o. This is more than the large-scale strain-rate estimate $\Delta U/\lambda_x$, which is 0.27 in these flows. This plateau value of

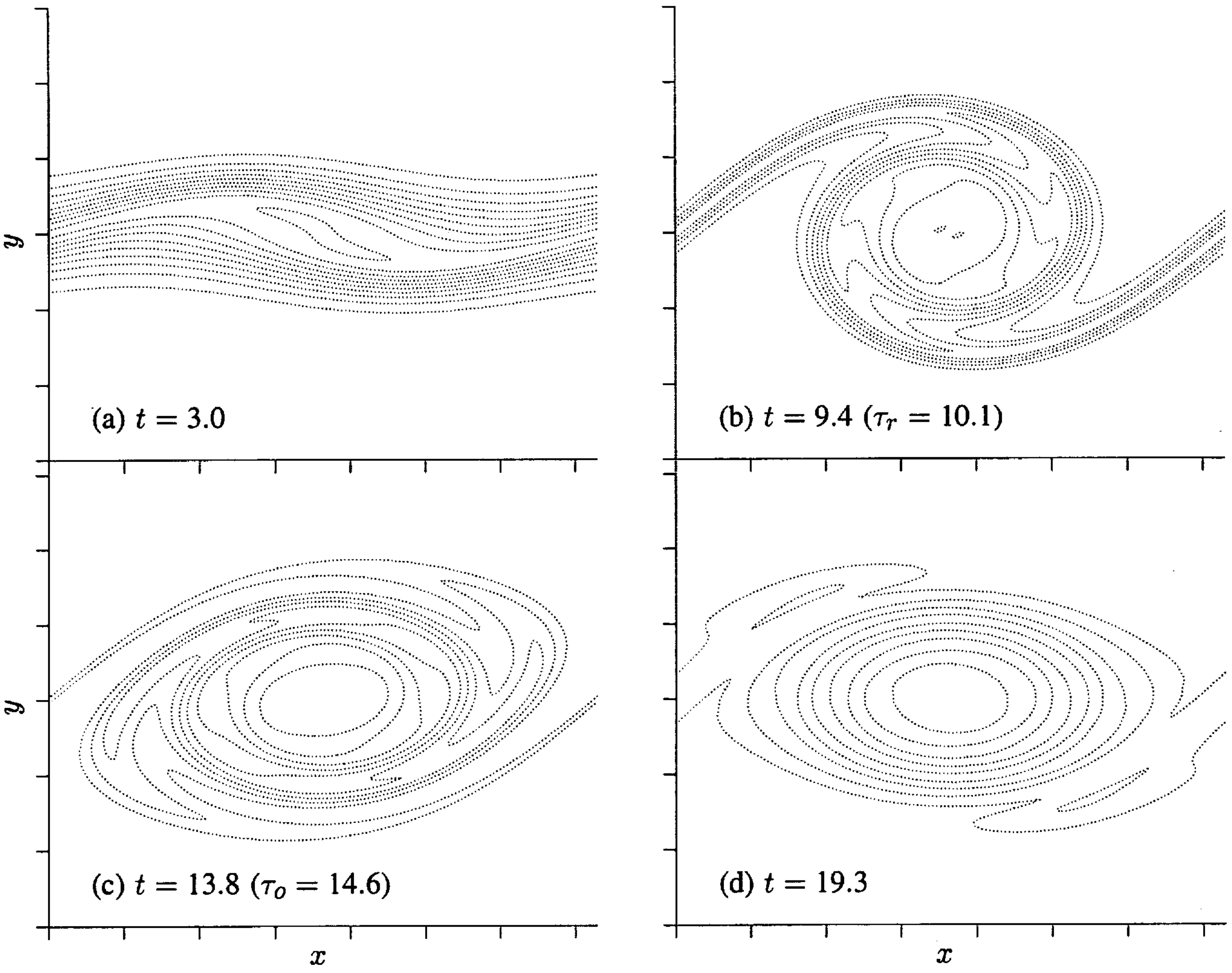

Figure 3. Contour plots of spanwise vorticity. Contour increment is -0.2, and tic marks are at δ_ω^0 intervals.

the maximum strain-rate is nearly constant over our Reynolds number range. However, the initial rate at which the strain-rate is reduced does depend on Re_0, with lower Reynolds numbers producing more rapid reductions. In fact, for $Re_0 \geq 500$, the maximum mid-braid strain-rate *increases* initially.

Two other quantities of interest are also shown in figure 4. The time development of the momentum thickness,

$$\delta_m = \int_{-\infty}^{\infty} (1 - U^2) dy \tag{9}$$

is shown in figure 4(c). For $Re_0 \geq 500$, the curves are nearly identical, and the $Re_0 = 250$ curve is similar. The $Re_0 = 100$ case, on the other hand, shows significant viscous effects, including substantial early-time viscous thickening, and damping of the late-time oscillations. Viscous effects are also evident in the peak vorticity levels shown in figure 4(d) for $Re_0 \leq 250$. For $Re_0 \geq 500$, the viscous decay of the peak level is minimal.

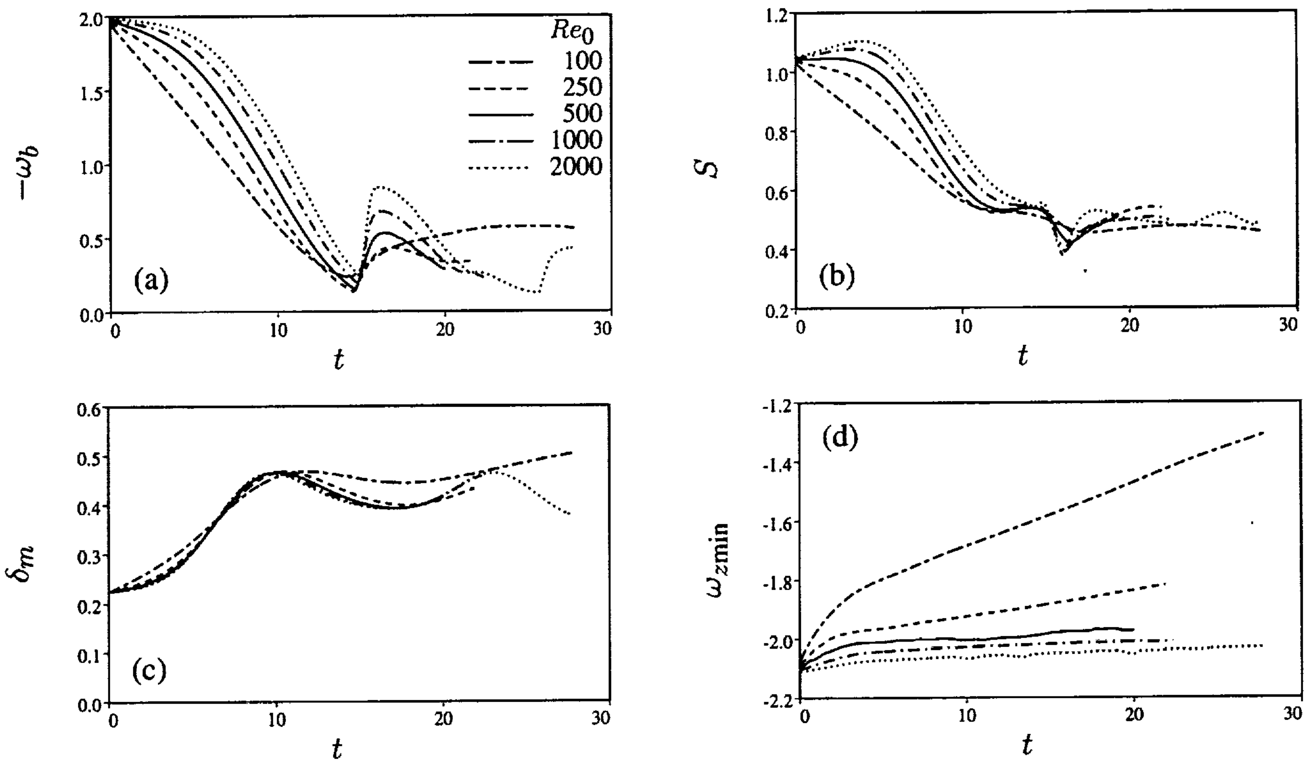

Figure 4. Time development of (a) mid-braid vorticity, (b) mid-braid strain-rate, (c) momentum thickness, and (d) vorticity extrema at various Reynolds numbers (viscous eigenfunction disturbance profiles were used).

To demonstrate the effects of Reynolds number variation on flow structure, the vorticity and passive scalar contours just before τ_o are shown in figure 5 for Reynolds numbers of 100, 500, and 2000. The differences are striking. The $Re_0 = 100$ flow is smooth and well mixed (as can be seen from the passive scalar contours). The $Re_0 = 2000$ case shows many "windings" of vorticity, separated by free-stream fluid. The $Re_0 = 500$ case is similar to the $Re_0 = 2000$ flow in that the windings of vorticity and scalar are evident, though they are not as pronounced.

All the results discussed above indicate that for initial Reynolds numbers less than 500, significant viscous effects become evident in these two-dimensional simulations. In order to avoid these low-Reynolds-number effects, 500 was selected as the Reynolds number for most of the simulations reported here.

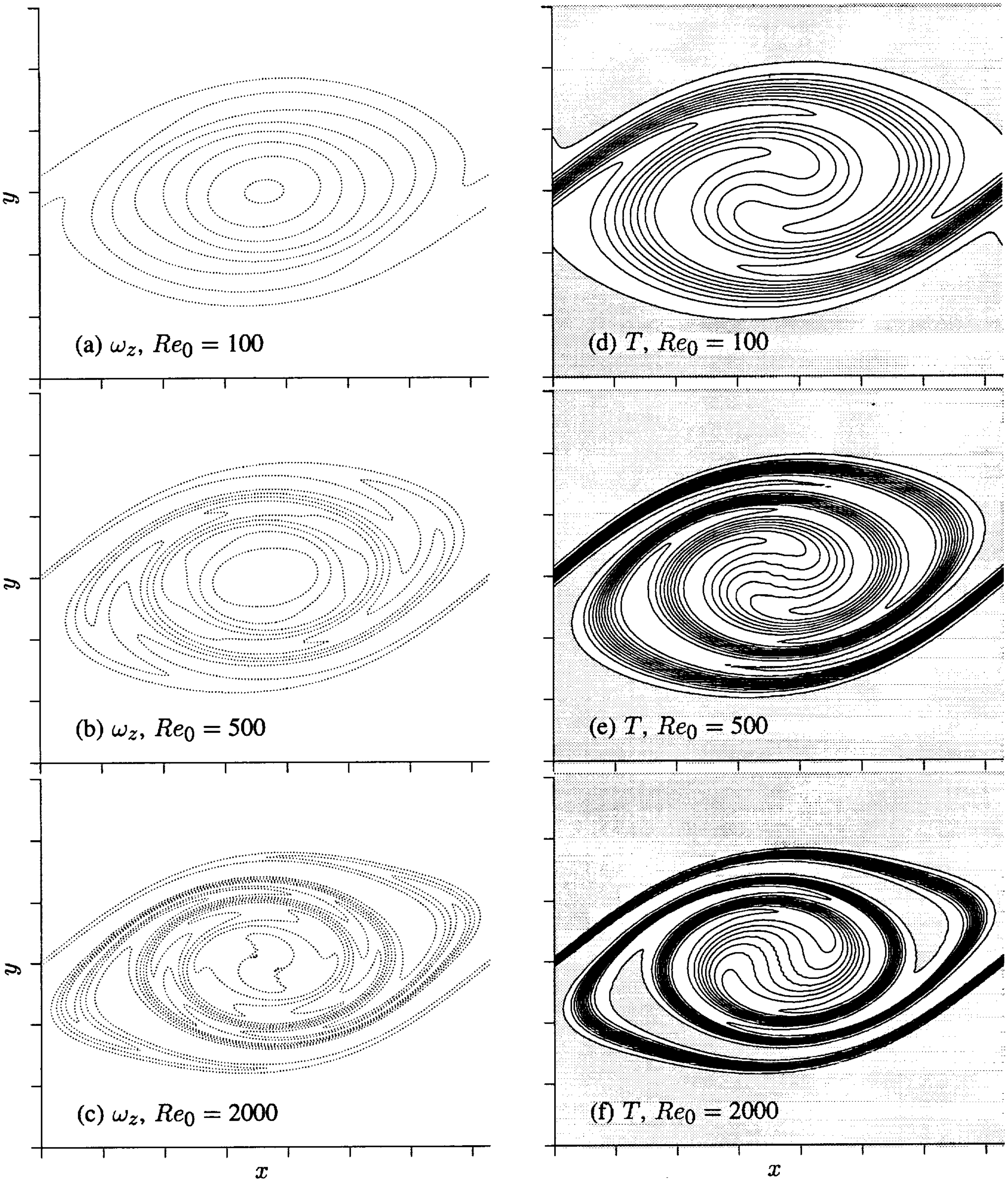

Figure 5. Contour plots of spanwise vorticity and the passive scalar (T) just before τ_o. Contour increments are (a)–(c) 0.02, and (d)–(f) 0.08. In (d)–(f), contours start at 0.02 (bottom) and go to 0.98 (top). Shaded regions indicate free-stream fluid, and tic marks are at δ_ω^0 intervals.

4 THREE-DIMENSIONAL ROLL-UP

4.1 Initial Conditions

In addition to the two-dimensional initialization parameters described in section 3.1, a number of three-dimensional parameters must be specified. These include spanwise disturbance wavelength, form, and strength of the three-dimensional disturbance, and phasing of the three-dimensional disturbance relative to the prescribed two-dimensional disturbance (see sec. 2.3). Also, although it is not feasible to increase the Reynolds number beyond $Re_0 = 500$, changes brought about by decreasing the Reynolds number will be examined.

First, a spanwise fundamental wavelength (λ_z) must be selected; it will determine the spanwise computational domain size ($L_z = \lambda_z$ for the simulations described here; see sec. 2.3). Pierrehumbert and Widnall (1982) found that three-dimensional disturbances with $\lambda_z/\lambda_x \approx 0.6$ are the most unstable for a row of Stuart (1967) vortices (core-size parameter $\rho = 0.25$, chosen to match the experimental vorticity distributions of Browand and Weidman (1976)). However, the growth-rate curve has a broad peak, signifying that the three-dimensional disturbance growth rate is not sensitive to the choice of λ_z. Corcos and Lin (1984) studied the linear stability of an evolving two-dimensional base flow and also found the growth rate to be insensitive to λ_z. We made a similar study (discussed in detail in sec. 5.3 and in Part 2) and, like Pierrehumbert and Widnall, find the most unstable spanwise wavelength to be $\lambda_z/\lambda_x \approx 0.6$. Because of this, most of the three-dimensional roll-up simulations were performed with $\lambda_z = 0.6\lambda_x = 0.696(2\pi)$. In agreement with the weak dependence on λ_z/λ_x noted above, simulations with $0.5 \leq \lambda_z/\lambda_x \leq 1.0$ yield results similar to those for the $\lambda_z/\lambda_x = 0.6$ case (e.g., sec. 4.3.3). Experiments (e.g., Huang and Ho 1990) also indicate that the most unstable spanwise wavelength is about $0.6\lambda_x$.

The functional form of the three-dimensional disturbance is described by the wavenumbers of the Fourier mode initialized (α, β) (see eq. (6) for definition), the vertical (y) profile of the disturbance, and the components of vorticity being initialized. Initial disturbance energy can be included as a streamwise invariant (STI) disturbance in the $(0, 1)$ mode, as an oblique disturbance in the $(1, \pm 1)$ modes, or as a combination of the two. For the oblique disturbances, both the $(1, 1)$ and $(1, -1)$ modes are generally initialized with the same vertical profile and the same amplitude, though simulations were also run with only one of these modes initialized (sec. 4.4.4). Note that because $\lambda_z/\lambda_x = 0.6$, the $(1, \pm 1)$ modes are at an angle of about 30° to the streamwise direction.

Several different initial vertical disturbance profiles were studied. Viscous eigenfunction (VE) profiles were usually used for the oblique disturbances. However, for the STI modes there are no eigenfunctions for our boundary conditions. For these cases (and some oblique disturbance cases), Gaussian vertical velocity (vG) or Gaussian streamwise vorticity (ωG) profiles were used. For most of the simulations the vertical vorticity component ω_y was not initialized. This typically resulted in a short (up to $t \approx 1$) development time during which ω_y grew rapidly to a level comparable to that of ω_x. If we were attempting to truly match the development of an infinitesimal disturbance, the initial ω_y would have to be nonzero to account for its development in the presence of an exponentially growing ω_x. Because of this, some simulations were run with ω_y initially nonzero (Gaussian vertical profile or equilibrium profile associated with the initial ω_x VE disturbance); they are discussed in section 4.3.6.

The initial energy in the three-dimensional disturbance is typically of the same order as that of the two-dimensional fundamental disturbance ($0.025 \le \sqrt{A_{01}^2 + A_{11}^2}/A_{10} \le 10$). The associated streamwise circulation, Γ_x (definition given in sec. 4.2.3), is thus much less than the spanwise circulation given by the mean flow boundary conditions, $\Gamma_z = \Delta U \lambda_x$. For the cases reported here, $0.005 \le \Gamma_x/\Gamma_z \le 0.100$.

Finally, the phasing of the three-dimensional disturbance relative to the two-dimensional disturbance must be specified. For the STI and single oblique disturbances, phase is not relevant since it only affects the positioning of the disturbances in the periodic computational domain. A pair of oblique waves, however, results in local vorticity concentrations that may appear where the two-dimensional roller will develop, where the braid region will develop, or anywhere in between, depending on the phase.

The two extreme phasings considered in this paper are the "in-phase" case, in which the three-dimensional streamwise vorticity concentrations are maximum at the mid-braid and the mid-roller streamwise locations, and the "out-of-phase" case, in which the streamwise vorticity is zero at these locations (see sec. 4.4). Pierrehumbert and Widnall (1982) termed the instability that arises from the in-phase case the "translative instability." They find no appreciable instability for the out-of-phase case, in which the three-dimensional disturbance causes a "bulging" of the vortex cores (rather than parallel bending as in the translative case).

The simple low-wavenumber initial conditions used in the flows examined here typically have two symmetries that are preserved by the Navier–Stokes equations and therefore are present throughout the flow evolution.[5] These two symmetries consist of a z-plane reflection symmetry,

$$\begin{aligned} \omega_i(x,y,z) &= -\omega_i(x,y,-z)\ , \quad i = x,y \\ \omega_i(x,y,z) &= \omega_i(x,y,-z)\ , \quad i = z \end{aligned} \tag{10}$$

where $z = 0$ is located at the zeros of the initial streamwise vorticity disturbance (here at the center or boundary of the computational domain), and a point-reflection symmetry,

$$\omega_i(x,y,z) = \omega_i(-x,-y,-z)\ , \quad i = x,y,z \tag{11}$$

where $x = 0$ is located at the center of, or between, the roller cores of the two-dimensional disturbance; $y = 0$ is the domain centerline; and $z = 0$ is at the peaks of the initial streamwise vorticity disturbance (or for the OBLOUT simulation described in section 4.4.2 at the zeros of the streamwise vorticity). The first of these symmetries implies that streamwise rib vortices, if they occur, will be found in pairs of positive and negative vorticity of equal strength. It can be broken by considering spanwise subharmonics (i.e., two pairs of ribs with ribs of different strengths), unequal strength ribs in a single pair (implying a mean spanwise flow), or other asymmetric flows such as single oblique wave disturbances. The second symmetry affects the streamwise rib shape, as described in sections 4.2 and 4.4.2.

The presence of these symmetries in many of the flows considered here simplifies the analysis of the simulation results. For example, the first symmetry, equation (10), allows an unambiguous definition of the rib streamwise circulation, and the second symmetry, equation (11), aids in defining and locating

---

[5] Because of numerical roundoff error, the initial integrated asymmetric enstrophy is of the order of 10^{-28} of the integrated enstrophy in the domain. This increases in time but remains below 10^{-22} in the simulations described here.

the rib vortex lines (see sec. 4.2.3). Of course, laboratory mixing layers do not possess these symmetries; therefore, cases that exclude one or both of the symmetries have been run to ensure that the insights gained from these idealized symmetric cases are valid in general (see secs. 4.3.7, 4.4.3, and Part 2).

4.2 Typical Roll-up Evolution

Parameters for the three-dimensional simulations discussed in sections 4.2 through 4.4 are given in table 2. In this section, the evolution of the ROLLUP simulation is described in detail. The ROLLUP simulation was begun from a VE, $A_{10} = 0.10$ two-dimensional fundamental disturbance and an STI ωG disturbance of amplitude such that initially $\Gamma_z/\Gamma_x^0 = 40$, using disturbance wavelengths $\lambda_x = 1.16(2\pi)$ and $\lambda_z = 0.696(2\pi)$ with $Re_0 = 500$.[6] Although the flow development is sensitive to initial conditions, a number of low-wavenumber disturbances lead to structures that resemble those described here for ROLLUP. Effects of varying the various initial parameters will be discussed in following sections using the results presented below as a baseline for comparison.

The initial condition ($t = 0$) used for the simulation is shown in figure 6. The spanwise vorticity is present in a two-dimensional sheet with a slight concentration caused by the two-dimensional fundamental disturbance. The streamwise vorticity exists in two tube-shaped regions (one positive, one negative) that have no streamwise variation, as described in section 4.1. Despite the fact that a surface contour plot suggests that these tubes are streamwise vortices, vortex lines show that the shaded

Table 2. Parameters of the three-dimensional simulations[a]

Simulation	τ_r	τ_o	τ_c	3D dist	(k_x, k_z)	Γ_x^0/Γ_z
ROLLUP	9.8	13.5	8.8	ωG	(0,1)	0.025
LOROLL	10.1	14.1	$\gg \tau_o$	ωG	(0,1)	0.005
HIROLL	7.5	12.1[b]	4.9	ωG	(0,1)	0.100
LOWRE	10.1	12.9	$\gg \tau_o$	ωG	(0,1)	0.025
WIDEROLL	9.9	13.8	$\gg \tau_o$	ωG	(0,1)	0.025
DELAY	12.1	16.1	9.8	ωG	(0,1)	0.025
LOWDEL	12.4	15.9	10.7	ωG	(0,1)	0.025
VGROLL	9.6	13.5	7.6	vG	(0,1)	0.025
WYROLL	10.1	13.8	13.4	ωG	(0,1)	0.000[c]
OBLIN	10.2	13.4	7.3	VE	(1,1)	0.025 in phase
OBLOUT	9.9	13.7	N/A	VE	(1,1)	0.025 out phase
OBLMID	10.0	13.0	8.2	VE	(1,1)	0.025 mid phase

[a] $Pr = 1.0$ and $\lambda_x = 1.16(2\pi)$ for all cases; $\lambda_z = 0.6\lambda_x$ for all cases except WIDEROLL ($\lambda_z = \lambda_x$); $Re_0 = 500$ for all cases except LOWRE ($Re_0 = 100$) and LOWDEL ($Re_0 = 250$); and the initial two-dimensional fundamental disturbance for all cases was VE $A_{10} = 0.10$ except for DELAY and LOWDEL, which were begun from VE $A_{10} = 0.04$.

[b] Actual reentry of spanwise vorticity at $t \approx 14.5$ (see text).

[c] Initial disturbance in ω_y (not ω_x as other simulations), thus $\Gamma_x^0 = 0$; peak level of ω_y same as that of ω_x in ROLLUP.

---

[6] Γ_x^{MP} is used to denote the value of Γ_x at the mid-braid streamwise location, and $\Gamma_x^0 = \Gamma_x^{\mathrm{MP}}(t = 0)$. Note when using an STI disturbance for the initial condition, Γ_x is not a function of x.

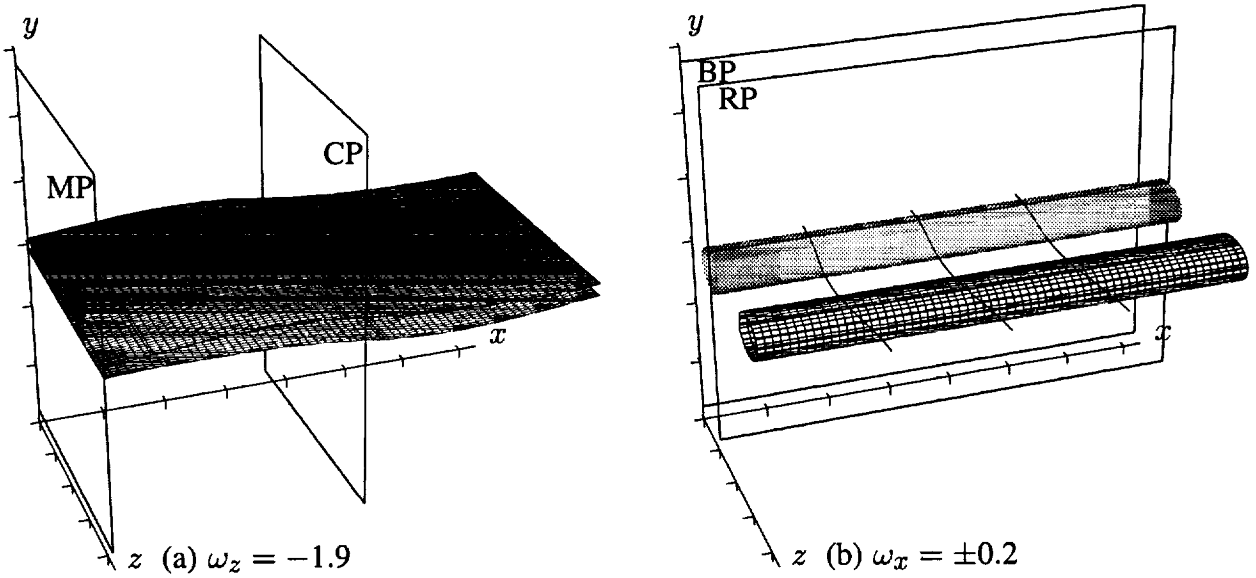

(a) $\omega_z = -1.9$ (b) $\omega_x = \pm 0.2$

Figure 6. Surfaces of constant vorticity magnitude and vortex lines at $t = 0$. Cross-hatched surfaces represent negative vorticity levels, shaded surfaces represent positive vorticity levels, and tic marks are at δ_ω^0 intervals. Also shown are the special planes MP, CP, BP, and RP.

and cross-hatched regions in figure 6(b) are not vortices but simply regions where the vorticity has a streamwise component; that is, the nearly spanwise vortex lines are kinked in this region. It should be noted that the presence of this three-dimensional disturbance does not alter the two-dimensionality of the spanwise vorticity because $\partial\omega_x/\partial x = 0$.

To study the details of the evolving three-dimensional flow, it will be necessary to examine contour plots in planes cut through it. The four planes used here are superimposed on the initial vorticity contours in figure 6. They intersect at least part of virtually all the flow structures that develop and are, therefore, sufficient to describe the flow development. As mentioned above, the two-dimensional disturbance causes a slight concentration in the spanwise vorticity sheet. The roller core will eventually form at this location. The z-y plane cutting through the location of the maximum $-\omega_z$ perturbation of the two-dimensional disturbance is called the "roller core plane" and is referred to here as CP. The z-y planes halfway between the CP and its periodic images are termed the mid-braid planes (MP) and are located in the middle of what will become the braid region as the flow evolves. In addition to these two z-y planes, two x-y planes are shown in figure 6(b). The rib planes (RP) are located at the z-locations of the extrema of the ω_x disturbance (the one associated with the positive ω_x disturbance is shown). The roughly streamwise "rib vortices" (sec. 4.2.2) will be located in this plane as the flow evolves. The between-ribs planes (BP) are located halfway between neighboring RPs (which contain opposite signs of ω_x). For the flow in figure 6, symmetry considerations ensure that $\omega_x = \omega_y = 0$ in the BPs. Flow symmetry also implies that the flow features in the RP and BP not shown in figure 6(b) are reflections of those in the planes shown.

4.2.1 Comparison with two-dimensional evolution– Here the time evolution of several quantities in the three-dimensional ROLLUP simulation is compared with the corresponding development in a two-dimensional flow that has the same initial Reynolds number and the same initial two-dimensional disturbance (2D500).

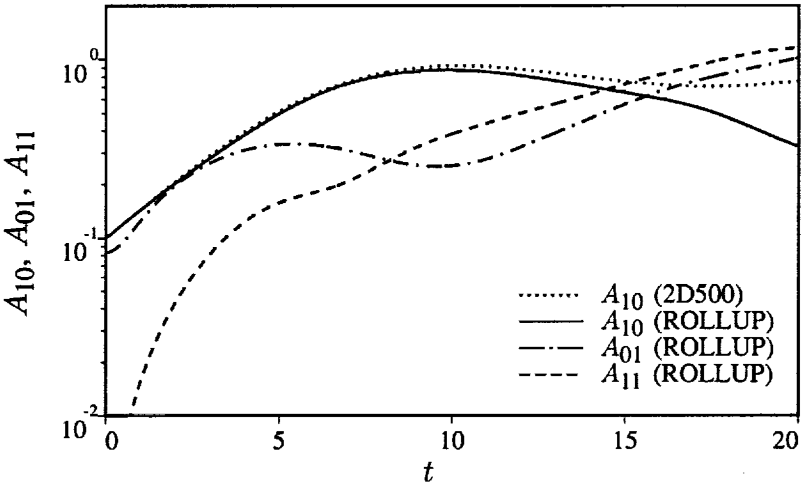

Figure 7. Time development of low-wavenumber amplitudes for ROLLUP and the corresponding two-dimensional flow (2D500).

The evolution of A_{10}, A_{01}, and A_{11} for the ROLLUP simulation is shown in figure 7 along with that of A_{10} from 2D500. The energy development of the two-dimensional fundamental mode is not significantly altered by the presence of the three-dimensional disturbance, particularly for $t < \tau_r$ (the roll-up time). Despite this, the location and magnitude of A_{10}^{sat} are slightly different from their values in the two-dimensional case. For the three-dimensional flow, $\tau_r = 9.8$ (compared with $\tau_r = 10.1$ for the two-dimensional flow), and A_{10}^{sat} is 5% lower. The growth of the STI disturbance is not exponential until $t \approx 0.5$. At this point its growth rate is larger than that of the fundamental two-dimensional disturbance. After this rapid growth, A_{01} also saturates, reaches a minimum near τ_r, and then continuously increases in the oversaturated state. Amplitude A_{11} is also shown. Although initially zero, it grows rapidly and overtakes A_{01} by $t \approx 8$. Shortly after τ_o (oversaturation time), both the oblique and the STI modes become more energetic than the two-dimensional fundamental. The highly three-dimensional structure associated with this energy distribution is described in section 4.2.2.

Figure 8(a) contains the time development of ω_b, defined in the three-dimensional simulations as the maximum (in y) of the spanwise-averaged ω_z in the mid-braid plane. The presence of the three-dimensional disturbance has increased the apparent rate of ω_z depletion from the mid-braid region up to $t \approx 4$. This is primarily a result of the layer becoming corrugated (sec. 4.2.2), so that ω_b, which is a z-average, includes some nearly irrotational regions; the peak ω_z level in the MP is actually higher than that in the two-dimensional case. The oversaturation time, τ_o, occurs sooner in the three-dimensional flow (13.5 vs 14.6), and although ω_b is similar in magnitude to that in the two-dimensional case at τ_o (-0.12 and -0.15), stronger spanwise vorticity is present in the mid-braid region for $t > \tau_o$. This is at least partly a result of stretching (and therefore amplification) of the vorticity that is being brought back into the mid-braid region. The time at which the maximum mid-braid spanwise vorticity suddenly increases (as opposed to the maximum spanwise-averaged value) is virtually identical to τ_o.

The mid-braid strain-rate evolutions are compared in figure 8(b). For the three-dimensional case the maximum principal strain-rate of the spanwise-averaged flow at the mid-braid location is shown. Three-dimensionality decreases the average braid strain-rate level slightly.

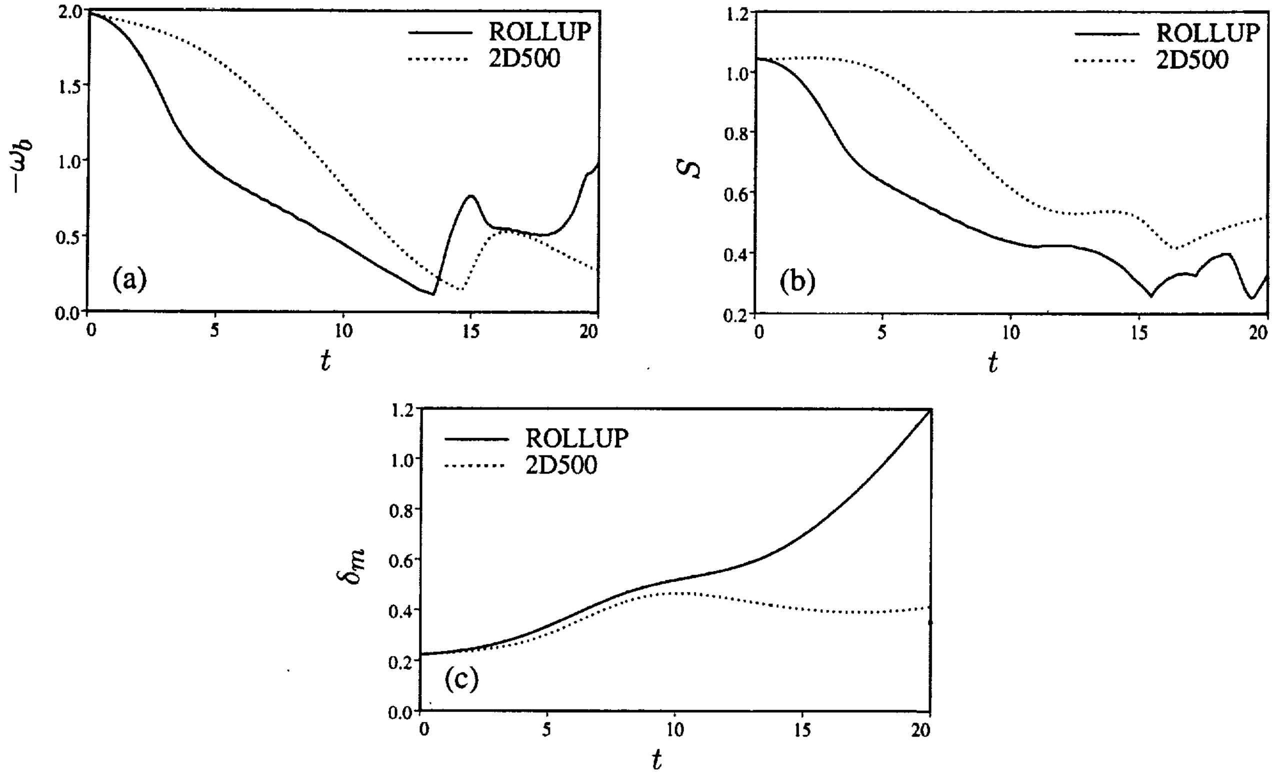

Figure 8. Time development of (a) mid-braid spanwise vorticity, (b) mid-braid strain-rate, and (c) momentum thickness for ROLLUP and the corresponding two-dimensional flow (2D500).

The evolution of the momentum thickness is shown in figure 8(c). The layer is considerably thicker at late times than it was in the two-dimensional cases. The corrugation of the three-dimensional layer and the presence of streamwise "rib vortices" are responsible for this difference.

The development of the vorticity extrema is illustrated in figure 9. In the two-dimensional flow, only ω_z is present and, therefore, the discussion here will be limited to figure 9(a). Unlike in the two-dimensional case, the peak negative ω_z does not decay owing to viscous effects at early times (implying that a small amount of vortex stretching is occurring to offset viscous diffusion). At $t \approx 9$, the peak negative ω_z level begins a rapid increase, indicative of substantial vortex stretching. This behavior will be explained later in terms of flow structures (sec. 4.2.2). The strongest spanwise vorticity reaches 5 times its initial level beyond τ_o. In the two-dimensional flow, the maximum positive vorticity must retain its initial value (zero) for all time. In the three-dimensional flow, positive ω_z appears suddenly at $t \approx 7.8$ for reasons described in section 4.2.3.

4.2.2 Definition of the three-dimensional flow structures– A three-dimensional surface contour plot of the strong vorticity at $t = 12.8$ (a time after τ_r but before τ_o) is shown in figure 10. Some vortex lines are also shown in the figure and the domain has been periodically extended by a factor of 2 in both x and z for clarity. It is apparent that the flow is highly three-dimensional at this point.

The hatched "cup-shaped" surfaces represent spanwise vorticity that is more than twice the peak level associated with the initial mean-error function profile. As a result of vortex stretching, the peak

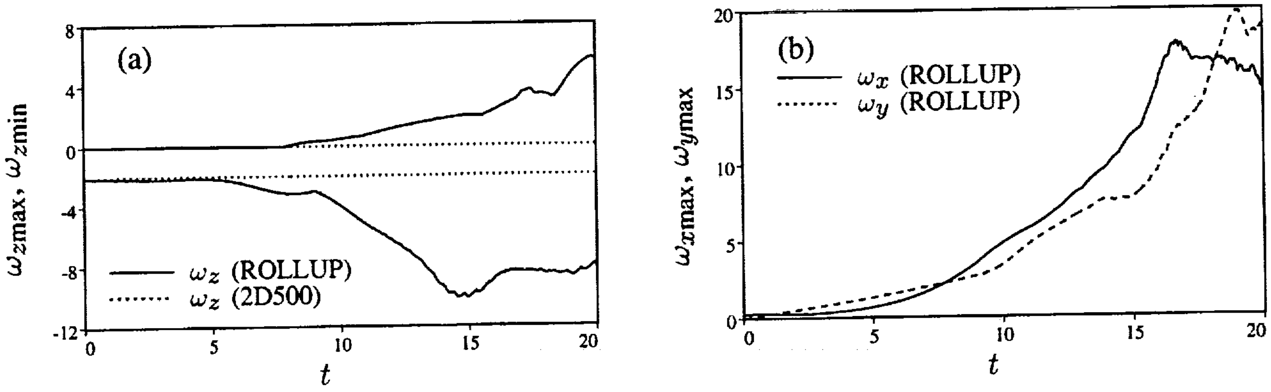

Figure 9. Time development of vorticity component extrema for ROLLUP and the corresponding two-dimensional case (2D500). Note that $\omega_{x\min}$ and $\omega_{y\min}$ are equal in magnitude but opposite in sign to $\omega_{x\max}$ and $\omega_{y\max}$.

spanwise vorticity level within these regions at this time is −7.3 (see fig. 9(a)). Surfaces of lower spanwise-vorticity magnitude (i.e., $\omega_z \approx -1$) reveal a highly corrugated spanwise "roller" connecting the strong ω_z regions shown. Vortex lines traced through the cup vorticity also indicate a corrugated roller (shown in sec. 4.2.5), the "upper" cup being above and slightly downstream of the "lower" cup.

The shaded surfaces shown in figure 10 are regions where $\sqrt{\omega_x^2 + \omega_y^2}$ is greater than 4.0. Each of these regions has ω_x and ω_y of the same sign, but the sign alternates in the z-direction. Vortex lines begun in the MP at or near the center of these "ribs" are superimposed on the contour plot. The alignment of the vortex lines with the shaded regions shows that the streamwise structures are truly "vortices" and not simply regions where some ω_x or ω_y is present. Since the vorticity alternates in sign in z, these are counterrotating vortices. Such structures have been observed in experimental mixing layers by Bernal (1981) and others. The levels of ω_x and ω_y are comparable, which can be deduced from the figure because the vortex lines are inclined at about 40° to the streamwise direction. The slight angle the ribs make with the RP also implies that they have a small ω_z component.

The vortex lines connecting the ribs are separate from those of the spanwise roller and simply connect each rib to its neighbor of opposite sign. In the connection regions, the vortex lines become diffuse (indicating weaker vorticity levels) and primarily spanwise in orientation, with the same sense as the initial mean vorticity. Because of flow symmetry they are perpendicular to the BP. Contour plots of ω_z in the BP (sec. 4.2.4) show a narrow arc-shaped region through which the vortex lines connecting neighboring ribs pass. Because of its shape, this flow structure is referred to as the "wisp." As can be seen in figure 10, the wisps are located on the opposite sides of the roller from the cups.

4.2.3 Details of the rib evolution– Having introduced the key features of the flow (rollers, cups, wisps, and ribs), we can now examine in detail the evolution of the flow. The discussion here focuses on the characteristics of the rib vortices. The roller development is discussed in section 4.2.4.

The point-reflection symmetry (eq. (11)), present in this flow has important consequences regarding the topology of the rib vortices. For the disturbance considered here it implies that the rib centers are fixed at the locations of the extrema of the initial STI disturbance. Thus, in the figures the ribs are centered at the centerline of the MP at $z = L_z/4$ and $z = 3L_z/4$. An additional consequence of this

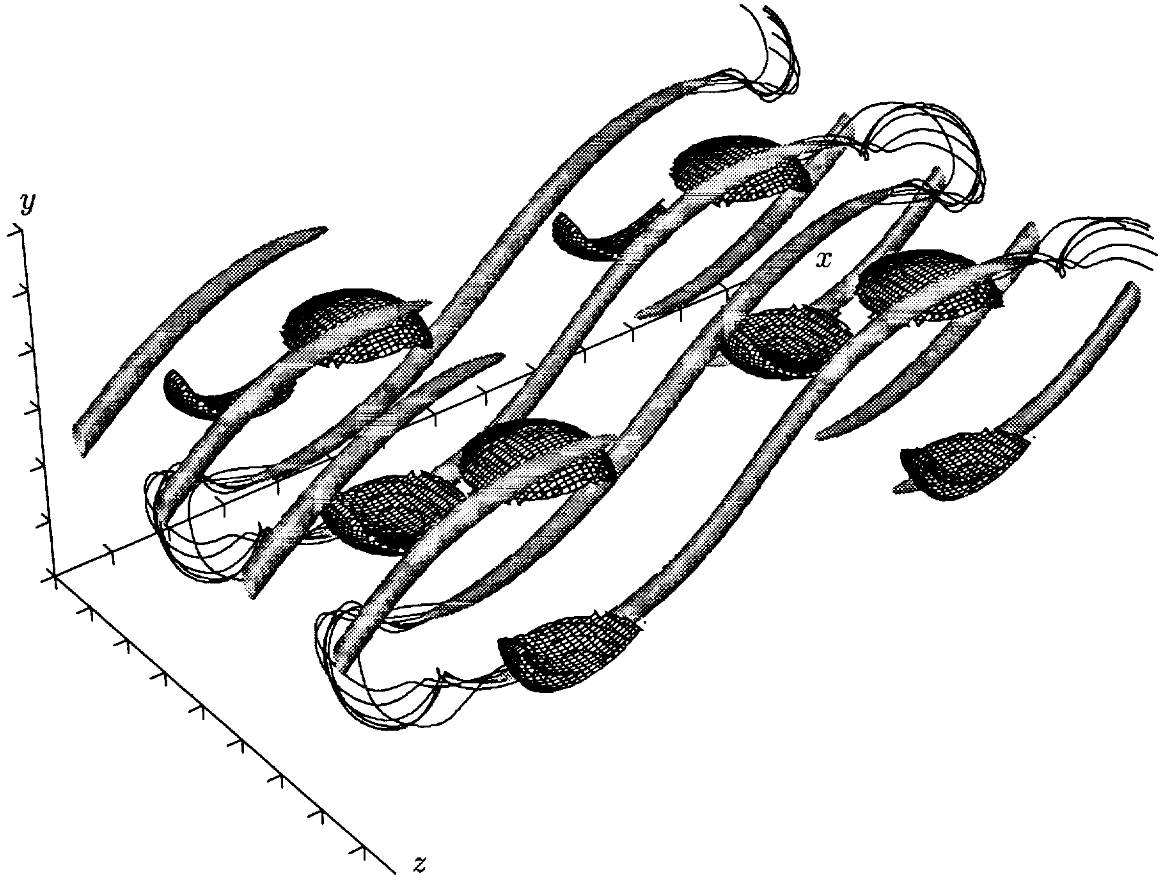

Figure 10. Surfaces of constant vorticity magnitude and vortex lines at $t = 12.8$. Cross-hatched surfaces represent $\omega_z = -4.0$ and shaded surfaces represent $\sqrt{\omega_x^2 + \omega_y^2} = 4.0$. The "rib" structures contain ω_x and ω_y of the same sign, and the sign alternates in z (negative for the closest rib). Periodicity has been used to extend the domain in both the streamwise and spanwise directions, and the same vortex lines go through both of the counterrotating rib vortex pairs (concealed by the rib surface contour). Tic marks are at δ_ω^0 intervals.

symmetry is that rib vortex lines cannot undergo a viscous reconnection process resulting in a vortex ring or loop (vortex lines closing back on themselves) containing the symmetry point. Both the formation of such vortex loops and the movement of the centers of the ribs are observed in the flows discussed in section 4.3.7 where the point-reflection symmetry is broken by the addition of a wake component to the initial mean profile.

Figure 11 shows the time evolution of ω_x and ω_y in the RP (both are identically zero in the BP). The fact that ω_x and ω_y are roughly of the same magnitude in the same regions implies that the vorticity vector is usually inclined at about 45° to the streamwise direction when projected into x-y planes. An exception to this is the core (roller) vorticity at early times. Indeed, the presence of negative ω_x in figure 11(a) is surprising, given that the initial condition consisted of positive ω_x with no x-dependence. Production of this negative ω_x is due to vortex stretching and amounts to a kinking of the spanwise roller vorticity that is opposite to the kinking of the vortex lines in the braid region (the latter being the same as that given by the initial condition). During the early layer development there is competition between the $\omega_z \partial u/\partial z$ and $\omega_y \partial u/\partial y$ stretching terms in the ω_x equation. Since ω_z consists almost

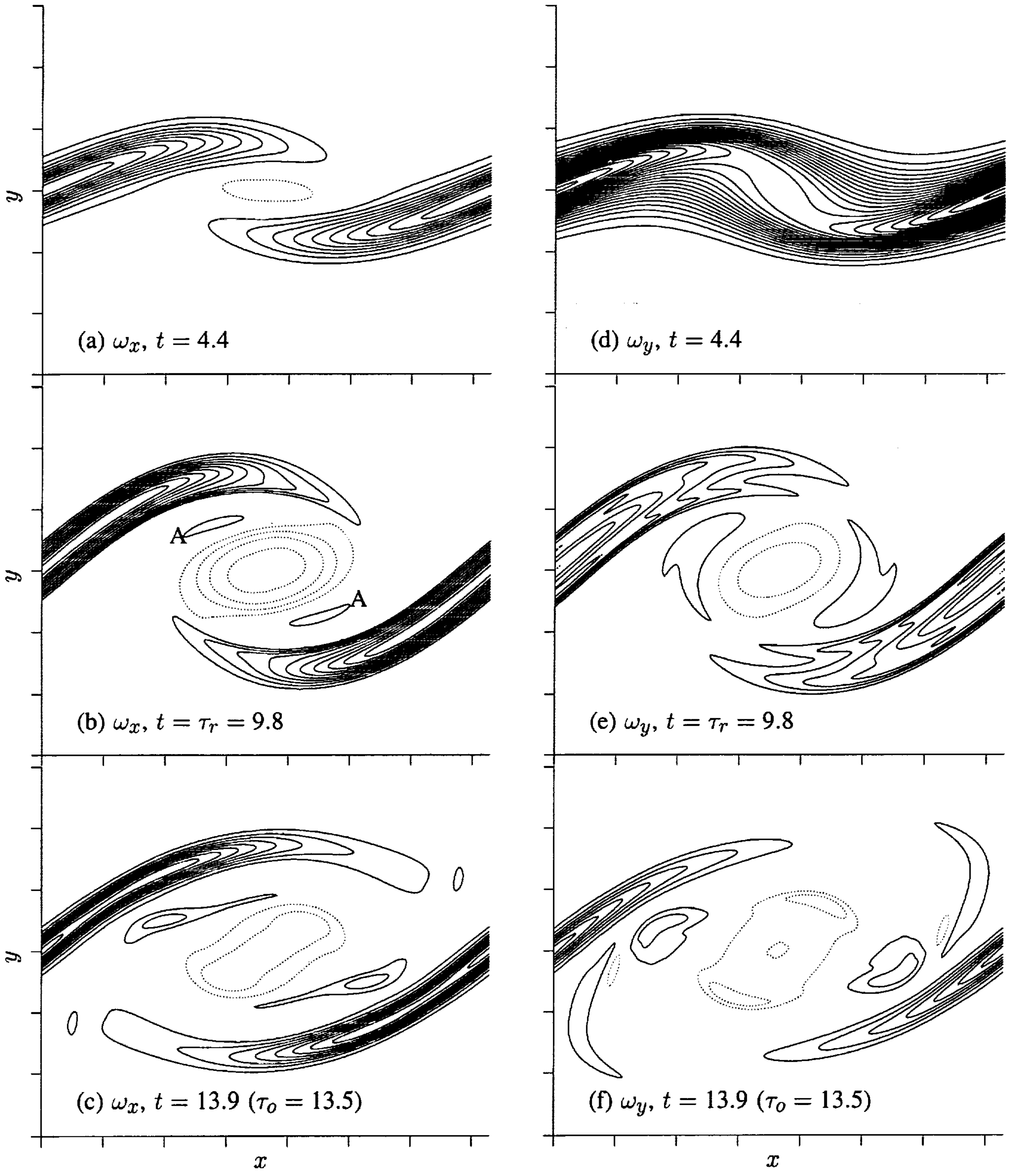

Figure 11. Contour plots of streamwise and normal vorticity in the RP (both are zero in the BP). Contour increments are (a),(d) ±0.05; (b),(e) ±0.4; and (c),(f) ±1.0. Solid contours indicate positive vorticity, dotted contours indicate negative vorticity, and tic marks are at δ_ω^0 intervals.

entirely of $-\partial u/\partial y$ and ω_y is primarily $\partial u/\partial z$, the above two terms are nearly equal in magnitude and opposite in sign. As the roll-up progresses, ω_z is drawn into the roller, and ω_y is strengthened in the braid region. In the roller core, where ω_z is concentrated, the term $\omega_z \partial u/\partial z$ dominates, leading to the production of negative ω_x, as shown in figure 11. In the braid region, where ω_y is growing, the term $\omega_y \partial u/\partial y$ is largest and leads to the generation of positive ω_x, strengthening the initial ω_x at that location.[7] At this time there is no negative ω_y being created by vortex stretching.

The creation of ω_y is also accomplished by vortex stretching (ω_y is zero throughout the domain in the initial condition used here). At early times, the ω_y contours are similar to those of ω_x and ω_z because ω_y is being generated almost entirely by the $\omega_z \partial v/\partial z$ term. Thus, the spanwise variation of vertical velocity kinks the spanwise vortex sheet so that it acquires a vertical vorticity component (see also sec. 4.2.5). Experimentalists (e.g., Huang and Ho 1990; Bell and Mehta 1989a) have taken advantage of this behavior to locate streamwise vortices from spanwise traces of streamwise velocity, which show similar spanwise oscillations. At later times ($t \approx 4.4$), ω_y grows more rapidly in the braid region than in the roller core, with all vortex stretching terms combining to enhance ω_y (the initially zero $\omega_y \partial v/\partial y$ term becomes significant). In the roller core, the other vortex stretching terms counter the growth caused by the $\omega_z \partial v/\partial z$ term. Later still, as the core ω_x becomes negative, the associated $\partial v/\partial z$ changes sign, becoming positive in the core in the RP shown. The $\omega_z \partial v/\partial z$ stretching term thus changes sign and tends to make the core ω_y negative (this is partially reduced by a positive $\omega_x \partial v/\partial x$ in the core). In the braid region, $\omega_x \partial v/\partial x$ and $\omega_z \partial v/\partial z$ combine to increase the magnitude of ω_y (the $\omega_y \partial v/\partial y$ term has also switched sign and is opposite in sign, but only about half the magnitude of this sum, at $t = 6.4$). By τ_r, the ω_x and ω_y distributions are similar, both having core vorticity and rib vorticity that are opposite in sign at a given spanwise (z) location.

The streamwise and normal vorticity components reach magnitudes that are comparable to, and even larger than, those of ω_z (fig. 9(b)). The negative extrema are not shown; they have the same magnitude as the positive extrema because of flow symmetry. The streamwise vorticity shows little growth before $t \approx 4$ and rapid growth thereafter. The normal vorticity component, on the other hand, grows nearly linearly up to $t \approx 9$, after which it too grows rapidly.

In figure 11(b), positive ω_x extends through the ribs and around the roller (at very low levels), and ends in isolated contours labeled A. Vortex lines drawn through the ribs and the isolated contours A are not part of the same vortex structure. Vortex lines drawn from the mid-braid location in the ribs leave this plane at the top and bottom of the roller, as seen in figure 10. The (weak) positive ω_x, labeled A, is associated with predominantly spanwise core vorticity that has been "bent" by vortex stretching, acquiring ω_x and ω_y components of the same sign as the ribs. The vortex lines associated with this core vorticity are also kinked in the same direction as the rib vortex lines. At later times this core vorticity is further strengthened by the strain field at these locations, and the vortex lines become increasingly pulled out into hairpinlike structures. These "sub-rib" structures eventually resemble short streamwise ribs. However, they remain weaker than the ribs and do not extend into the mid-braid region until well past τ_o.

---

[7] Because the $\frac{\partial u}{\partial y}\frac{\partial u}{\partial z}$ term cancels from the sum $\omega_y \frac{\partial u}{\partial y} + \omega_z \frac{\partial u}{\partial z}$ it is instructive to write the vortex stretching term as $\omega_x \frac{\partial u}{\partial x} + \frac{\partial v}{\partial x}\frac{\partial u}{\partial z} - \frac{\partial w}{\partial x}\frac{\partial u}{\partial y}$. In this representation, all three terms are similar in magnitude. In the core, the second term dominates and is aided by the third term, whereas in the braid region, all three terms are nearly equal in magnitude but the last two combine to control the stretching behavior.

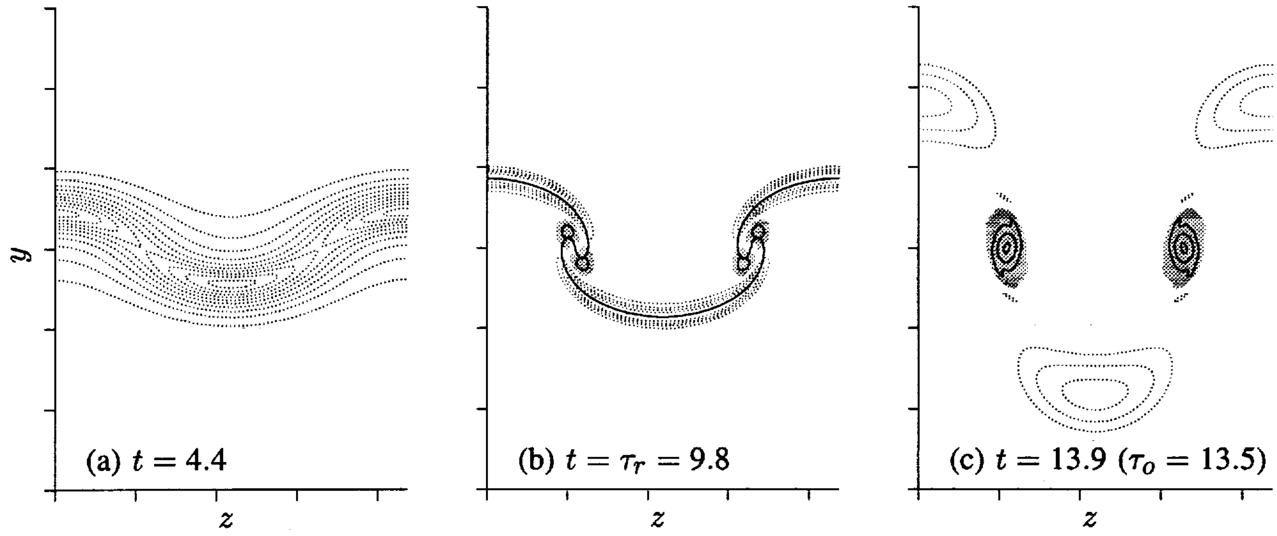

Figure 12. Contour plots of spanwise vorticity (ω_z) in the MP. Contour increments are (a) -0.2; and (b),(c) ± 0.3. In (b), the $T = 0.5$ contour (heavy solid line) has been superimposed on the spanwise vorticity contours. Shaded regions indicate regions of positive ω_z, solid contours indicate positive vorticity, dotted contours indicate negative vorticity, and tic marks are at δ_ω^0 intervals.

The evolution of the ω_z and ω_x vorticity components in the MP is shown in figures 12 and 13, respectively. The early-time evolution of ω_z (fig. 12(a)) shows the corrugation of the vortex sheet by the three-dimensional disturbance. By τ_r (fig. 12(b)), the spanwise vorticity levels in the braid region have been reduced, and some positive ω_z is present where the ribs are located. As mentioned previously, ω_b (fig. 8(a)) is a spanwise-averaged quantity, and because this average is taken over a region including large segments of irrotational fluid, $-\omega_b$ is less than half the peak level of $-\omega_z$ in figure 12(b). The 0.5 contour of the passive scalar quantity is also shown in figure 12(b). At this time, for the Peclet number under consideration ($Pe_0 = Re_0 Pr = 500$), this scalar contour is a good approximation to the material interface initially located at $y = 0$. The developing rib vortices have created a spiral pattern in this interface, and the rib vortex lines assume a similar spiraling component. Where the vortex lines run counter to the mean vorticity a region of weak positive ω_z is apparent. By about τ_o (fig. 12(c)), diffusion has smoothed out the spiraling of the rib vortex lines, and a single region of positive ω_z is found at the rib location. This vorticity is stronger than that present at τ_r (fig. 12(b)) and is associated with bending of the entire rib bundle of vortex lines back against the mean vorticity (discussed further in sec. 4.2.5). The sudden appearance of positive ω_z and its subsequent increase in magnitude was shown in figure 9(a). This positive ω_z is due mainly to the bending (into a horseshoe shape) of the rib vortices as just discussed (although the largest positive ω_z may not be in the MP).[8] Also visible in figure 12(c) is the reentry of spanwise vorticity into the braid region (well above and below the centerline) after oversaturation. At this point, virtually all the negative ω_z present in the MP is a result of this reentry, and the use of ω_b to determine τ_o is thus justified. This negative spanwise vorticity is associated with the wisp connecting neighboring rib vortices and is discussed further in section 4.2.4.

---

[8] Viscosity can also change the vortex line topology such that positive ω_z is created. In this flow, however, this does not occur until late in the flow development, and the resulting positive ω_z is weak.

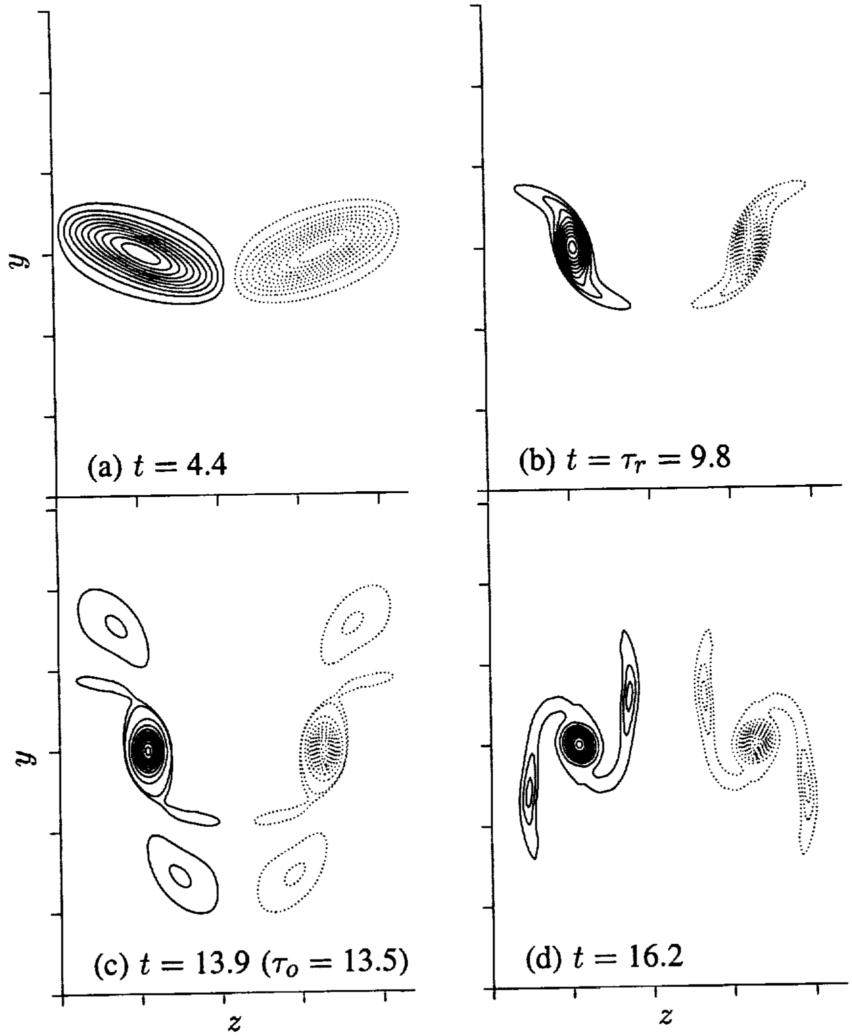

Figure 13. Contour plots of streamwise vorticity in the MP. Contour increments are (a) ±0.05; (b) ±0.4; and (c),(d) ±1.0. In (c), there are four additional contours at ±0.1 and ±0.2, to show the low-level vorticity reentering the braid region. Solid contours indicate positive vorticity, dotted contours indicate negative vorticity, and tic marks are at δ_ω^0 intervals.

The evolution of the streamwise vorticity in the MP is shown in figure 13. The behavior of ω_y is similar, the contour patterns being nearly identical, though the magnitudes may vary depending on the exact angle of the vorticity vector. By τ_o, the streamwise vorticity has collapsed into compact vortices, with a substantial increase in vorticity amplitudes (about a factor of 20 for ω_x). As can be seen in figure 13, this collapse begins by a tilting of the initially elliptical ω_x contours. This is followed by the formation of an S-shaped pattern with a nearly axisymmetric core and eventually ends in complete collapse into a nearly axisymmetric vortex (the cut shown is not perpendicular to the rib and the cross sections therefore appear elliptical).

Lin and Corcos (1984) predicted this behavior by considering a two-dimensional model problem. Intending to mimic the braid region of the mixing layer, they considered an array of counterrotating vortices aligned with the extensional direction of a uniform plane strain with no strain in the spanwise direction. Their predicted behavior is virtually identical to that shown in figure 13 (see fig. 4 in Lin and

Corcos—since ω_x and ω_y are similar, either one can be compared with their "ribwise" vorticity), indicating that this two-dimensional model problem captures the essence of the three-dimensional behavior in the braid region. Their model, which is based on the circulation strength of the ribs, the rib spanwise spacing, the strength of the two-dimensional plane strain, and the Reynolds number, will be discussed further in section 4.3.1, in which other roll-up simulations with different initial three-dimensional disturbance amplitudes are also considered.[9]

The spiral pattern apparent in figure 12(b) occurs only when the rib vortices collapse as described above. Consequently the appearance of positive ω_z is closely related to the collapse. Using the passive scalar as an approximation to the material interface separating the two streams, a "collapse time" τ_c can be defined. At $t = 0$, the scalar contours in the MP are parallel to the z-axis. As the ribs collapse, the scalar MP contour begins to form a spiral as in figure 12(b). The time when the scalar contour at the center of the rib in the MP has been rotated 180° is defined as τ_c (reported in table 2). Note that a vortex line segment at the same location would also be rotated about 180° at this time and therefore would have a positive ω_z component. For $t > \tau_c$, significant positive ω_z is present in the flow (fig. 9(a)).

By $t = 13.9 > \tau_o$, spanwise vorticity has reentered the braid region and the resulting ω_x is visible (at a much lower level than that of the main rib) away from the centerline (fig. 13(c)). This ω_x is stronger at $t = 16.2$ and, because it has the same sign, gets wound into the rib, forming a lobed pattern (fig. 13(d)).

The sudden reentry of vorticity into the braid region is accompanied by a sudden increase in rib (or more precisely MP) circulation, an important parameter in the Lin and Corcos model of the ribs. Figure 14 portrays the evolution of the streamwise circulation,

$$\begin{aligned}\Gamma_x &= \int_{y=-\infty}^{\infty}\int_{z=0}^{\lambda_z/2} \omega_x \,\mathrm{d}z\mathrm{d}y = -\int_{y=-\infty}^{\infty}\int_{z=0}^{\lambda_z/2} \frac{\partial v}{\partial z}\,\mathrm{d}z\mathrm{d}y \\ &= -\int_{y=-\infty}^{\infty} v(y, z = \lambda_z/2) - v(y, z = 0)\,\mathrm{d}y \end{aligned} \tag{12}$$

at various streamwise locations. The circulation over the other spanwise half of the computational domain is equal and opposite by symmetry. This circulation is the same as that obtained by integrating the vorticity component along the rib over the plane normal to the rib in the limit of infinitesimal rib cross section. Thus, especially in the collapsed state, Γ_x should be a reasonable approximation to Γ_{rib}. By manipulating the Navier–Stokes equations, the governing equation for Γ_x can be obtained (for simplicity the inviscid case is considered here):

$$\frac{\partial \Gamma_x}{\partial t} = \int_{y=-\infty}^{\infty} (u\omega_z)\,\mathrm{d}y\Big|_{z=0}^{\lambda_z/2} = \int_{y=-\infty}^{\infty} (u\frac{\partial v}{\partial x})\,\mathrm{d}y\Big|_{z=0}^{\lambda_z/2} \tag{13}$$

Since $u\omega_z$ has no spanwise variation in the initial condition, the initial growth rate of Γ_x is zero in the absence of viscosity. Also, when ω_z is completely removed from a given streamwise location, Γ_x cannot increase at that location. The removal of spanwise vorticity from the mid-braid region seen in figure 8(a) results in a plateau in figure 14 extending from $t = \tau_r$ to $t = \tau_o$ (for the mid-braid

---

[9] The reason for examining the mid-braid strain-rate behavior shown in figure 8(b) is now clear; it has a large effect on the collapse behavior of the rib vortices.

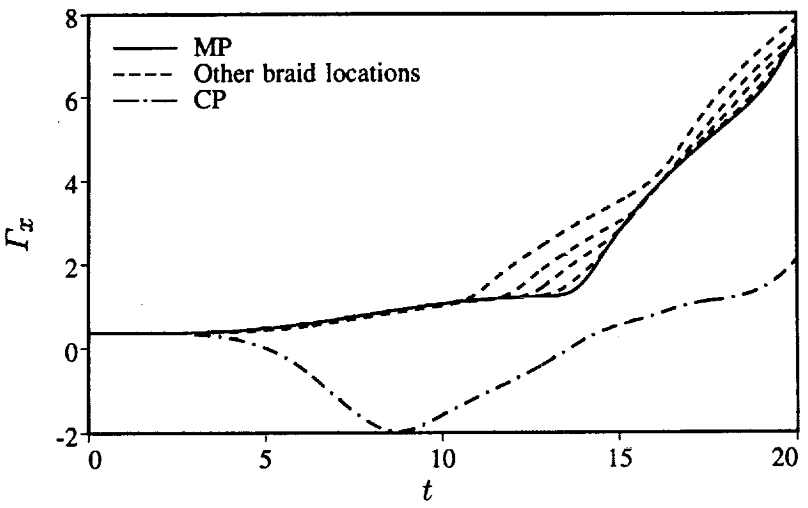

Figure 14. Time development of streamwise circulation. Dashed lines are for various braid region locations progressively farther from the MP as the curves move away from the solid line.

curve). The sudden increase in Γ_x occurs sooner for braid planes farther from the MP because the wisp spanwise vorticity reenters them sooner.

In equations (12) and (13) the spanwise locations $z = 0$ and $z = \lambda_z/2$ are the BPs on either side of a rib. The symmetry given by equation (10) implies that ω_x and ω_y are zero in these planes, which makes them a natural choice as boundaries for calculating the rib circulation. The symmetry given by equation (11) implies that the ω_z pattern in the $z = \lambda_z/2$ BP is the same as that in the $z = 0$ BP when reflected in x and y. This fact can be used to simplify equations (12) and (13) for flows that possess the symmetry in equation (11) (as ROLLUP does). In particular, equation (12) becomes

$$\Gamma_x = 2\int_{y=-\infty}^{\infty} v(y, z = 0)\,\mathrm{d}y \tag{14}$$

and equation (13) becomes

$$\frac{\partial \Gamma_x}{\partial t} = -2\int_{y=-\infty}^{\infty} (u\omega_z)(y, z = 0)\,\mathrm{d}y \tag{15}$$

From equation (15) it is clear that a change in the circulation Γ_x can only occur (inviscidly) when there is ω_z in the BP where $u \neq 0$ (away from the centerline). The spanwise vorticity in the BP is discussed in section 4.2.4. For study of circulation in the MP, the $u\omega_z$ distribution on the left boundary ($z = 0$ BP) of figure 12 is used in equation (15). At $t = 0$ (not shown), the spanwise vorticity is symmetrically distributed about the centerline, whereas u is distributed antisymmetrically. Integrating their product in y thus yields zero and, as noted above, $\partial \Gamma_x^{\mathrm{MP}}/\partial t$ is initially zero. As the layer develops, the motion induced by the ribs moves the spanwise vorticity above the centerline, and the y-integral of $-u\omega_z$ becomes positive. As can be seen from equation (15), this implies that the circulation of the (positive circulation) rib increases. (The actual Γ_x^{MP} growth is small because the y-location of $u = 0$ also moves up). When the wisp (consisting of the vortex lines connecting neighboring ribs) reenters the braid region, ω_z is present well above the $u = 0$ y-location. This results in the rapid growth of Γ_x^{MP} for $t > \tau_O$.

A better understanding of the above circulation growth mechanism can be obtained by considering the behavior of vortex lines in the flow. By regarding the rib as a collection of vortex lines, it is clear that its circulation can only increase if other vortex lines are brought into the rib bundle. Because of the symmetry given by equation (10), each rib vortex line is connected to the neighboring rib; that is, the rib bundle consists of many hairpinlike vortex filaments. To increase the MP rib circulation, additional hairpinlike filaments must be brought through the MP to combine with the existing rib. The wisp spanwise vorticity associated with the tip of the hairpin filament (located in the BP between the two ribs) must cross the MP before this can happen. Note that it is exactly this spanwise vorticity that appears in equation (15) for $\partial \Gamma_x / \partial t$. Without new BP spanwise vorticity (hairpin filament heads) crossing the MP, the circulation Γ_x^{MP} cannot increase. Also, if a hairpin vortex filament with legs with signs opposite those of the ribs crosses the MP, the circulation will decrease. Just before τ_o, virtually all the vorticity present in the braid region is already in a collapsed rib vortex, and no new filaments are available to increase the circulation. However, as the wisp crosses the MP a large supply of vortex lines becomes available again. Note that the arrival of the wisp in a given braid region signifies that rib vortex lines from the neighboring braid region (upstream or downstream periodic images in this case) are present in addition to the original rib lines.

According to the above description, the MP circulation should approximately triple after τ_o. This is simply because any given MP will then have rib vortex lines from an upstream and a downstream rib, as well as the rib centered in that plane. The time required to achieve the full factor-of-3 growth will be the time required to pull all the hairpin vortex filaments through the MP. By $t \approx 16$ (only $\Delta t = 2.5$ after τ_o), the portion of the wisp containing the rib vortex lines has been pulled through the MP. At this time, all the curves for Γ_x (fig. 14) at the five streamwise locations that are considered approach a value of 3.8. This recombination of the Γ_x curves implies that there is no streamwise variation in circulation at this time and that no new nearby vortex filaments are still being pulled toward the MP. Indeed, the value 3.8 is close to 3 times the plateau value of Γ_x ($\Gamma_x^{\mathrm{MP}}(t = \tau_o) = 1.3$).

For $t > 16$, the five curves in figure 14 again separate as the vortex lines associated with the sub-rib (which are connected in a second wisp structure discussed in section 4.2.4) enter the MP, bringing even more hairpin vortex filaments to augment the circulation. It is difficult to define a circulation associated with the sub-rib structures, because no symmetries can be taken advantage of to clearly define the area over which the circulation should be computed. From the continued growth of Γ_x^{MP} when $t > 16$, it would appear that the sub-rib circulation is comparable to the rib circulation by the time it is pulled through the MP. By $t = 20$, the circulation Γ_x^{MP} reaches 7.4 and is a significant fraction of the roller core circulation $\Gamma_z = \Delta U \lambda_x = 14.6$. Thus, a significant fraction of core vorticity has been pulled through the braid region.[10]

4.2.4 Details of the roller evolution– Figure 15 shows the time development of the spanwise vorticity in both the BP and the RP. The early-time vorticity distribution shown in figure 15(d)(RP) is similar to that of the two-dimensional roll-up at the same time. The roller is symmetric (required at this spanwise location by the symmetry of the initial condition), and vorticity is being drawn from the braid region into the spanwise roller. However, there is already evidence of three-dimensionality in the BP (fig. 15(a)). The contours are asymmetric, and the level of ω_z is not decreasing in the braid region.

---

[10] Note that of this 7.4, 3.5 is associated with core vorticity since 3(1.3) is associated with rib structures. Thus the fraction of core vorticity pulled through the MP is $3.5/(14.6 - 1.3) = 0.26$.

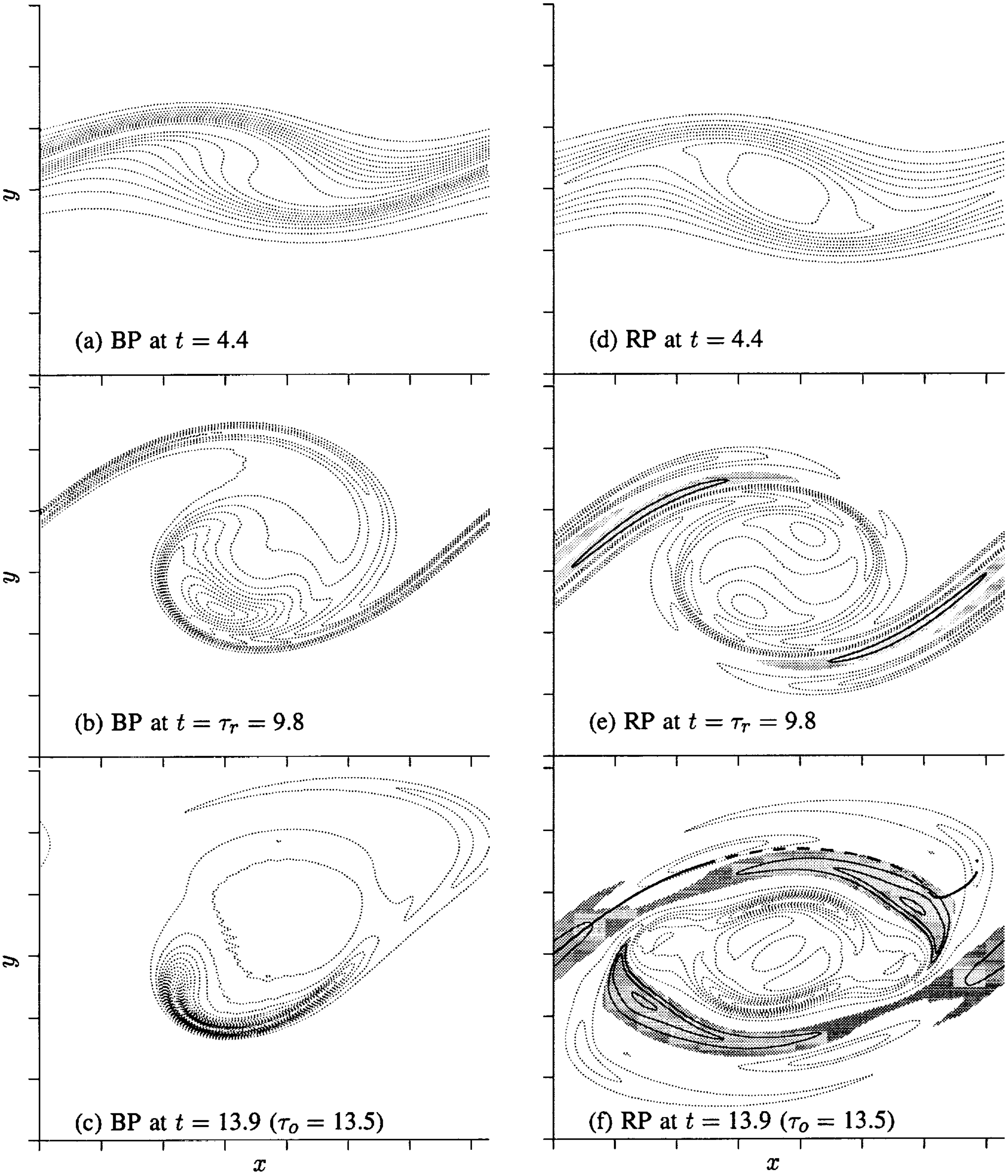

Figure 15. Contour plots of spanwise vorticity in the BP and RP. Contour increments are (a),(d) -0.2; (b),(e) ± 0.3; and (c),(f) ± 0.5. The heavy line in (f) is a vortex line through the mid-braid symmetry point; the dashed portion is behind the plane shown. Shaded regions indicate regions of positive ω_z (opposite in sign to the mean vorticity), solid contours indicate positive vorticity, dotted contours indicate negative vorticity, and tic marks are at δ_ω^0 intervals.

Spanwise vorticity is being advected into the roller, but at the same time vortex stretching is amplifying the braid vorticity. This stretching is due to the strain field established by the forming ribs. In the BP this stretching is entirely owing to $\omega_z \partial w/\partial z$; in the RP it is weaker and predominantly $\omega_y \partial w/\partial y$.

At $t = 9.8 = \tau_r$ (figs. 15(b), 15(e)), the roller of spanwise vorticity is roughly circular. Vortex stretching has had a marked effect on the ω_z distribution in the BP (fig. 15(b)). The peak spanwise vorticity level, $\omega_z = -3.73$, is approaching twice the initial maximum. In addition, vortex stretching is depleting spanwise vorticity from the upper half (lower half in the other BP) of the roller and is concentrating spanwise vorticity in the cup-shaped regions described previously. The strongest mid-braid ω_z in the BP has a value of -1.39. At the same time, the RP contains a double structure of spanwise vorticity. The two maxima in the roller core are associated with the two neighboring spanwise cups (see fig. 10). The double-braid structure is likewise a cut through two adjacent braid ω_z structures (see fig. 12(b)). In between these two braid structures is the region of positive (peak level 0.40) ω_z described in section 4.2.3.

At $t = 13.9$ (figs. 15(c), 15(f)), just after $\tau_o = 13.5$, the flow is similar to that shown in figure 10. In the BP, the peak ω_z reaches -9.30 in a well-defined cup. In addition, there are two wisps of spanwise vorticity. The first, wisp 1, is stronger (peak level -1.20) and is reentering the mid-braid region. This is the wisp that contains the spanwise vorticity connecting neighboring ribs. The second, wisp 2 (peak level -0.98; however, this level increases to -2.08 by $t = 16.2$), forms a semicircular arc opposite the cup at this time. Wisp 2 consists of spanwise vorticity connecting the sub-ribs visible in figure 11 and described in section 4.2.3.[11] The remainder of the BP is essentially irrotational (ω_x and ω_y are zero by symmetry in this plane). In the RP at this time (fig. 15(f)) there is a complicated pattern of ω_z. The strong core ω_z is from two adjacent cups, as in figure 15(e). The remaining contours are all associated with the ribs. In this oversaturated state the vortex lines connecting the ribs are horseshoe-shaped. The angles formed with the z-direction result in significant ω_z, including a region of positive ω_z close to the cups. A typical vortex line going through these contours is shown in figure 15(f).

The time evolution of the spanwise vorticity in the CP is presented in figure 16. At $t = 4.4$ (fig. 16(a)), the spanwise roller undulates because of the spanwise variation of vertical velocity described previously, and there is some spanwise variation in peak ω_z level. By τ_r (fig. 16(b)), the cups have begun to form (alternating between the top and bottom of the layer in the spanwise direction, as shown in fig. 10). In addition, the spanwise vorticity associated with the braid region wraps over the top and under the bottom of the roller. This results in a pattern similar to that in figure 12(b) above and below the roller core in figure 16(b).[12] As can be seen in figure 10, the upper cup is downstream of the lower cup. Because of this, the peak levels of cup spanwise vorticity do not occur in the CP. At this time, the extremum in the CP is -2.76 and the peak is -3.73. The peak occurs downstream of this plane for the

---

[11] The sub-rib vortex lines are not symmetric around their midpoints as are the rib vortex lines in this flow. Because of this, a sub-rib vortex line does not go through the same place in the BPs on either side of it. At late times ($t \approx 16$), sub-rib vortex lines go through the center of wisp 2 in one BP and through the region joining wisps 1 and 2 in the other BP.

[12] Note: this implies that at low contour levels the roller will appear kinked in the opposite direction of the vortex lines connecting the cups. Contours of the passive scalar quantity in the CP show a pattern similar to that of figure 16(b). Similar patterns have been observed in the roller core in flow visualizations of experimental mixing layers (e.g., Lasheras, Cho, and Maxworthy 1986, figure 12, frames 10–15; Lasheras and Choi 1988, figure 8, frames 5–14).

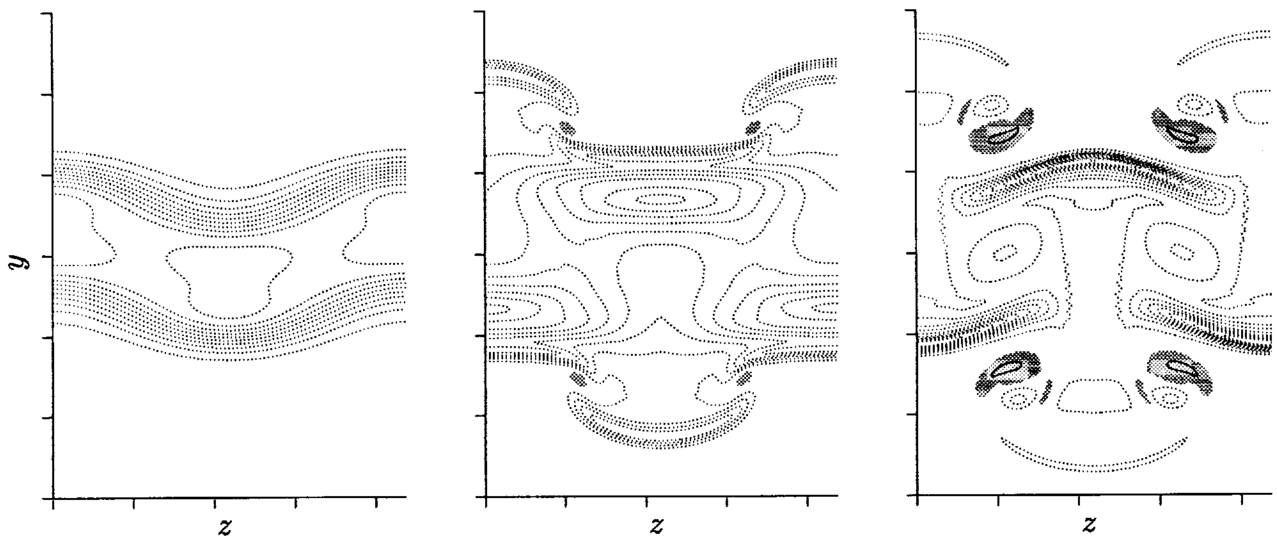

(a) $t = 4.4$ (b) $t = \tau_r = 9.8$ (c) $t = 13.9$ ($\tau_o = 13.5$)

Figure 16. Contour plots of spanwise vorticity in the CP. Contour increments are (a) −0.2, (b) ±0.3, and (c) ±0.6. Shaded regions indicate regions of positive ω_z (opposite in sign to the mean vorticity), solid contours indicate positive vorticity, dotted contours indicate negative vorticity, and tic marks are at δ_ω^0 intervals.

upper cup and upstream for the lower cup.[13] At later times (fig. 16(c)), the general pattern is similar. The cups, however, have become more concentrated with larger magnitude vorticity. This concentrating and strengthening by the strain field apparently continues until an equilibrium with viscous diffusion is reached.

The vortex-stretching mechanism that generates the cup structures can be understood by examining contours of ω_x in the CP (fig. 17). Throughout the evolution of the layer, the core distribution of ω_x consists primarily of ribs from the upstream braid region above the roller, ribs from the downstream braid region below the roller, and opposite-sign ω_x in the roller core itself (the evolution of this core vorticity was described in section 4.2.3 in the context of rib formation). This effectively forms two "quadrupoles" (the core vorticity being associated with both) centered in each BP. At the center of one of these quadrupoles, vortex stretching is enhancing the spanwise vorticity levels; at the other, compression is weakening it. Note that at the neighboring BPs, the sign of the quadrupoles is reversed. This results in cups alternating from the top to the bottom of the roller core as one moves in the spanwise direction. The stagnation point associated with each quadrupole prevents the highly stretched vorticity from being advected away, and thus allows the ω_z levels to continuously increase in time (figs. 16, 9(a)).

The value of Γ_x for the CP is shown in figure 14. Initially constant, it changes sign as the bulk of the core ω_x becomes negative. The fact that the total circulation (combining the core and rib tips above and below it—see fig. 17(b)) becomes negative indicates that the core circulation is more than twice that of the ribs at this streamwise location. Because of this, the "quadrupole" is not symmetric and the net induced motion at the center of the quadrupole tends to give the cup its cuplike shape. The same

---

[13] The streamwise distance between the cup maxima at τ_r is 1.4 ≈ 0.2 λ_x; the vertical separation is 1.3. Both increase by a factor of 1.7 by t = 13.9.

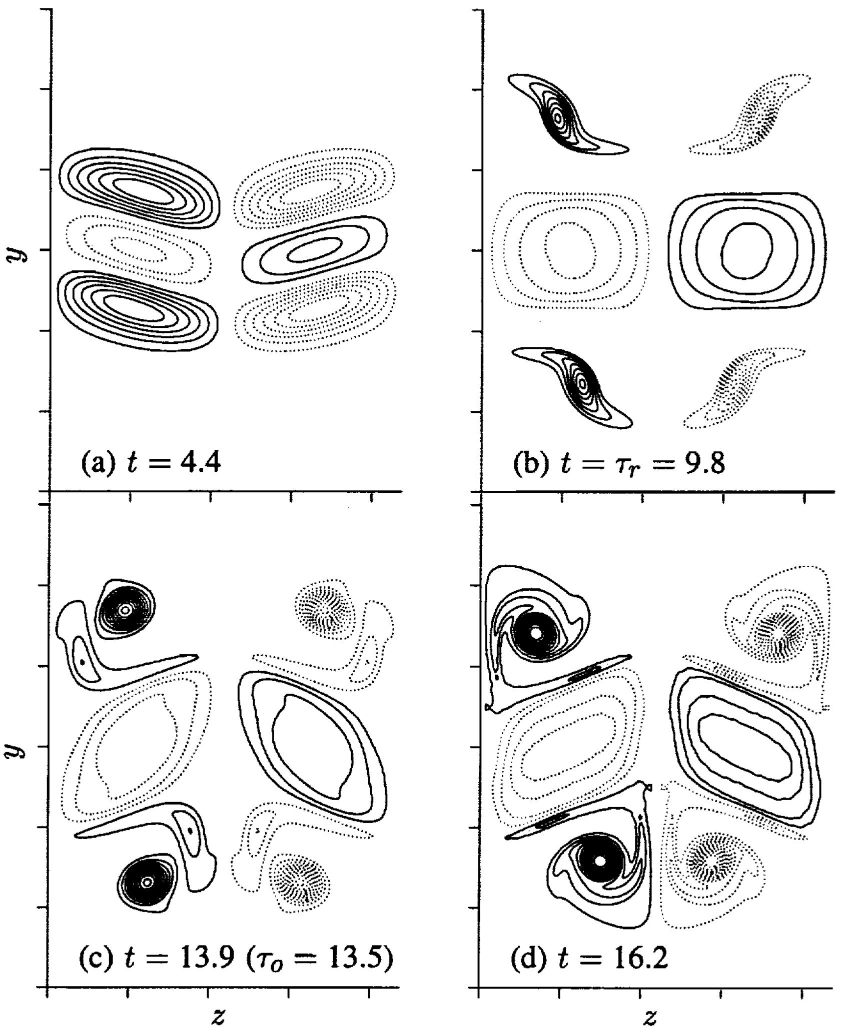

Figure 17. Contour plots of streamwise vorticity in the CP. Contour increments are (a) ±0.02; (b) ±0.4; and (c),(d) ±0.6. Solid contours indicate positive vorticity, dotted contours indicate negative vorticity, and tic marks are at δ_ω^0 intervals.

vortex dynamics have been observed in Buell and Mansour's (1989a) direct numerical simulations of spatially developing mixing layers. At later times the core vorticity is not as dominant, and for $t > \tau_o$ the CP circulation is again positive.

4.2.5 Summary of ROLLUP evolution– The vortex lines associated with the spanwise roller and the streamwise ribs are shown in figure 18 and are discussed here to summarize the evolution of this typical three-dimensional, plane mixing-layer roll-up. At early times, ω_y develops rapidly. In the core region, ω_x is being reduced, leaving a spanwise core that is bent predominantly in the vertical direction (fig. 18(a)). The braid region ω_x is enhanced by stretching, but the ω_y in this region is growing faster, resulting in vortex lines that are also kinked predominantly in the vertical direction (fig. 18(d)). By τ_r, the Kelvin–Helmholtz roll-up is substantially completed. Vortex stretching has produced significant ω_x and ω_y in the roller core that is opposite in sign to the rib vorticity at the same spanwise location. This implies that the spanwise roller is bent in a direction opposite to the vortex lines connecting the rib

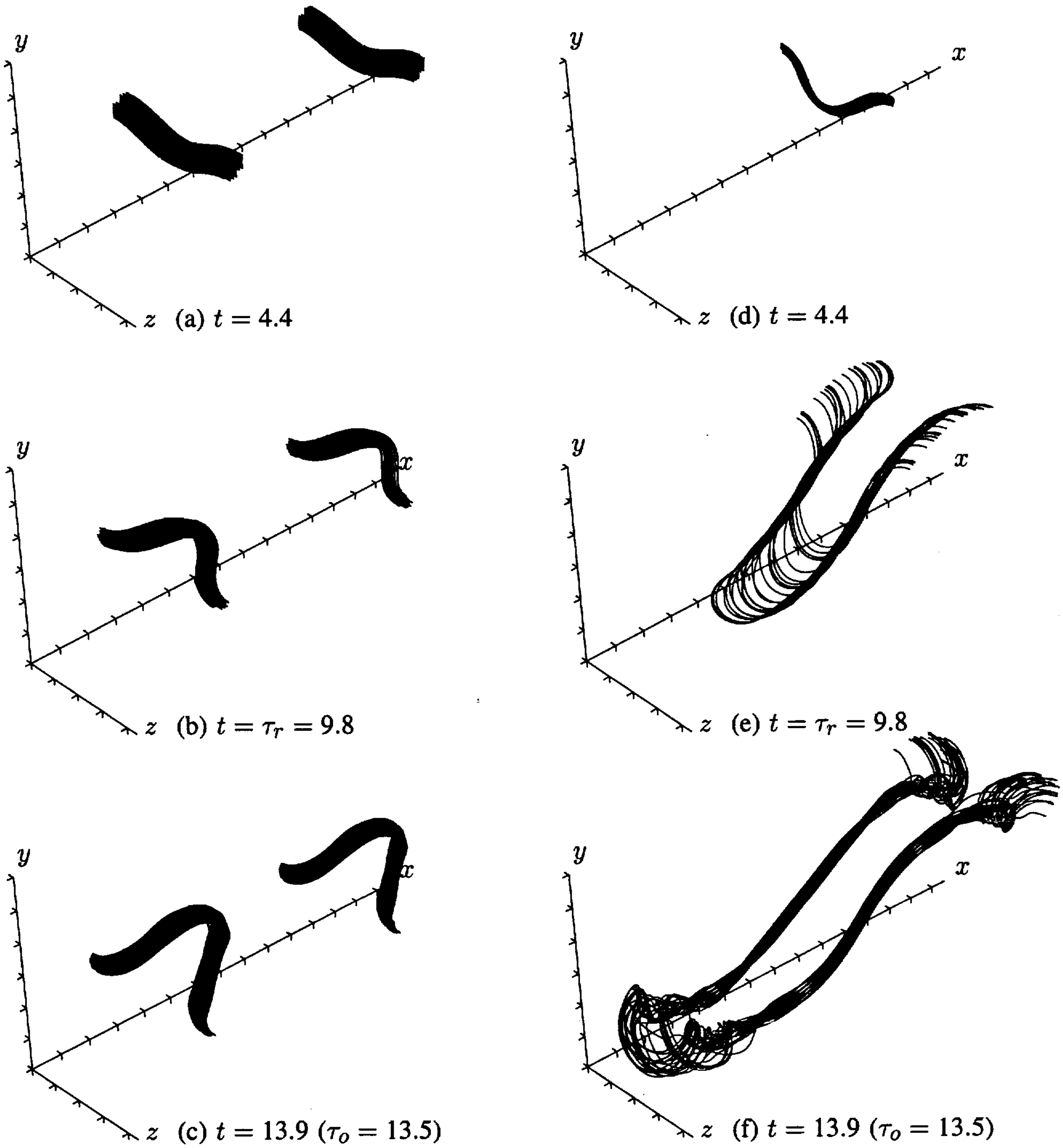

(a) $t = 4.4$ (d) $t = 4.4$

(b) $t = \tau_r = 9.8$ (e) $t = \tau_r = 9.8$

(c) $t = 13.9$ ($\tau_o = 13.5$) (f) $t = 13.9$ ($\tau_o = 13.5$)

Figure 18. Vortex lines (a)–(c) through the roller core and (d)–(f) through the ribs. Periodicity has been used to double the extent of the streamwise domain, and tic marks are at δ_ω^0 intervals.

vortices (figs. 18(b), 18(e)).[14] The streamwise vorticity is now larger than the vertical vorticity (although they are comparable), and the rib structures are angled at about 40° to the streamwise direction. In the braid region the vortex lines are compact, indicative of the collapse of the rib vortices. The connection to neighboring ribs is more diffuse (fig. 18(e)), resulting in a wisp of low-level spanwise vorticity in the BP. As time progresses, the rib vortices extend farther in the streamwise direction. They also become less confined to the RP and acquire a spanwise vorticity component. The hairpinlike vortex lines connecting adjacent ribs become horseshoe or Ω-shaped near the tips (fig. 18(f)) (this evolution is typical of isolated hairpin vortices in a wide variety of shear flows; e.g., see Moin, Leonard and Kim (1986)). The outward bulging vortex lines of this horseshoe structure have a significant ω_z component, as can be seen in figure 15(f). Some of the vortex lines are helical or spiraling in this region. The mid-braid part of the rib is also angled in the spanwise direction at this point, resulting in positive ω_z (fig. 12(c)). As shown in figure 18(c), the spanwise roller continues to be stretched in the streamwise and vertical directions, becoming more kinked in regions of strong vortex-stretching between the ribs. In these regions, cups of strong spanwise vorticity are located. These cups, which cannot form in two-dimensions because of the absence of vortex stretching, play an important role in the transition to turbulence, as will be seen in Part 2.

4.3 Variation of Initial Parameters

4.3.1 Initial rib circulation– The highly three-dimensional state shown in figure 10 results from a streamwise vorticity disturbance with a circulation of only one fortieth of that associated with the spanwise vorticity in a single roller. Given the difficulty in measuring such low vorticity levels in experiments, it is not clear whether the disturbance strength of the case described in section 4.2 is comparable to that observed in experiments, though crude experimental estimates by Jimenez (1983) and Bell and Mehta (1990) of the rib circulation in the early development of mixing layers are in good agreement with the plateau level of rib circulation shown in figure 14. In order to examine how sensitive the flow evolution is to the initial three-dimensional disturbance strength, two additional cases with $\Gamma_x^0/\Gamma_z = 0.005$ (LOROLL) and $\Gamma_x^0/\Gamma_z = 0.100$ (HIROLL) were run with the remaining initial condition parameters exactly as in the "typical" case (ROLLUP) described in section 4.2. This represents a factor of 5 decrease and a factor of 4 increase over the $\Gamma_x^0/\Gamma_z = 0.025$ value for ROLLUP.

The developed flow field (t just past τ_r) for the LOROLL simulation is shown in figure 19. It resembles the ROLLUP flow described in section 4.2 in many ways, although the three-dimensionality is reduced. The BP (fig. 19(a)) shows the concentration of spanwise vorticity into a weak cup, which is not very cup-shaped at this time. This in turn results in a corrugated roller (fig. 19(d)). As with ROLLUP, the RP (fig. 19(b)) shows both ribs and sub-ribs together with core streamwise vorticity opposite in sign to the ribs. The MP streamwise vorticity distribution, however, is different from that of figure 13(b), showing no evidence of the collapse described in section 4.2.3. Although the contours in figure 19(b) indicate a long riblike region of ω_x, vortex lines drawn through these points do not stay confined to the RP. Instead, they form hairpinlike bends with a significant streamwise component and a total streamwise extent that is about a third of what appears to be the rib in figure 19(b). This behavior, in which the vorticity vectors are not aligned with the contour surfaces, is typical of weakly three-dimensional flows with "noncollapsed" ribs.

---

[14] This behavior has been nicely documented in experimental mixing layers by Lasheras and Choi (1988).

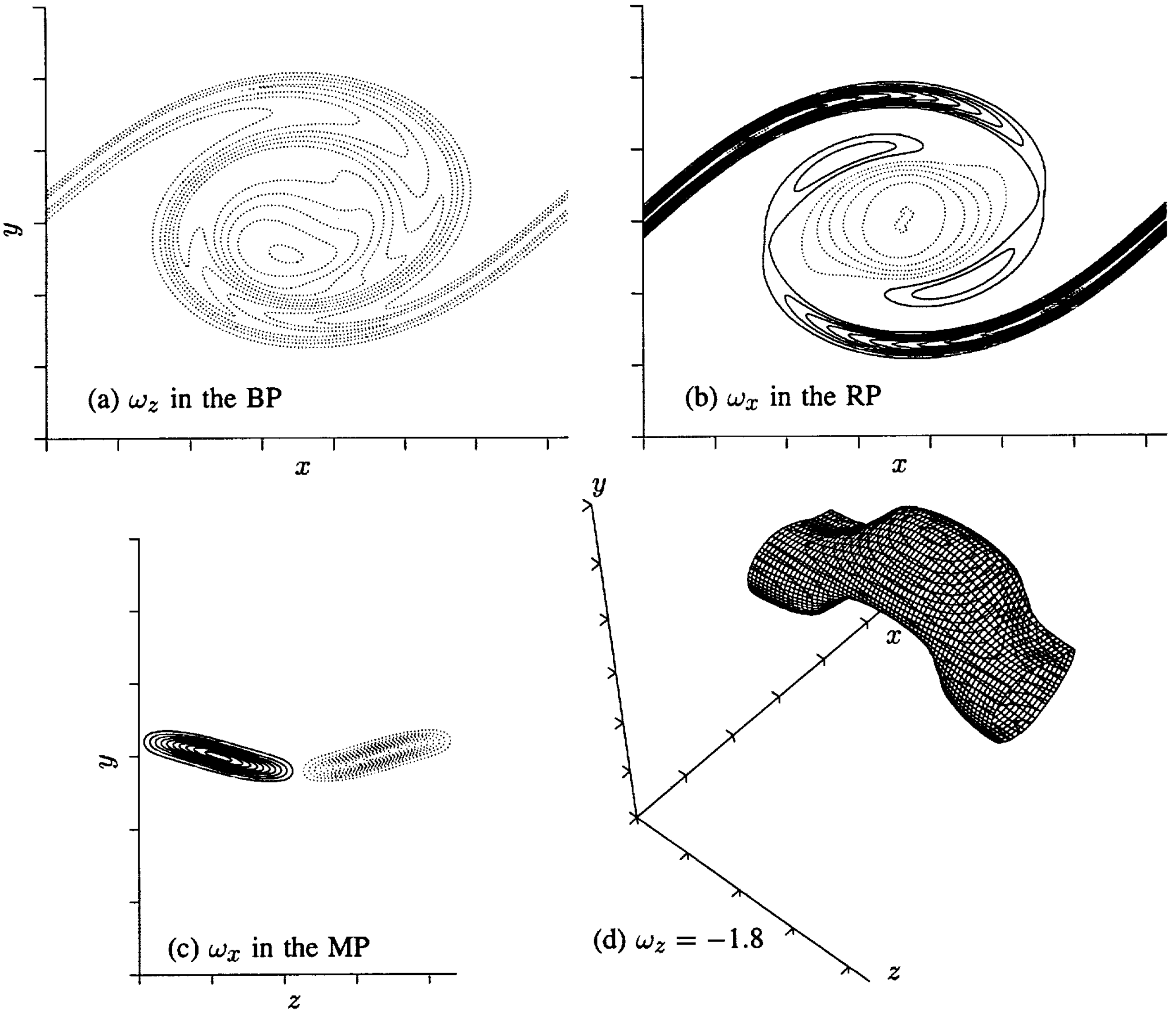
(a) ω_z in the BP

(b) ω_x in the RP

(c) ω_x in the MP

(d) $\omega_z = -1.8$

Figure 19. Contour plots for LOROLL at $t = 10.5$ ($\tau_r = 10.1$). Contour increments are (a) -0.2; and (b),(c) ± 0.06. Solid contours indicate positive vorticity, dotted contours indicate negative vorticity, and tic marks are at δ_ω^0 intervals.

Contour plots from the HIROLL simulation are shown in figures 20 to 22. The typical flow structures are again visible, although the flow is more three-dimensional than the ROLLUP flow. By τ_r, the BP (fig. 20(a)) shows a pronounced cup of spanwise vorticity, a largely irrotational core region, and a wisp of spanwise vorticity opposite the cup. Note that in HIROLL the cup is oriented mostly vertically (instead of horizontally as in ROLLUP), resulting in a corrugated roller (fig. 20(c)) bent primarily in the streamwise instead of the cross-stream direction.[15] The RP (fig. 20(b)) shows the usual pattern of core ω_x opposite in sign to the rib vorticity in the same plane. The sub-rib has ω_x of both signs, implying more complicated vortex-line structure than that of ROLLUP. As can be seen in figures 20(b) and 21, the ribs in HIROLL are nearly as large as the core at this point. They are also clearly collapsed, although

---

[15] Note that there are additional concentrations of spanwise vorticity between the cups.

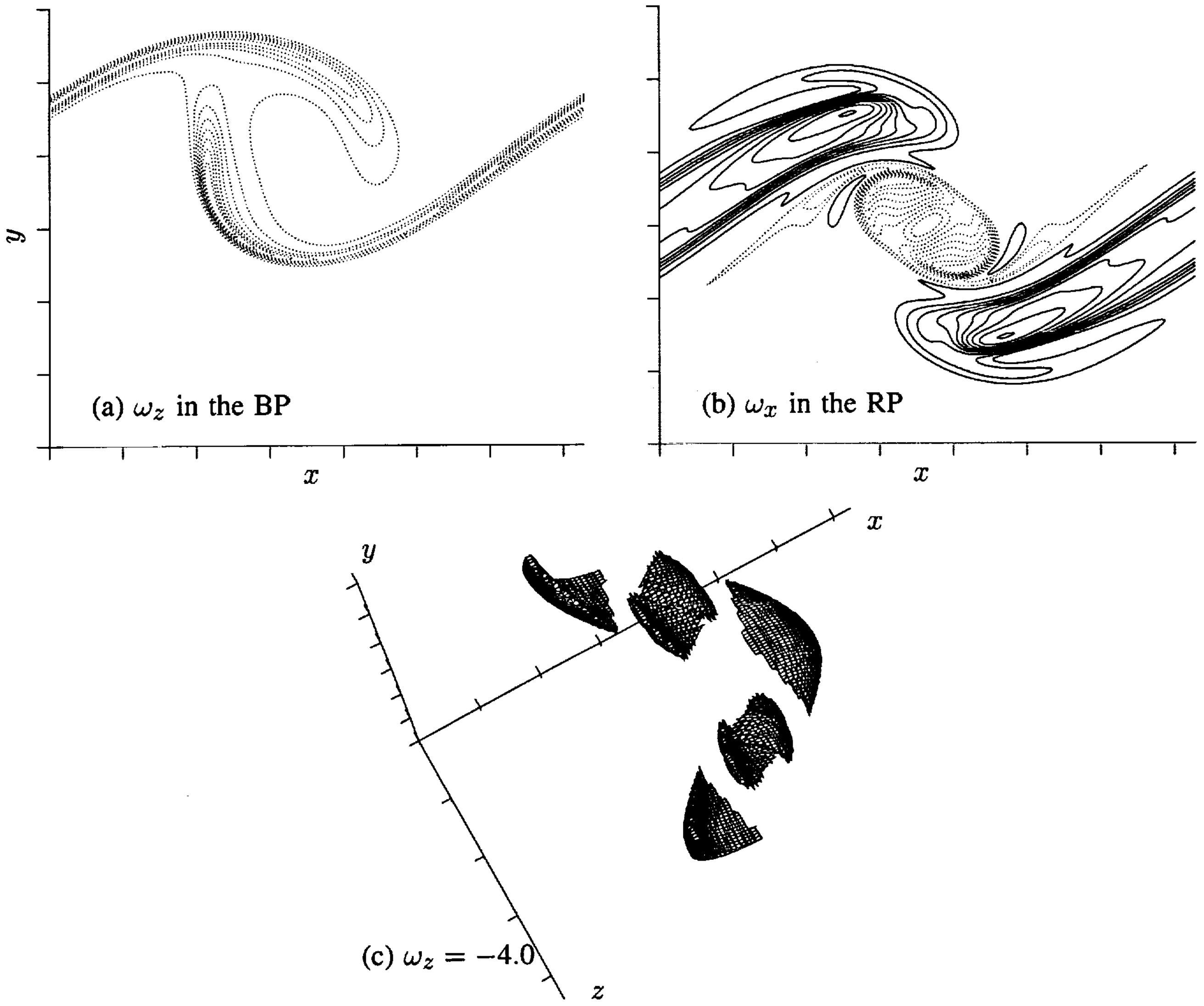

Figure 20. Contour plots for HIROLL at $t = \tau_r = 7.5$. Contour increments are (a) -0.7, and (b) ± 0.6. MP contours of ω_x and ω_z are shown in figure 21. Solid contours indicate positive vorticity, dotted contours indicate negative vorticity, and tic marks are at δ_ω^0 intervals.

the opposite-sign ω_x around the outer edge of the ribs again indicates that the vortex-line structure of HIROLL is more complex than that of ROLLUP.

The evolution of rib vorticity in HIROLL is shown in figure 21. As in figure 12(b), the passive scalar $T = 0.5$ contour level is superimposed upon the ω_z contours. Before τ_o, there is a good correlation between the regions of positive ω_z and regions where the initially horizontal scalar contour line has been "turned over." As shown in figure 21(b), many windings of the scalar interface occur before the molecular diffusivity of the passive scalar acts to mix the rib material (fig. 21(c)). Since $Pr = 1.0$, it is expected that viscosity would also begin to have an effect on the rib vorticity at this time. The ω_x pattern shown in figure 21(f) is indeed undergoing a change, acquiring a central core region of opposite sign, but this must be due at least in part to vortex stretching. At later times this trend continues, and by $t = 15$, the rib streamwise vorticity is concentrated in a narrow hoop-shaped region. The ribs also

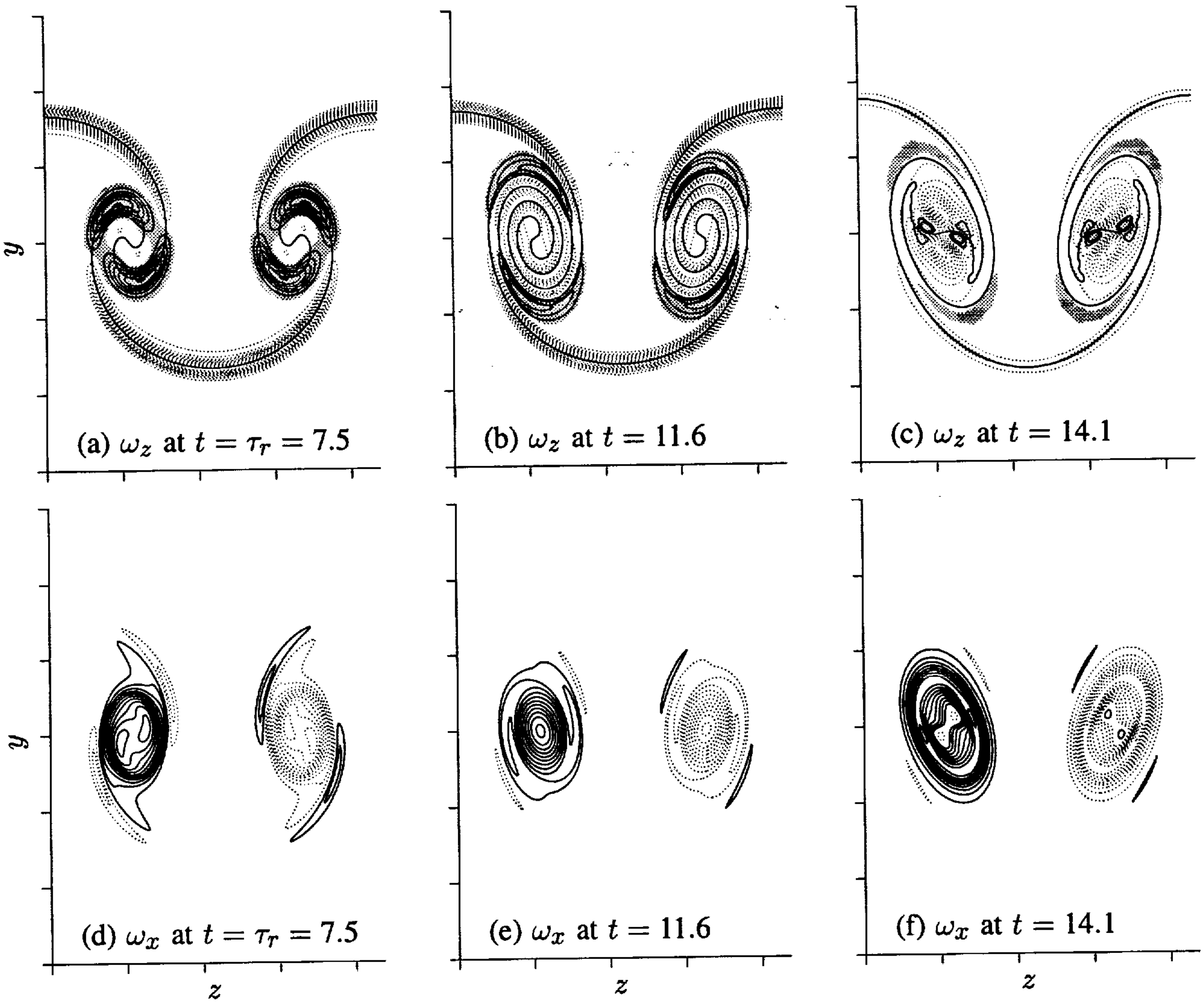

Figure 21. Contour plots of spanwise and streamwise vorticity in the MP. Contour increments are (a) ±0.4, (b) ±0.2, (c) ±0.3, (d) ±0.4, (e) ±0.7, and (f) ±0.5. In (a)–(c), the $T = 0.5$ contour (heavy solid line) has been superimposed on the spanwise vorticity contours. Shaded regions indicate regions of positive ω_z, solid contours indicate positive vorticity, dotted contours indicate negative vorticity, and tic marks are at δ_ω^0 intervals.

contain many regions of spanwise vorticity of both signs at this point. In summary, the HIROLL ribs are large enough to have their own complicated internal vortex dynamics, and this results in a flow that is more complex than the ROLLUP flow.

The vorticity distribution in both the BP and the RP at $t = 14.9 > \tau_o$ is shown in figure 22. In the BP, the vorticity (only ω_z because of flow symmetry) is confined to long filament-like regions[16] and roughly circular "roll-ups" of these filaments. Note also the presence of positive ω_z, which can only appear in the BP through viscous diffusion owing to flow symmetries. The contours of vorticity in the RP are complicated, with several regions that have both signs of all components present. At this

---

[16] These filament-like regions are actually vortex sheets, for there is little spanwise variation over several of their thicknesses.

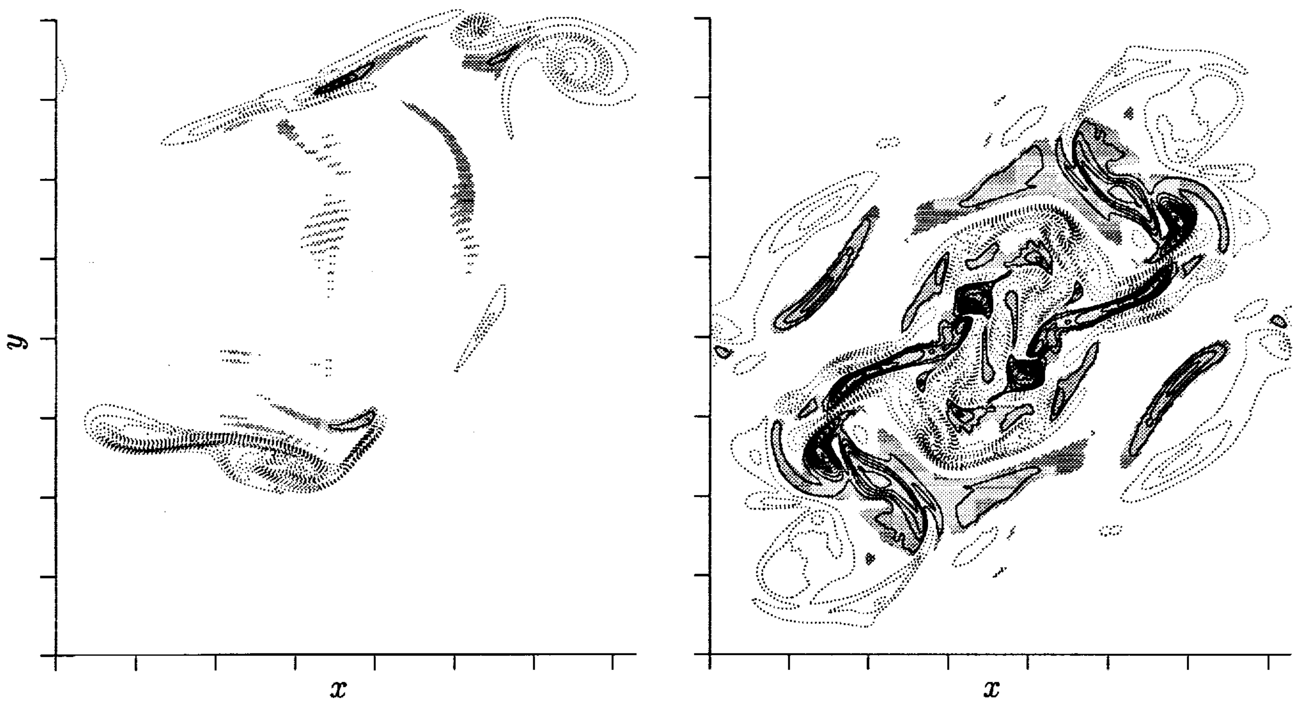

(a) ω_z in the BP

(b) ω_z in the RP

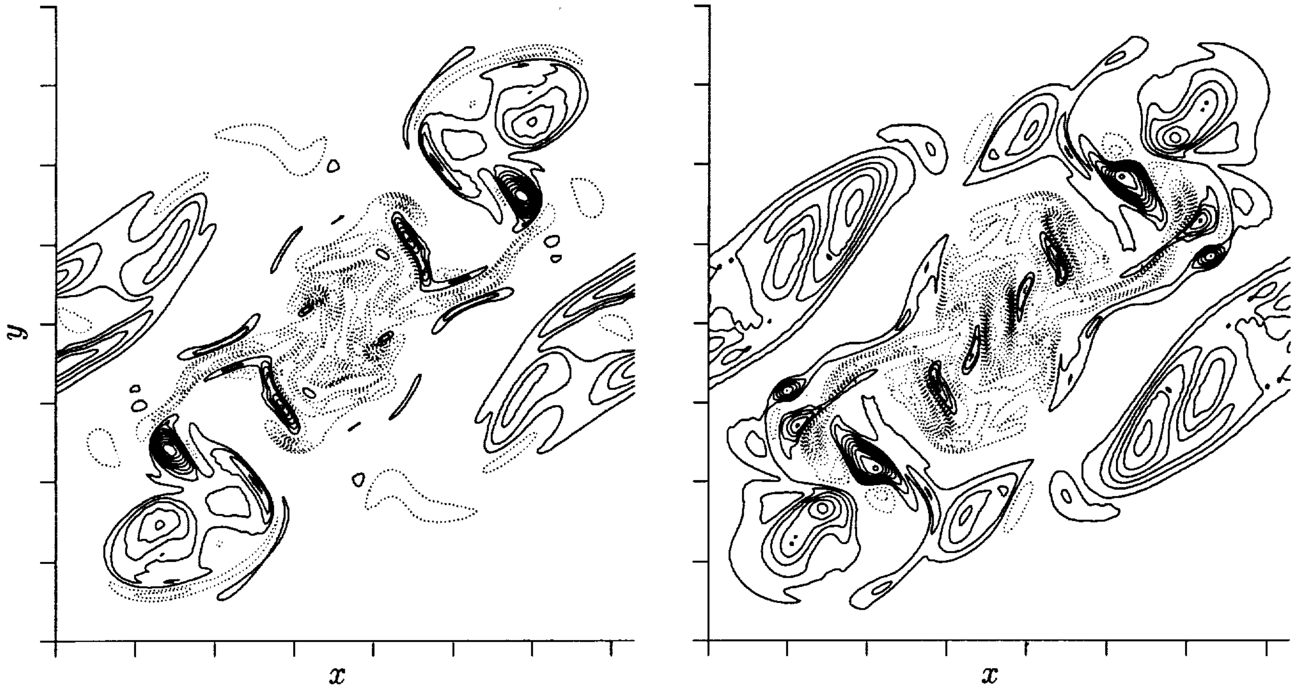

(c) ω_x in the RP

(d) ω_y in the RP

Figure 22. Contour plots of all vorticity components in the BP and the RP of HIROLL at $t = 14.9$ (ω_x and ω_y are zero in the BP). Contour increment is ± 1.0. Shaded regions indicate regions of positive ω_z, solid contours indicate positive vorticity, dotted contours indicate negative vorticity, and tic marks are at δ_ω^0 intervals.

spanwise location the layer appears "turbulent," although the symmetries are preserved. In Part 2 it will be seen that flow features like those in figure 22 are indeed associated with the transition to turbulence.

The development of A_{ij} for three low-wavenumber modes in LOROLL, ROLLUP, and HIROLL is shown in figure 23. The initial three-dimensional disturbance energy in HIROLL is larger than that of the two-dimensional fundamental, as can be seen by comparing the initial levels in figures 23(a) and 23(b). It is large enough to significantly reduce both A_{10}^{sat} and τ_r. On the other hand, the evolution of A_{10} for LOROLL is indistinguishable from that of the corresponding two-dimensional case (2D500), as shown in figure 23(a). Remarkably, the curves describing the time development of A_{01} and A_{11} (figs. 23(b), 23(c)) are nearly parallel for all the cases (at least up to τ_r). Apparently the three-dimensional modes are interacting linearly with the mean flow and with the two-dimensional modes up to this point, the constant ratio between the curves being determined by their initial ratio. For all cases, A_{11} becomes greater than A_{01} at $t \approx 8$.

The mid-braid spanwise vorticity, mid-braid strain-rate, and momentum thickness are shown in figure 24. The behavior of these quantities in LOROLL is intermediate between the results described for ROLLUP and the corresponding two-dimensional flow, with δ_m being virtually identical to the growth in the two-dimensional flow until τ_o. The behavior of these quantities in HIROLL shows qualitative differences. The momentum thickness grows rapidly from $t = 0$ and becomes larger than that of ROLLUP. This is due in part to the wide extent of vorticity in the braid region (which makes the average-layer thickness greater), but mainly to the fact that the stronger ribs push much of the

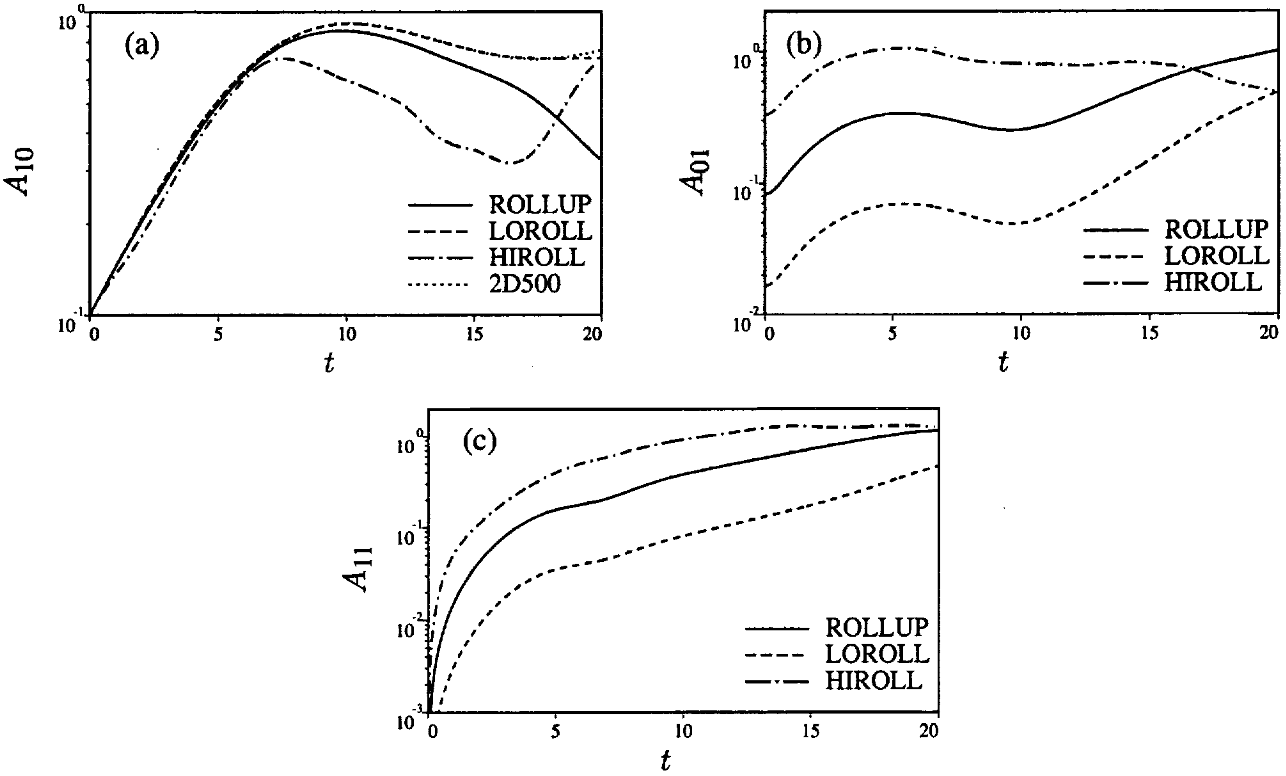

Figure 23. Time development of (a) A_{10}, (b) A_{01}, and (c) A_{11} for ROLLUP, LOROLL, HIROLL, and the corresponding two-dimensional flow (2D500).

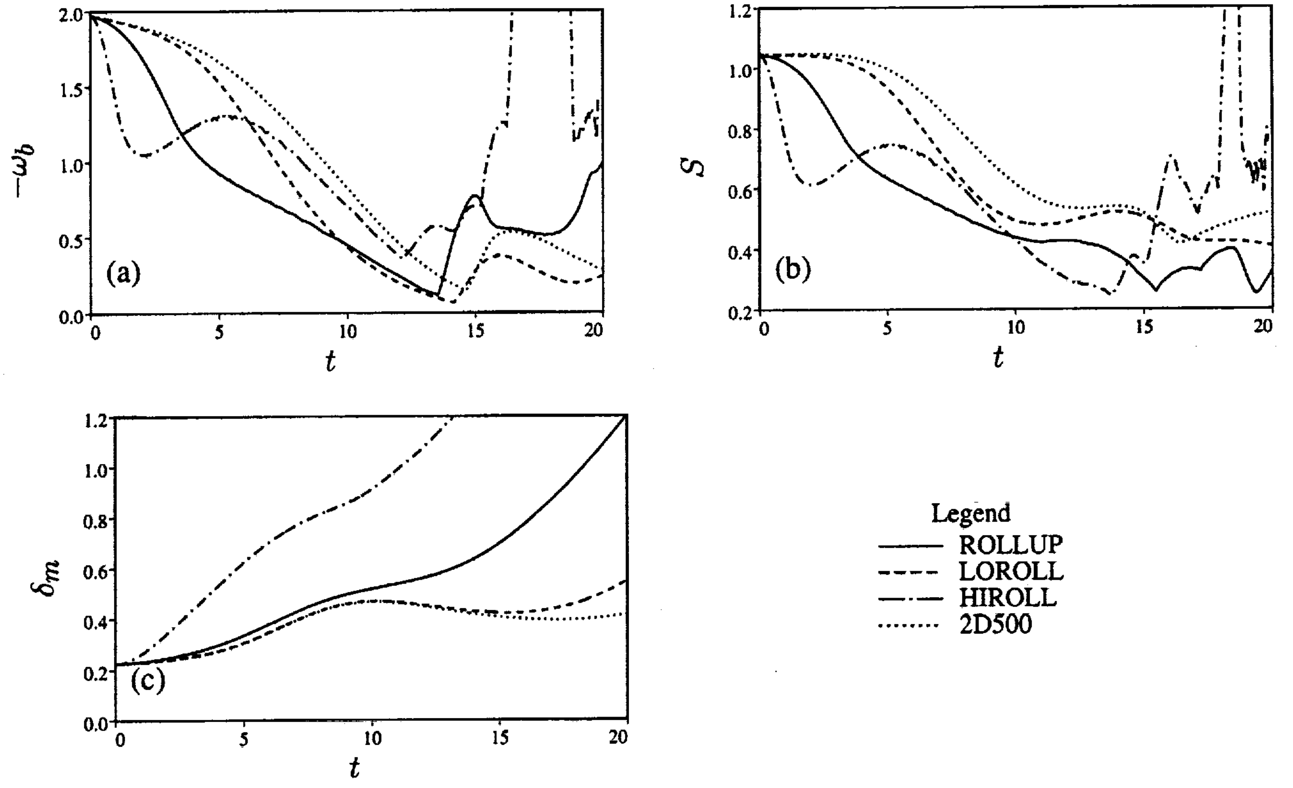

Figure 24. Time development of (a) mid-braid spanwise vorticity, (b) mid-braid strain-rate, and (c) momentum thickness for ROLLUP, LOROLL, HIROLL, and the corresponding two-dimensional simulation (2D500).

layer farther from the centerline (note the BP ω_z shown in fig. 20(a) is almost entirely above the centerline). The mid-braid spanwise vorticity magnitude initially decreases more rapidly (because of faster corrugation of the layer), but then increases, reaching a local maximum as vortex stretching temporarily outpaces removal from the braid region. After τ_r, ω_b behaves erratically, as might be expected from the complicated structure shown in figure 22. From the definition given in section 3.2 (time at minimum $|\omega_b|$), $\tau_o = 12.1$ for HIROLL (fig. 24(a)). However, in this case the internal rib-vortex dynamics, not the reentry of spanwise vorticity into the braid region far from the centerline, are responsible for the increase in ω_b magnitude at $t = 12.1$. The time $\tau_{reentry}$ is about 14.5 in this flow, in closer agreement with τ_o from LOROLL and ROLLUP. The mid-braid strain-rate (fig. 24(b)) shows a local maximum at $t \approx 5$, which is related to the increase in mid-braid vorticity at this time. By τ_o, the same plateau level attained in the ROLLUP simulation is reached. For late times, the strain-rate is large and erratic, like ω_b.

The vorticity extrema for the three cases are shown in figure 25 (the minima of ω_x and ω_y are equal and opposite to the maxima because of flow symmetry). The strong vortex stretching in HIROLL has generated peak spanwise vorticity levels that are more than 10 times the initial peak level (this flow requires a finer computational mesh because of this). Also, the positive ω_z level increases sooner than in ROLLUP. LOROLL, on the other hand, does not develop any significant positive ω_z until $t > \tau_o$. In addition, vortex stretching has only increased the peak negative ω_z by 30% at $t = \tau_o$ (reflected in the

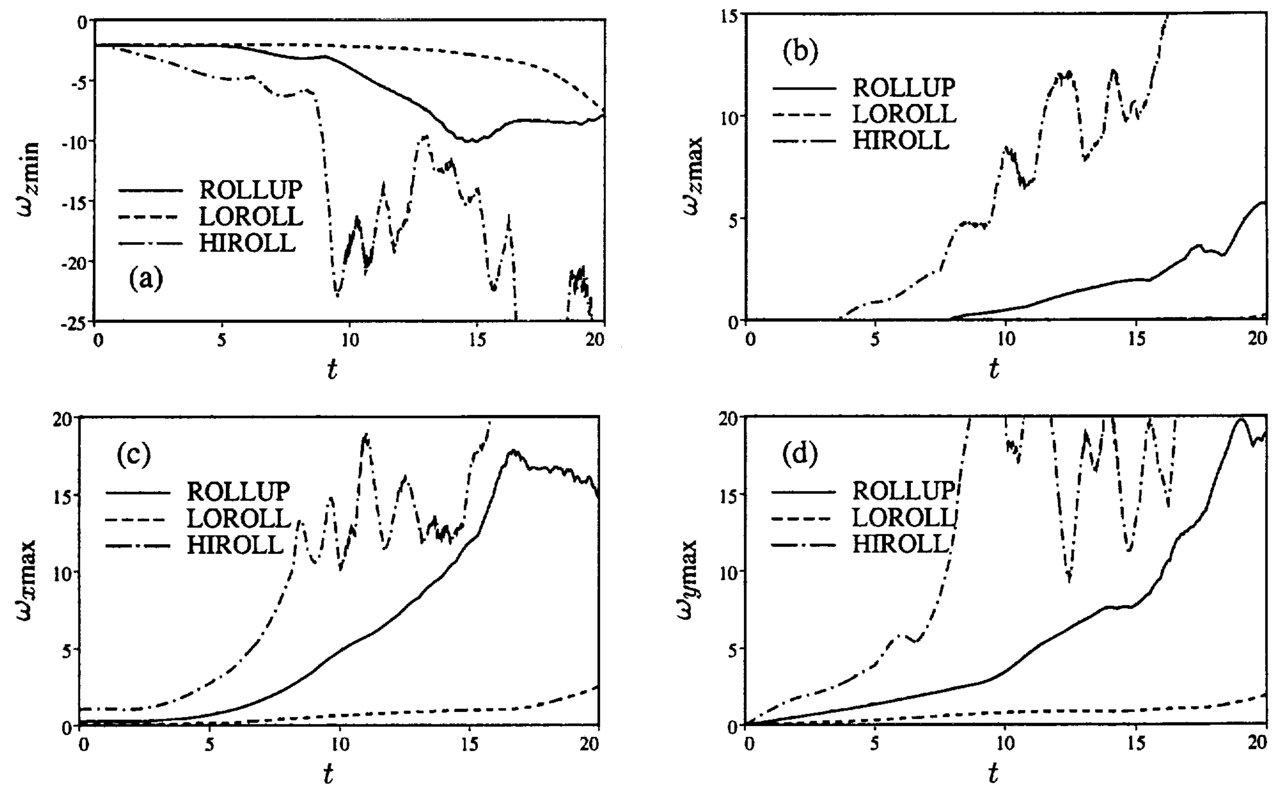

Figure 25. Time development of vorticity component extrema for ROLLUP, LOROLL, and HIROLL. Note that $\omega_{x\min}$ and $\omega_{y\min}$ are equal in magnitude but opposite in sign to $\omega_{x\max}$ and $\omega_{y\max}$.

weak cup vorticity of fig. 19(a)). Although the extrema of ω_x and ω_y reach similar levels for HIROLL and ROLLUP, they remain less than 1.0 until after τ_o for LOROLL.

Up to about τ_o, the mid-braid streamwise circulation Γ_x^{MP} (fig. 26) differs among the cases by a roughly constant factor (which, as with A_{ij}, is set by the initial condition).[17] In all cases, there is a sudden increase in Γ_x^{MP} when the spanwise vorticity (wisp 1) reenters the MP (at τ_o, except for in HIROLL, where $\tau_{reentry} \approx 14.5$). The circulation evolution after τ_o shows a qualitatively similar increase for the LOROLL and ROLLUP simulations. For HIROLL, however, the circulation oscillates, does not reach 3 times its plateau value (sec. 4.2.3), and by $t = 20$ is actually less than the plateau level.[18]

The slow, roughly linear growth of the LOROLL ω_x and ω_y extrema is qualitatively different from that of the other cases. As noted above, this is because the MP ω_x (fig. 19(c)) does not collapse into a compact vortex. The Lin and Corcos (1984) model described in section 4.2 predicts the kind of pattern shown in figure 19(c) for low values of Γ_{rib}. From their model problem, two important parameters are

---

[17] Note that this is also true of the circulation-based collapse parameter $\mathcal{L}$ described below.

[18] Note that this plateau level is about 4 and is already almost 30% of Γ_z. A factor-of-three increase would require virtually all of the vortex filaments to cross the MP.

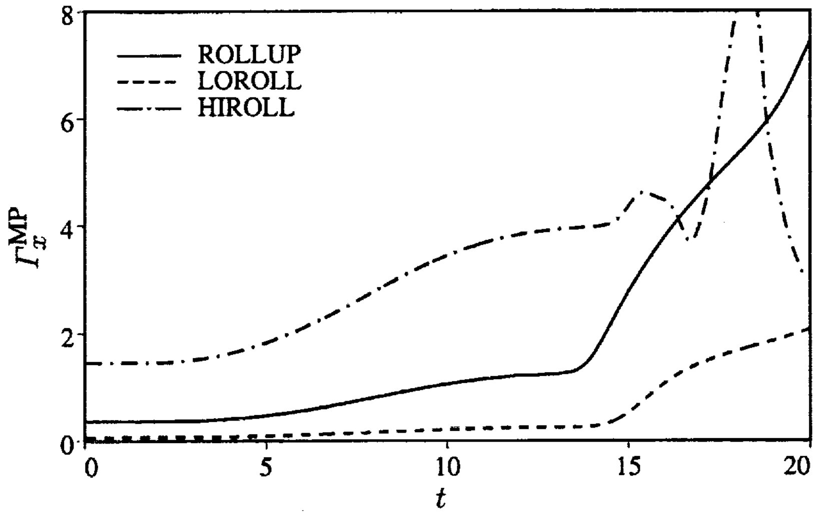

Figure 26. Time development of streamwise circulation in the MP (Γ_x^{MP}) for ROLLUP, LOROLL, and HIROLL.

derived. These are the nondimensional circulation strength,

$$\Gamma^* = \frac{\Gamma_{rib}}{S\lambda_z^2} \tag{16}$$

(S being the mid-braid principal strain-rate) and the aspect ratio,

$$A_R = \frac{\lambda_z}{4\delta_a} \tag{17}$$

($\delta_a = \sqrt{\pi\nu/(2S)}$, a strain-diffusion equilibrium length scale). For $\Gamma^* \ll 1$ and $A_R \gg 1$, they expect "substantial collapse" for $\Gamma^* A_R > 0.43$. For more typical values of Γ^* and A_R this simple criterion must be generalized. Their curve (shown in their fig. 9) for substantial collapse is well described by

$$\Gamma^* A_R^{1.365} = 1.45 \tag{18}$$

By substituting the definitions given above, this yields

$$\mathcal{L} = \frac{\Gamma_{rib}}{S^{0.3175}\lambda_z^{0.6350}\nu^{0.6825}} > 13.1 \tag{19}$$

It should be noted that increasing the rib circulation and the Reynolds number improves the chance of collapse, whereas increasing the two-dimensional strain-rate and the spanwise wavelength reduces the chance of collapse. Of these effects, the circulation is of primary importance; the Reynolds number and spanwise wavelength are somewhat less significant, and changes in the two-dimensional strain-rate have only a minor effect on $\mathcal{L}$. In the two-dimensional Lin and Corcos model problem, all of the quantities entering the definition of $\mathcal{L}$ are constant during their flow evolution. In the three-dimensional mixing layer, Γ_{rib} and S vary as the flow evolves. The value of Γ_{rib} typically increases because of the conversion (turning) of ω_z into ω_x by the vortex-stretching term (with a particularly large increase after τ_o), and S decreases as ω_z (which contributes to S) is removed from the braid region.

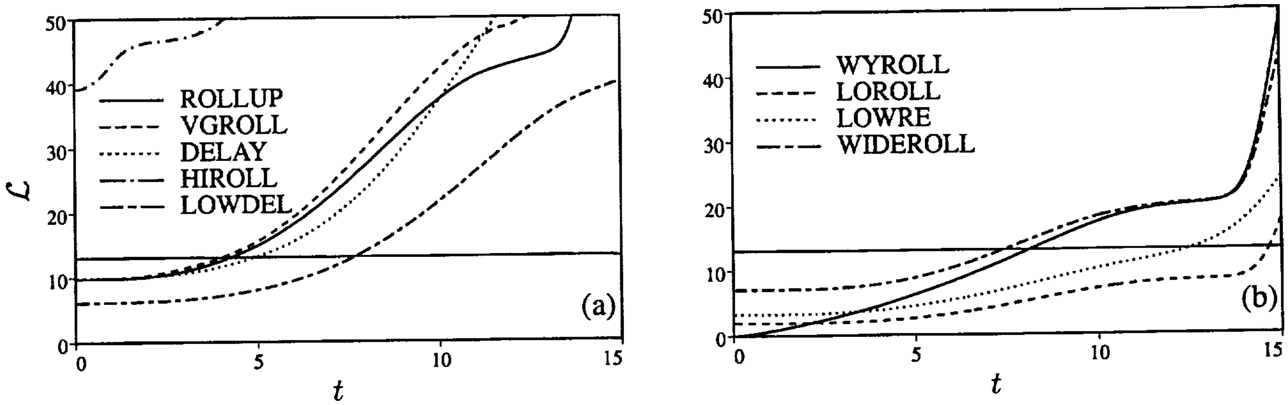

Figure 27. Time development of the Lin and Corcos collapse parameter $\mathcal{L}$ for (a) cases that exhibit collapse, and (b) cases that exhibit marginal (WYROLL) or no collapse. The horizontal lines at $\mathcal{L} = 13.1$ represent the Lin and Corcos collapse criterion.

The time evolution of $\mathcal{L}$ for all the STI disturbance simulations listed in table 2 is shown in figure 27. Here, the streamwise circulation Γ_x^{MP} is used in place of Γ_{rib}. Because the ribs have a nonzero extent in y, this substitution is not exact (in the limit of zero vertical rib extent $\Gamma_{rib} = \Gamma_x^{\mathrm{MP}}$, because $\mathrm{d}\Gamma_{rib} = \omega_{rib}\,\mathrm{d}A_{rib} = \omega_x\,\mathrm{d}A_x$). However for the cases considered here, this error is small because the "ribwise" variation of ω_x over distances comparable to the rib thickness is small. By examining the MP vorticity and passive scalar contour patterns, it was determined that the cases shown in figure 27(a) do exhibit substantial collapse (see also τ_c given in table 2). The cases shown in figure 27(b) either undergo partial collapse (WYROLL) or show no evidence of collapse (at least before τ_o). All the flows that exhibit clear collapse have $\mathcal{L} > 13.1$ well before the roll-up is completed. Those exhibiting partial collapse achieve this critical level after $t \approx 8$, by which time the roll-up is nearly complete. The LOWRE and LOROLL simulations, in which the ribs do not collapse, do not have $\mathcal{L} > 13.1$ until $t > \tau_o$. Despite the fact that the evolution of $\mathcal{L}$ in the WIDEROLL simulation is similar to that in the WYROLL simulation, the ribs in the WIDEROLL flow do not show even the marginal collapse observed in WYROLL until well after τ_o. Lin and Corcos found that the time required to achieve collapse increases rapidly as Γ^* decreases. Thus, the larger λ_z in WIDEROLL results in a smaller Γ^* and a larger time until collapse, in agreement with the current results. In general, examination of figure 27 indicates that the Lin and Corcos criterion is accurate in determining whether the ribs collapse, and indicates that their two-dimensional model problem does indeed capture the essence of the mid-braid flow evolution.

Figure 28 contains MP views of a passive scalar quantity taken from the LOROLL (noncollapsed) and ROLLUP (collapsed) simulations at $t \approx \tau_o$. Again, the patterns are virtually identical to those predicted by Lin and Corcos (see their figs. 12, 13). Although the streamwise vorticity associated with the noncollapsed case is too weak to induce more than a mild bending of the scalar contours, that of the collapsed case has generated mushroomlike patterns by wrapping the scalar around the ribs. Flow visualization in experimental mixing layers has indicated the presence of similar mushroom-shaped patterns, which suggests that to produce such collapsed ribs, experimental disturbance levels must be of the same order as in ROLLUP, or larger.

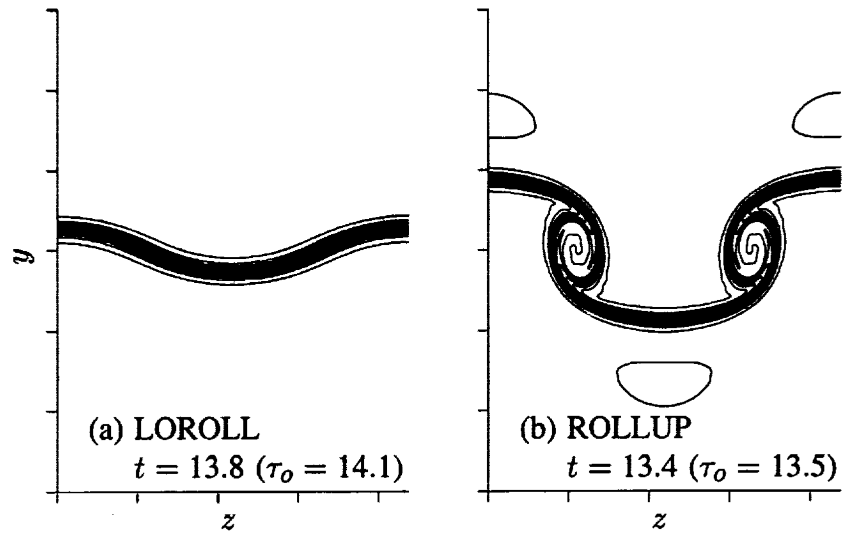

Figure 28. Contour plots of the passive scalar (T) in the MP with contour increment 0.08 from 0.02 (bottom) to 0.98 (top). Tic marks are at δ_ω^0 intervals.

4.3.2 Initial Reynolds number– Reduction of the initial Reynolds number from 500 to 100 leads to changes similar to those observed for the two-dimensional cases described in section 3.2. The momentum thickness initially increases more rapidly, a result of viscous diffusion, but later the layer thickness is less than that of the $Re_0 = 500$ case. The mid-braid strain-rate decreases more rapidly initially, but reaches about the same asymptotic level. The decrease of $-\omega_b$ is enhanced at early times, but the value at τ_o is larger in magnitude. This and the fact that $-\omega_b$ does not undergo a sudden increase at τ_o (but rather has a smooth, rounded minimum) are similar to the behavior of the two-dimensional case shown in figure 4(a). The energies A_{10}, A_{01}, and A_{11} all grow at slower rates and saturate at lower values for the $Re_0 = 100$ case. Again, similar behavior is observed (for A_{10}) in the two-dimensional simulations.

Reducing Re_0 also reduces the effects of vortex stretching and the associated three-dimensionality. The evolution of the vorticity extrema for the LOWRE simulation (identical to ROLLUP in all respects except for Re_0) is compared with that of the ROLLUP simulation in figure 29. The peak negative ω_z is reduced owing to the enhanced viscous diffusion. The appearance of positive ω_z is also delayed and its growth rate is smaller. Similarly, the ω_x and ω_y extrema are reduced. In general, the behavior of the low-Reynolds-number simulation is similar (in terms of the extent of three-dimensionality) to the LOROLL simulation begun from weaker initial three-dimensional disturbances.

The growth of Γ_x^{MP} in LOWRE is reduced for $t > \tau_o$ (fig. 30(a)). The reduced ability to remove ω_z from the mid-braid region and the lack of a sudden reentry of ω_z into the mid-braid region have made the growth at $t = \tau_o$ more gradual in the LOWRE case.

As in the two-dimensional layers, the larger viscosity in the LOWRE simulation tends to fatten the vortical structures present in the flow. The roller is fattened, and this results in a short braid region. The viscous-strain equilibrium length scale is greater than that of the ROLLUP simulation, and this prevents the cups from becoming as thin as they do for that case. The rib vortices remain broad and are only marginally collapsed by τ_o. This Reynolds number dependence is in agreement with the Lin and Corcos

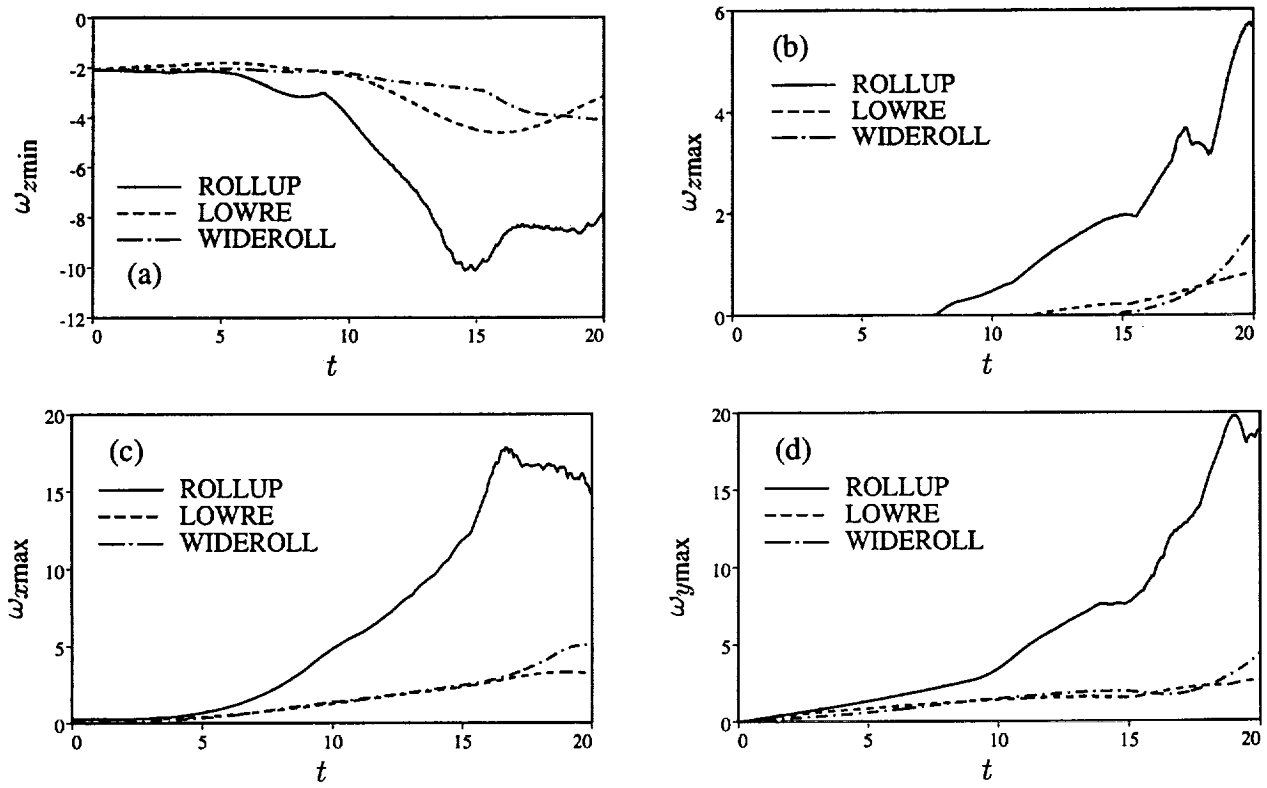

Figure 29. Time development of vorticity component extrema for ROLLUP, LOWRE, and WIDEROLL. Note that $\omega_{x\min}$ and $\omega_{y\min}$ are equal in magnitude but opposite in sign to $\omega_{x\max}$ and $\omega_{y\max}$.

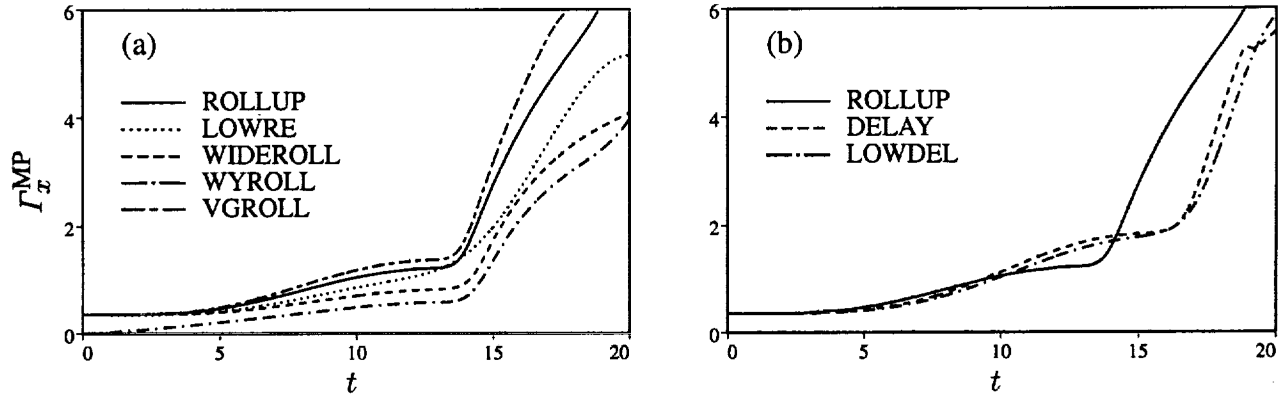

Figure 30. Time development of the streamwise circulation (Γ_x^{MP}).

model, as evidenced by the LOWRE curve in figure 27(b). Even when collapse does occur (stronger initial three-dimensional disturbances, longer flow-development times), the resulting mushroom patterns (as visualized by a passive scalar) are fat and not well separated in the spanwise direction.

4.3.3 Spanwise wavelength– The WIDEROLL simulation is identical to ROLLUP except for the spanwise disturbance wavelength, λ_z. Instead of the "most unstable" spanwise wavelength of about $0.6\lambda_x$, λ_z was made equal to λ_x. The initial circulation of the three-dimensional disturbance is the same as in ROLLUP, but the circulation growth is less (fig. 30(a)). This is consistent with the lower growth rate of disturbances with this wavelength.

In general, the WIDEROLL mixing layer is intermediate between the ROLLUP layer and the corresponding two-dimensional flow; in other words, widening the spanwise domain is roughly equivalent to reducing the initial three-dimensional disturbance amplitude. In WIDEROLL, the layer thickness does not grow as rapidly as in ROLLUP, but it does grow faster than the corresponding two-dimensional layer. The appearance of positive ω_z is delayed (until $t > \tau_o$), and the peak negative vorticity is only 1.3 times its initial peak level by $t = \tau_o$ (fig. 29). At τ_o the levels of ω_x and ω_y in ROLLUP are roughly 4 times those of WIDEROLL. The similarity of the extrema for the LOWRE and WIDEROLL cases indicates that a similar reduction in three-dimensionality can be achieved by reducing either Re_0 or increasing λ_z.

Figure 27(b) shows the development of $\mathcal{L}$ for the WIDEROLL simulation. From the Lin and Corcos (1984) model one would expect "partial or doubtful collapse" because $\mathcal{L}$ does not reach the critical value of 13.1 until the roll-up is nearly complete. Examination of the MP indicates that this is indeed the case. It appears that the extent of three-dimensionality achieved by variation of Γ_x^0 (sec. 4.3.1), ν (sec. 4.3.2), and λ_z (sec. 4.3.3) is well predicted by the Lin and Corcos model.

4.3.4 Two-dimensional disturbance amplitude– In the simulations described above, the circulation Γ_x^{MP} at $t = \tau_o$ is larger than Γ_x^0 by a factor ranging from 2.4 to 3.8. This increase is accomplished by the action of vortex stretching, which turns some of the ω_z in the braid region into ω_x. This process eventually stops when the spanwise vorticity is depleted from the braid region (leaving a roughly constant value of Γ_x^{MP} for $\tau_r < t < \tau_o$). By decreasing the amplitude of the two-dimensional fundamental disturbance, the roll-up and the associated removal of braid ω_z are delayed. It might be expected that the value of Γ_x^{MP} could reach higher levels under these circumstances.

To test this hypothesis, and to examine other effects of a delayed roll-up, a simulation (DELAY) identical in all respects to ROLLUP except for the initial value of A_{10}, was run. The amplitude A_{10} was reduced to 40% of its value in ROLLUP. Although the growth rate of A_{10} is initially (and for several time units) the same in the two simulations, the lower value at $t = 0$ in the DELAY simulation causes the flow to take about 2.5 time units longer to reach the same value of A_{10}. However, A_{10}^{sat} is lower in DELAY than in ROLLUP, and for $t > \tau_r$ the evolution of A_{10} is similar in the two simulations.

The values of τ_r and τ_o in the DELAY flow are also about 2.5 units larger than their values in the ROLLUP flow (table 2). The circulation development of the two simulations is compared in figure 30(b). As expected, the sudden increase in Γ_x^{MP} that happens at τ_o occurs about 2.5 time units later in the DELAY flow. It is also clear, however, that the value of Γ_x^{MP} (roughly constant for $\tau_r < t < \tau_o$) is higher than that in the ROLLUP flow despite the fact that Γ_x^0 is the same in both flows. The ratio

$\Gamma_x^{\mathrm{MP}}(t = \tau_o)/\Gamma_x^0$ is 5.2 in the DELAY flow, well above the range of values given above for this parameter in the other simulations and 50% larger than the corresponding value in the ROLLUP flow. Similar behavior is observed in the Lin and Corcos (1984) collapse parameter (fig. 27(a)); the growth is delayed, but by $t \approx 10$, $\mathcal{L}$ becomes larger in DELAY than in ROLLUP. It is indeed the case that delaying the removal of spanwise vorticity from the braid region has increased the circulation of the rib vortices.

The growth of $\omega_{x\max}$ and $\omega_{y\max}$ in the DELAY flow also lags that of the ROLLUP flow. However, for these quantities the lag time is only about a single time unit. Thus, at the same time relative to τ_r (or τ_o), these extrema are larger in the DELAY flow than in ROLLUP.

The behavior of the ω_z extrema cannot be predicted by a simple time lag. The initial appearance of positive ω_z in DELAY does indeed occur about one time unit later than in ROLLUP, but in the developed DELAY flow, $\omega_{z\max}$ is up to twice the ROLLUP value (and is even larger if the flows are compared at the same time relative to their respective τ_r values). The magnitude of $\omega_{z\min}$ is generally smaller in the DELAY flow. It is more informative, however, to compare the evolution of $\omega_{z\min}$ at the same time relative to the τ_r value in each flow (i.e., shift the DELAY curve 2.3 time units to the left). When plotted in this way, $\omega_{z\min}$ is greater in magnitude in the DELAY flow only up until a time about four fifths of the way from τ_r to τ_o. Before this, all DELAY vorticity extrema are larger (indicating higher three-dimensionality), as would be expected from the larger rib circulation. After this, however, the cup vorticity in DELAY is not as strong as that in ROLLUP even though the rib circulation remains larger, apparently because the rib vortices do not remain confined to the RP for as long as they do in ROLLUP. They become horseshoe-shaped (resulting in the larger peak positive ω_z noted above) and do not continue straining the same cup vorticity for as long as they do in ROLLUP.

4.3.5 Form of the STI disturbance– Other vertical profiles can be used for the $(0, 1)$ mode disturbance instead of the ωG disturbance profile used in ROLLUP. In this section a comparison is made with a run (VGROLL) identical in all respects to ROLLUP except that the same initial value of Γ_x is obtained from an appropriately scaled vG disturbance. The vG disturbance contains ω_x of both signs, with a peak in ω_x at the centerline, which is higher than in the ωG case, and two opposite-sign ω_x zones above and below this central region. A comparison of VGROLL and ROLLUP indicates that the flow evolution is not sensitive to the form of the initial disturbance. The VGROLL layer exhibits slightly more three-dimensionality (as measured by the indicators described in the above subsections), perhaps because the initial ω_x extrema are slightly larger (as are the initial three-dimensional disturbance energies). The circulation (fig. 30(a)), although initially the same as that in ROLLUP, is about 10% larger at τ_o ($\tau_o = 13.5$ for both flows).

A subtle difference in the details of the three-dimensionality occurs in the VGROLL simulation. Positive ω_z occurs sooner and remains larger than in the ROLLUP simulation. Despite this apparently enhanced three-dimensionality, the peak negative ω_z is not as large at late times ($t > \tau_o$). This behavior is similar to that described in section 4.3.4 for the DELAY simulation (which also has stronger ribs than ROLLUP) and is associated with the more rapid deformation of the developed rib vortices.

4.3.6 The presence of initial ω_y– In the simulations described so far, the ω_y vorticity component was not initialized, but rather developed rapidly from the initial ω_x disturbance. The simulation described here (WYROLL) was begun from an ωG disturbance in ω_y with the same peak amplitude as the ωG disturbance of the ROLLUP simulation (0.2618). The streamwise vorticity, ω_x, was initially zero throughout the domain (implying $\Gamma_x^0 = 0$). To maintain a solenoidal vorticity field, the spanwise vorticity distribution had to be adjusted (by an amount $\partial\omega_y/\partial y$). Because the ω_y was placed in the $(0, 1)$ STI mode, this adjustment created $\partial\omega_z/\partial z$, and the spanwise vorticity distribution was no longer initially two-dimensional.

The WYROLL simulation exhibits less three-dimensionality than the ROLLUP case. The layer spreads at a reduced rate, the mid-braid strain-rate S decreases more slowly, ω_z is removed at a slower rate from the mid-braid region, positive ω_z forms later, and vortex stretching produces only about half the peak ω_x, ω_y, and ω_z levels. The circulation Γ_x^{MP}, although initially zero, grows to about half the value reached in the ROLLUP simulation by τ_o (fig. 30(a)). The Fourier mode energies A_{10}, A_{01}, and A_{11} lie between those of the ROLLUP and LOROLL simulations shown in figure 23 for most of their evolution (the exception being A_{01} during an adjustment period up to $t \approx 7$). In general, it appears that an initial ω_y disturbance is about half as effective at generating three-dimensionality as an initial ω_x disturbance of the same amplitude.

4.3.7 Wake component– Experimental spatially developing mixing layers typically form between streams initially separated by a splitter-plate. The mean velocity profile just downstream of this splitter-plate has a wake component resulting from the boundary layers on each side of the splitter-plate. To compare our results with those of experiments it is necessary to know how the disturbance develops in the presence of such a modified mean profile. Numerical simulations using initial mean profiles that include a wake component show qualitatively the same behavior as those described above, if the wake momentum deficit is small. For strong wake components, the layer development appears to be a hybrid between the mixing-layer structure described above and that observed in plane wakes.

When a mean profile was used that was similar to that used by Sandham and Reynolds (1987), the wake washed out of the mean profile before τ_r. Because the initial mean-velocity profile is asymmetric, the point-reflection symmetry, equation (11), is broken. The RP vorticity contours are no longer symmetric around the roller center. In addition, the ribs are no longer equally spaced in the spanwise direction, but rather appear in negative/positive pairs as one moves in the positive spanwise direction, with the distance between pairs greater than that between the ribs of a pair. This has also been observed by Ashurst and Meiburg (1988), who used a vortex tracking simulation, and found experimentally by Bernal (1981) and Bernal and Roshko (1986) (flow visualizations indicate spacing between "mushrooms" is greater than mushroom width).

The presence of large gradients (owing to the splitter-plate boundary layers) results in strong initial spanwise vorticity of both signs. To some extent, the weaker positive vorticity is simply passively advected by the developing flow. Also, the rib vortex lines can undergo a viscous reconnection to form closed vortex loops in this flow.

Although the details of the layer evolution can be different when a wake component is included, the vortex dynamics described in the previous sections still dominate the layer development. The two-dimensional roll-up progresses, removing vorticity from the braid region. Rib vortices strengthen, collapse, and create strong cup structures. In the absence of subharmonics, oversaturation occurs as described above. For large initial momentum deficits, the layer acquires some wakelike characteristics, but for momentum deficits likely to be encountered in experiments (i.e., two boundary-layer velocity profiles), the presence of a mean-wake component is not expected to significantly change the layer development.

4.4 Oblique Initial Disturbances

In this section the effect of placing initial three-dimensional disturbance energy in the $(1, \pm 1)$ modes (instead of in the $(0, \pm 1)$ modes) is examined. Although it is possible to initialize the $(1, 1)$ and $(1, -1)$ modes separately, it is expected that in most experimental situations there would be no preference between this pair of oblique waves, and they are initialized with equal amounts of energy. Simulations begun from single oblique modes are discussed in section 4.4.4.

For the simulations considered here, the disturbance wavelengths and the initial Reynolds number are the same as for the ROLLUP simulation, that is, $\lambda_x = 1.16(2\pi)$, $\lambda_z = 0.6\lambda_x$, and $Re_0 = 500$. The three-dimensional disturbance energy is placed in the $(1, \pm 1)$ modes with a VE vertical profile (unlike the STI disturbances, oblique three-dimensional disturbances have well-defined eigenfunctions). Surfaces of constant ω_x resulting from such an initialization are shown in figure 31. Because $\partial\omega_x/\partial x$ is no longer zero, the initial spanwise vorticity field is no longer two-dimensional.

As mentioned in section 4.1, when considering a pair of oblique wave disturbances, the phase relative to the two-dimensional disturbance must be specified. Here we will consider the two extreme cases of relative phasing and a case halfway between them. The "in-phase" case (OBLIN) situates

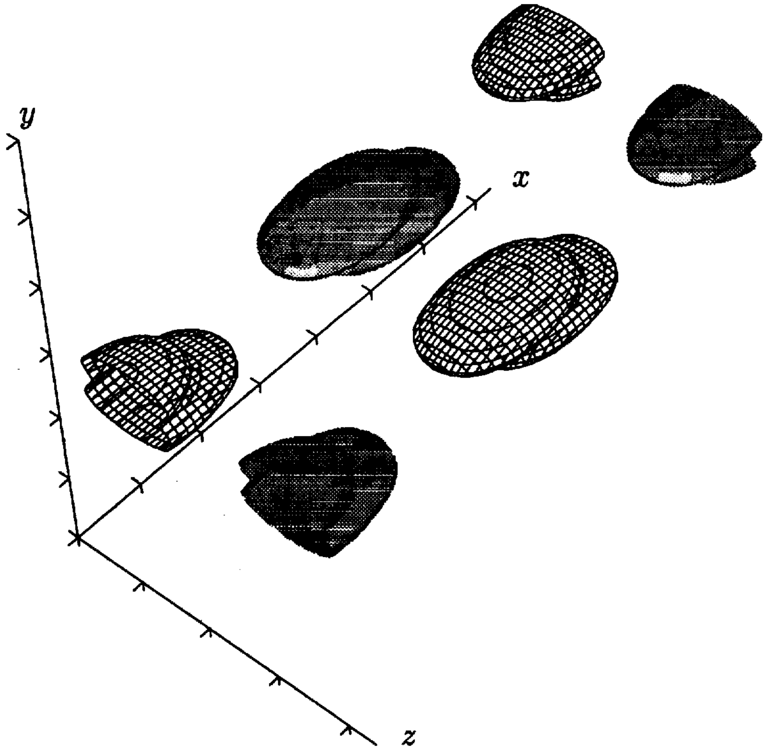

Figure 31. Surfaces of constant streamwise-vorticity magnitude of the oblique disturbance at $t = 0$. Cross-hatched surfaces represent $\omega_x = -0.15$, shaded surfaces represent $\omega_x = 0.15$, and tic marks are at δ_ω^0 intervals.

the two-dimensional disturbance such that the spanwise roller will form in the center of the domain depicted in figure 31. In this case, Γ_x is maximum both in the roller core and in the braid region. For the "out-of-phase" case (OBLOUT), the two-dimensional disturbance is placed such that the spanwise roller forms one quarter of the way through the domain shown in figure 31 (periodicity has been used to center the roller in the domain for figures shown later). The MP and CP initially have $\Gamma_x = 0$ in this case. The third case (OBLMID) is halfway between these two extremes (Γ_x^{MP} initially $\sqrt{2}/2$ of the value in OBLIN).

Although the eigenfunction for the linear stability problem has nonzero ω_y, ω_y was set to zero for the simulations described here to facilitate comparison with ROLLUP. The two extreme phasing cases (OBLIN and OBLOUT) were also run with nonzero ω_y in the initial conditions (as given by the eigenfunction). The larger initial three-dimensional disturbance energy in these cases leads to more three-dimensionality, but the flow evolution is qualitatively similar to OBLIN and OBLOUT. For these cases A_{11} is initially greater than A_{10}. However, as with the simulation begun from an ω_y disturbance (discussed in section 4.3.6), A_{11} decays initially and grows only after A_{01} reaches a significant amplitude. By τ_o, the Fourier mode energies of the simulations with and without ω_y are similar, although A_{10} in the ω_y simulations is reduced at late times owing to the enhanced three-dimensionality.

4.4.1 The in-phase case– Unlike the STI disturbance cases described earlier, for oblique initial three-dimensional disturbances, $\Gamma_x(t = 0)$ varies in the streamwise direction. The peak levels for the in-phase case are found in the MP and CP. This peak level is taken to be the same as the initial value of Γ_x used in the ROLLUP simulation, $\Gamma_x^0/\Gamma_z = 0.025$.

The evolution of the in-phase case (OBLIN) is shown in figures 32 to 34. Formation of the cup in the BP is shown in figure 32. At early times (fig. 32(a)), the intensification of the cup spanwise vorticity and the depletion of spanwise vorticity in the rest of the roller core progress faster than in ROLLUP (fig. 15(a)). By τ_o, however, the BP distributions of ω_z are similar in form and magnitude (figs. 32(c), 15(c)). The vortex-stretching mechanism responsible for the generation of the cups is the same as that in ROLLUP, and the CP ω_x distribution exhibits "quadrupoles" similar to those of figure 17. Wisps of spanwise vorticity are also evident in the BP. In figure 32(c), the downstream wisp contains vortex lines connecting the ribs, and the more upstream wisp contains vortex lines connecting sub-rib structures.

The development of the RP ω_z is also similar to that in the ROLLUP simulation (fig. 15). Again, however, the early development is more rapid. By $t = 4.5$, sections of the two cups on either side of the RP are already visible in that plane. By τ_r, there is more positive ω_z in the RP than in ROLLUP, but by τ_o, the RP ω_z is similar to that of figure 15(f).

Streamwise and vertical vorticity contours in the RP resemble those of ROLLUP (fig. 11) but again OBLIN develops more rapidly. At early times, the ω_x and ω_y levels are higher, and the opposite-sign core vorticity is proportionately stronger. The fact that OBLIN initially develops faster than ROLLUP might be expected from the structure of the initial condition. The distribution of streamwise vorticity resulting from the initial oblique disturbance used for OBLIN corresponds more closely to the developed state toward which the flow is evolving; that is, ω_x and ω_y in the roller core are opposite in sign to ω_x and ω_y of the rib at the same spanwise location. This leads to the earlier formation of the CP ω_x quadrupoles, which in turn provides the stretching mechanism for cup generation earlier in the layer development.

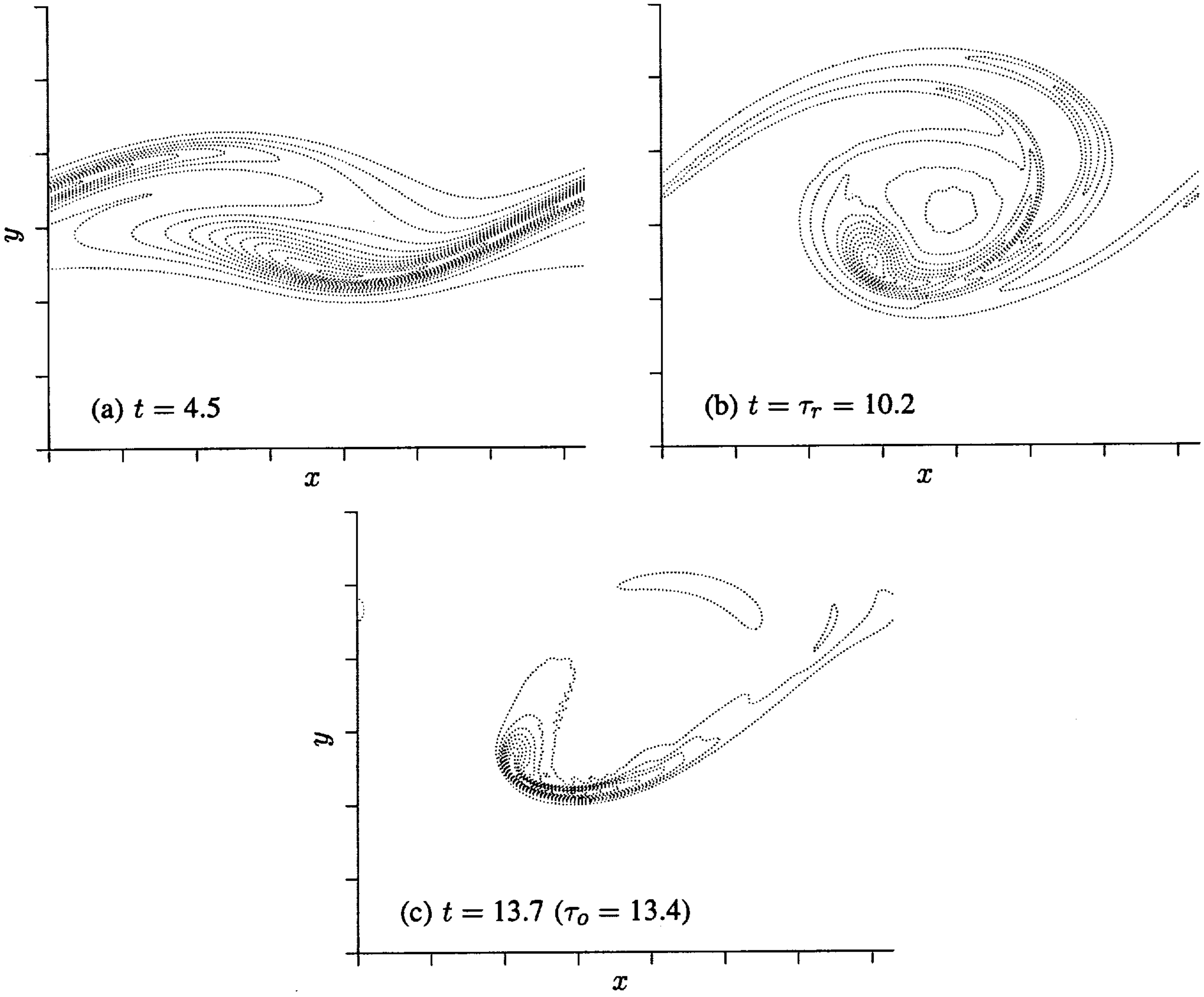

Figure 32. Contour plots of spanwise vorticity in the BP of OBLIN. Contour increments are (a) -0.3, (b) -0.5, and (c) -1.0. Tic marks are at δ_ω^0 intervals.

The passive scalar field in the MP (fig. 33(a)) indicates that the rib streamwise vorticity has collapsed as it does in ROLLUP. Because of flow symmetry, the rib spacing is uniform in this plane. In the CP at the same time (fig. 33(b)), the rib cross sections are not equally spaced, implying that the ribs are oblique. This can be clearly seen in figure 34(a)(at an earlier time). The ribs are thus not as confined to the RP as in ROLLUP. Note that the CP ω_x quadrupole mentioned above is also affected by the oblique ribs, and the upper- and lower-rib cross sections are not centered above the core vorticity contours. By τ_o, the OBLIN ribs are directly above each other in the CP (fig. 33(c)). This is not the result of the ribs returning to a single spanwise plane but rather of their assuming an S-shape, with the mid-braid section still oblique but now with positive ω_z (fig. 34(b)). The ROLLUP simulation ribs also become S-shaped at this point (fig. 18(f)), but their tips are not above each other in the CP (fig. 17(c)).

The oblique ribs observed during the early development of the OBLIN simulation resemble the ribs observed in experiments in which the domain width is not very large. This might be expected, since end-wall effects could provide a mechanism to produce oblique-mode energy rather than the STI

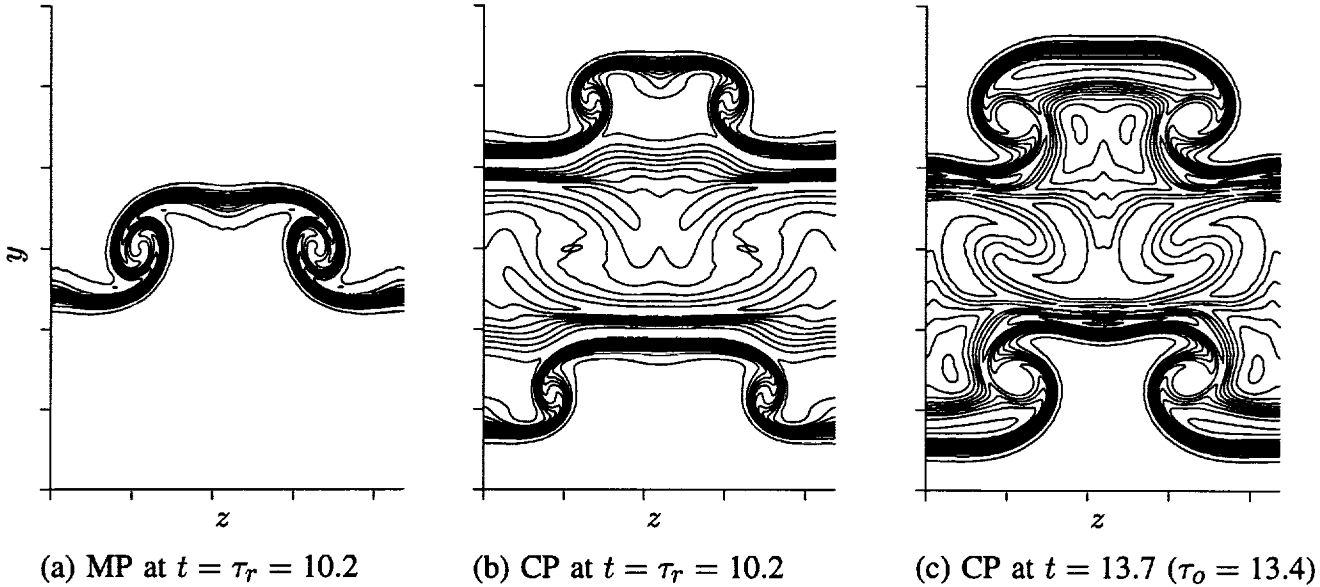

(a) MP at $t = \tau_r = 10.2$ (b) CP at $t = \tau_r = 10.2$ (c) CP at $t = 13.7$ ($\tau_o = 13.4$)

Figure 33. Contour plots of the passive scalar (T) in the MP and CP of OBLIN with contour increment 0.08 from 0.02 (bottom) to 0.98 (top). Tic marks are at δ_ω^0 intervals.

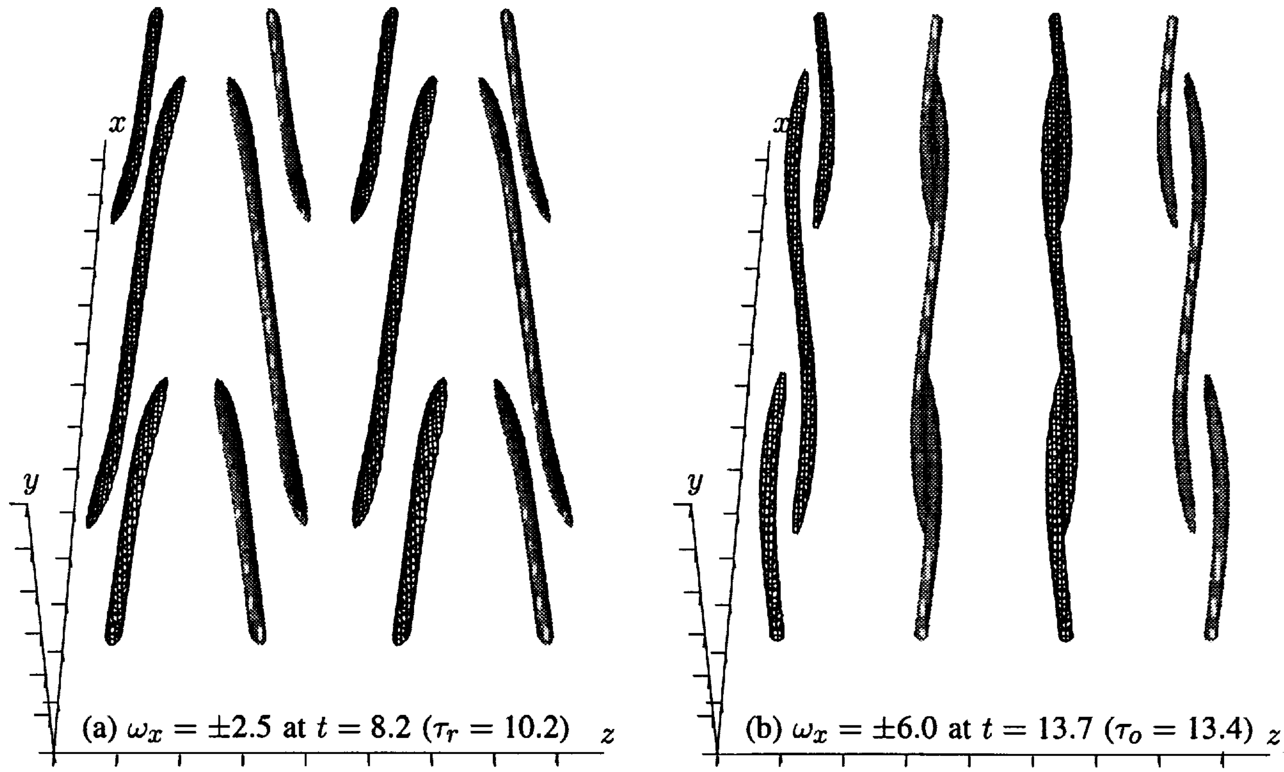

(a) $\omega_x = \pm 2.5$ at $t = 8.2$ ($\tau_r = 10.2$) (b) $\omega_x = \pm 6.0$ at $t = 13.7$ ($\tau_o = 13.4$)

Figure 34. Surfaces of constant streamwise vorticity magnitude in OBLIN. Cross-hatched surfaces represent negative ω_x, and shaded surfaces represent positive ω_x. Periodicity has been used to extend the domain in both the streamwise and spanwise directions. Tic marks are at δ_ω^0 intervals.

disturbances presumably generated by upstream defects. Flow visualizations by Lasheras, Cho, and Maxworthy (1986) show oblique ribs similar to those shown in figure 34(a) (see their figs. 10 and 14(c), for example).

The evolution of A_{10}, A_{01}, and A_{11} is shown in figure 35.[19] The growth of the two-dimensional disturbance is similar to that in the ROLLUP simulation. The oblique character of the rib vortices is reflected in the relative amplitudes of A_{11} and A_{01} (although it should be noted that these quantities are also affected by the roller vorticity distribution). Amplitude A_{11} is initially dominant when the ribs are oblique. Just after τ_r, A_{11} is overtaken by A_{01}, which is consistent with the ribs being on average predominantly streamwise at late times. As indicated in figure 7, for initial STI disturbances, A_{11} overtakes A_{01} before τ_r and stays larger for the remainder of the simulation. This is consistent with the ribs in ROLLUP being more oblique at late times.

The evolution of the streamwise circulation at various streamwise locations is shown in figure 36. As mentioned above, the initial circulation varies in x. However, the circulation dependence on streamwise location weakens as the rib is formed. By τ_r, the collapsed rib has the same circulation over most of its extent. The eventual sudden circulation increase resulting from oversaturation occurs as in ROLLUP. The evolution of Γ_x^{MP} in the OBLIN simulation is compared with that of the ROLLUP simulation in figure 37(a). Although the OBLIN circulation at $t = 3$ is 8% larger, by τ_r it is just under 70% of the corresponding ROLLUP value. Perhaps it is for this reason that the ROLLUP simulation can "catch up" to the OBLIN simulation (which exhibits faster cup formation and faster growth of ω_x and ω_y early on), resulting in similar flow fields at τ_o. The Lin and Corcos (1984) collapse parameter (fig. 37(b)) correctly predicts collapse for the OBLIN simulation (and for the OBLMID case discussed in sec. 4.4.3).

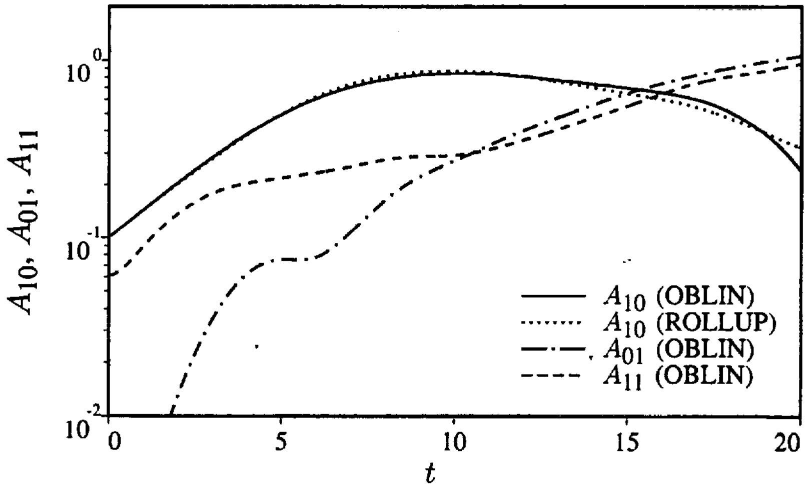

Figure 35. Time development of low-wavenumber amplitudes for OBLIN; ROLLUP included for comparison.

---

[19] The growth of A_{11} at early times is not exponential. There is a short adjustment period (see also fig. 49) because of the lack of ω_y in the initial condition. When the appropriate ω_y is added to the initial condition, A_{11} initially grows exponentially without any adjustment period.

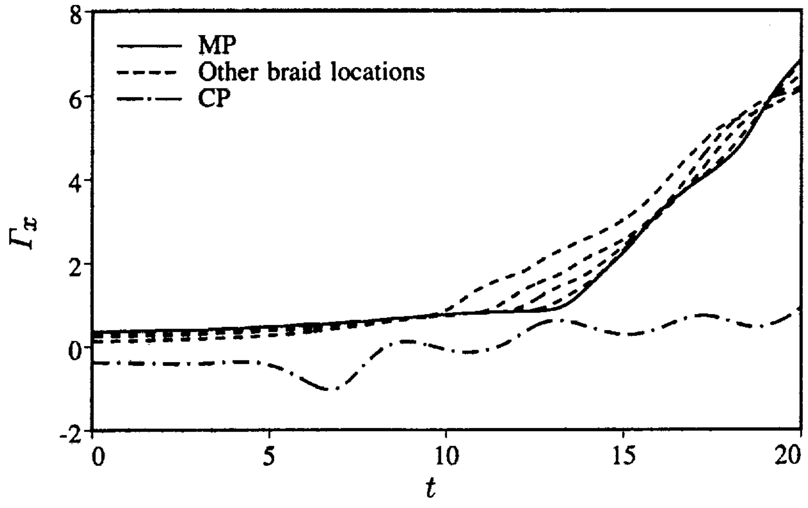

Figure 36. Time development of streamwise circulation for OBLIN. Dashed lines are for various braid region locations progressively farther from the MP as the curves move away from the solid line.

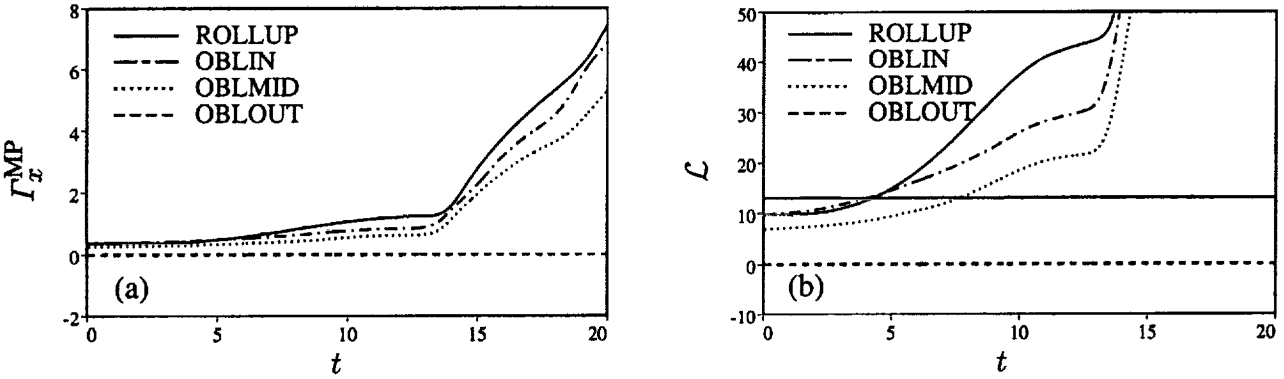

Figure 37. Time development of (a) streamwise circulation (Γ_x^{MP}), and (b) the Lin and Corcos collapse parameter $\mathcal{L}$. The solid line at $\mathcal{L} = 13.1$ in (b) represents the Lin and Corcos collapse criterion.

The evolution of ω_b, S, and δ_m is shown in figure 38. The behavior of the OBLIN simulation is similar to that of the ROLLUP case for all these quantities.

The vorticity extrema for OBLIN are shown in figure 39. The more rapid growth of the peak negative ω_z for OBLIN is apparent, but by τ_o the level is comparable to that of ROLLUP. By τ_o, the ω_x and ω_y extrema, although growing more rapidly early in the flow development, are only 20% larger than those of ROLLUP. In general, although the early development occurs more rapidly, by τ_o the OBLIN flow resembles the ROLLUP case.

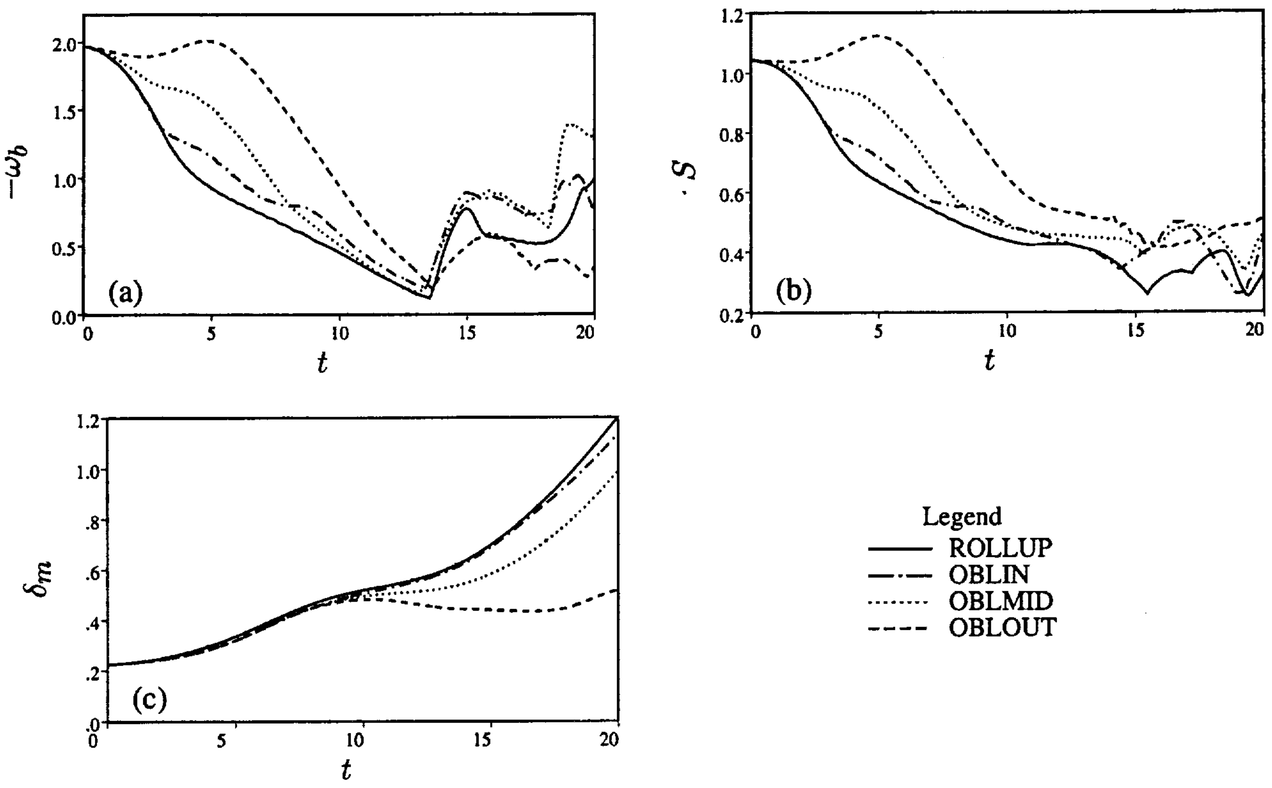

Figure 38. Time development of (a) mid-braid spanwise vorticity, (b) mid-braid strain-rate, and (c) momentum thickness for ROLLUP, OBLIN, OBLMID, and OBLOUT.

4.4.2 The out-of-phase case– The initial condition for the OBLOUT simulation described here is identical to that of the OBLIN case described above except for the relative phasing of the pair of oblique modes to the two-dimensional fundamental. In this case, the initial value of Γ_x is zero in both the MP and CP, and it remains zero for all time because of flow symmetry. This precludes the possibility of ultimately achieving the typical flow state described above. It does not, however, imply that ω_x and ω_y are zero in the MP and CP, but rather that they are antisymmetric in y. As expected, the evolution of this case is markedly different from the simulations described above.

The early (up to $t = 6.9$, $\tau_r = 9.9$) evolution of streamwise vorticity in the RP is shown in figure 40. The induced motion of the developing roller creates riblike structures, but these are qualitatively different from the ribs in ROLLUP (and OBLIN). First, the rib streamwise vorticity is opposite in sign on the upstream and downstream sides of the roller. This is unlike the typical evolution in which ribs of the same sign form on both sides of the roller (at fixed z). Second, in the MP the ribs contain equal amounts of ω_x of both signs (as noted above, this is imposed by flow symmetry in OBLOUT). The roller-core streamwise vorticity becomes opposite in sign to that of the nearby rib as in the typical evolution, but because the upstream and downstream ribs are of opposite sign, the core contains vorticity of both signs. Again, flow symmetry requires that the CP ω_x distribution be antisymmetric. Beyond $t = 6.9$, the ribs have largely moved out of the RP for reasons described below.

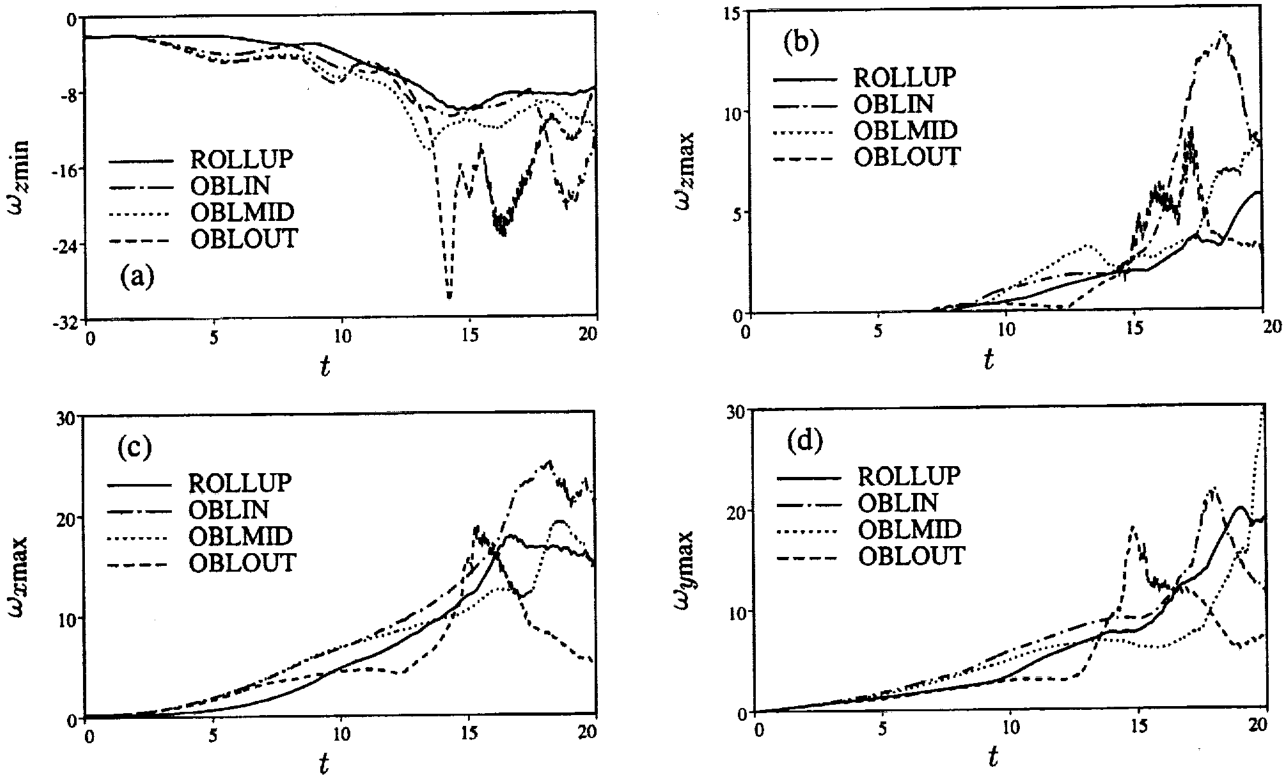

Figure 39. Time development of vorticity component extrema for ROLLUP, OBLIN, OBLMID, and OBLOUT. Note that $\omega_{x\min}$ and $\omega_{y\min}$ are equal in magnitude but opposite in sign to $\omega_{x\max}$ and $\omega_{y\max}$.

The evolution of the MP ω_x distribution is given in figure 41 (the evolution of ω_y is similar). The vorticity contours are antisymmetric in y, and therefore the circulation Γ_x in each spanwise half of the domain is zero, as noted above. The induced motion of this periodic array of "vortex dipoles" moves each one toward another dipole (a periodic image) of opposite sign (fig. 41(b)). The resulting quadrupole is held near $y = 0$ by the compressive component of the two-dimensional strain field associated with the developing rollers. Although the braid ω_x is initially strengthened by the expansive component of the two-dimensional strain field, the large gradients developing in the quadrupole ultimately lead to the viscous annihilation of the rib structures (fig. 41(c)). The annihilation of the ribs leaves only core vorticity. This core vorticity, however, is not two-dimensional.

Note that the movement of the ribs toward the spanwise domain boundaries in figure 41 is possible because the point-reflection symmetry point is now located at these boundaries rather than in the RP. In the STI disturbance simulations and in OBLIN, the ribs were anchored in the RP by the point-reflection symmetry point located there. Phasings intermediate between OBLIN and OBLOUT (i.e., OBLMID) do not possess any point-reflection symmetry.

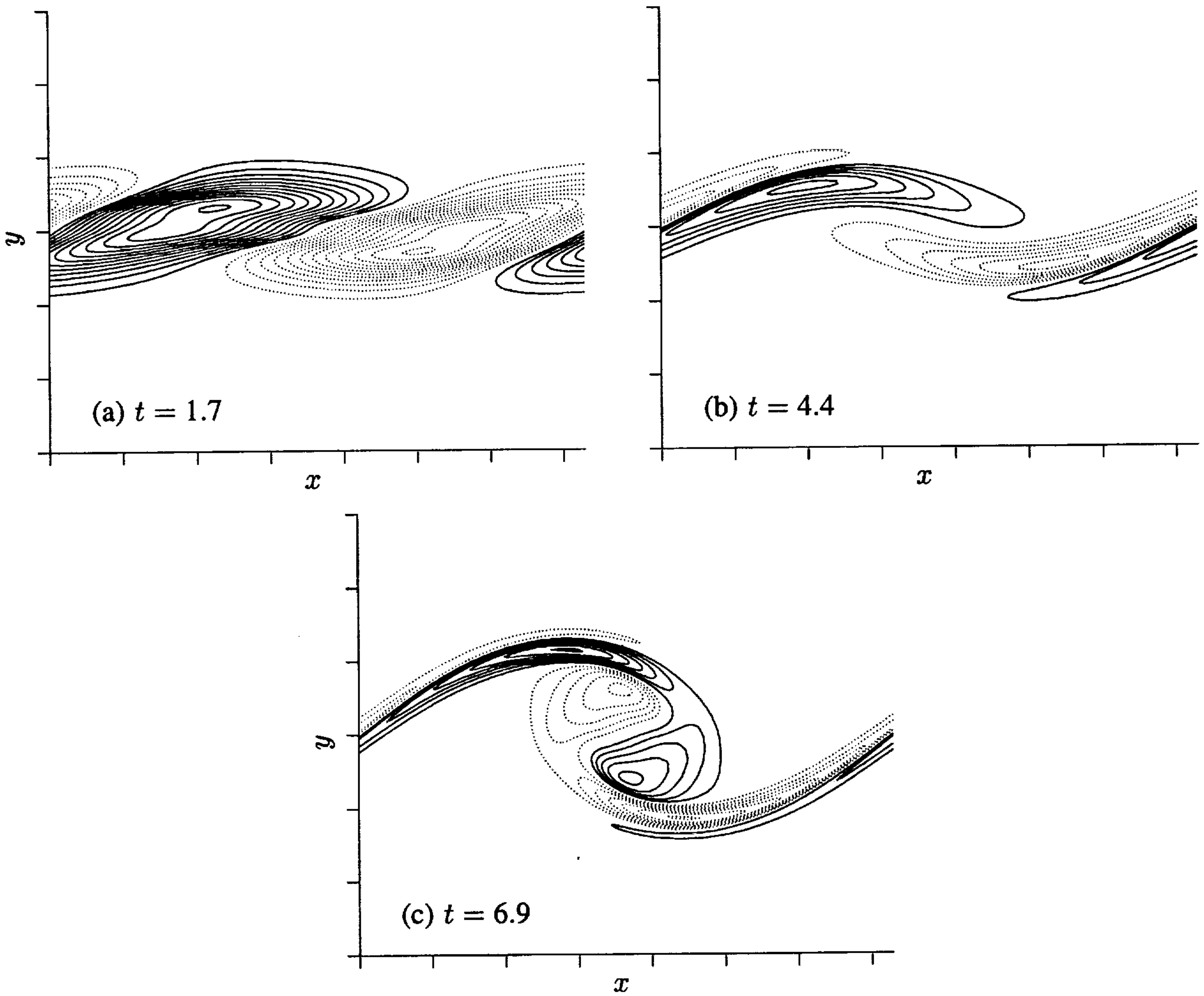

Figure 40. Contour plots of streamwise vorticity in the RP of OBLOUT (it is zero in the BP). Contour increments are (a) ±0.03, (b) ±0.2, and (c) ±0.3. Solid contours indicate positive vorticity, dotted contours indicate negative vorticity, and tic marks are at δ_ω^0 intervals.

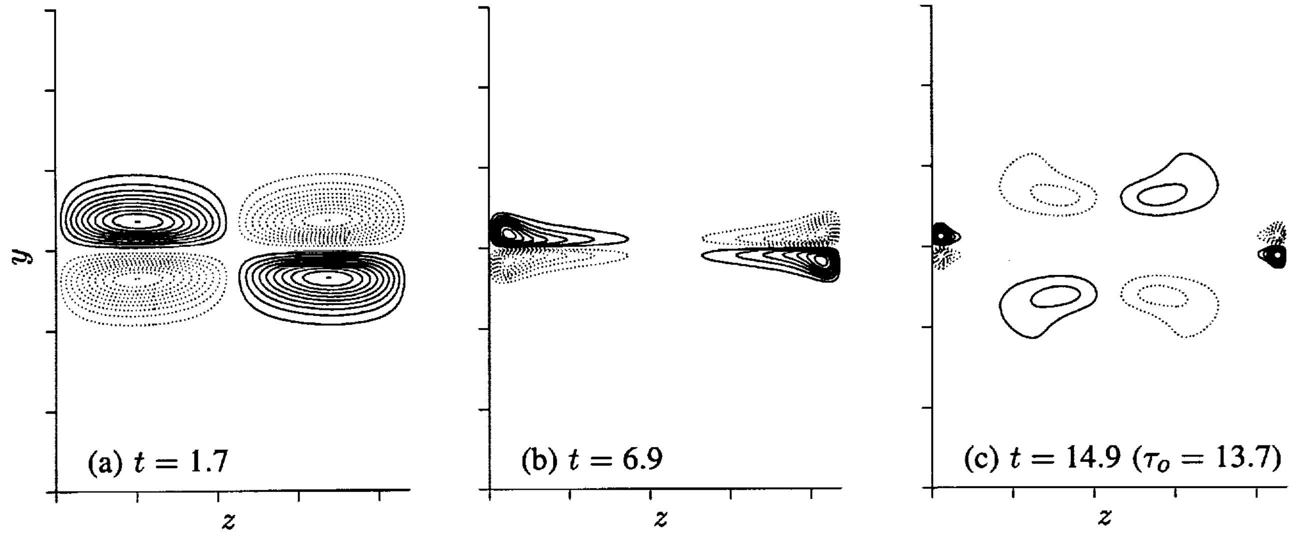

(a) $t = 1.7$ (b) $t = 6.9$ (c) $t = 14.9$ ($\tau_o = 13.7$)

Figure 41. Contour plots of streamwise vorticity in the MP of OBLOUT. Contour increments are (a) ±0.02; and (b),(c) ±0.3. Solid contours indicate positive vorticity, dotted contours indicate negative vorticity, and tic marks are at δ_ω^0 intervals.

At early times, the ω_x distribution in the CP is similar to that in the MP but of opposite sign (fig. 42(a)). Again, each dipole moves toward a neighbor, this time meeting in the center of the computational domain (forming a quadrupole of the same sign as the one in the MP). Unlike in the MP, the dynamics in the CP are not primarily determined by the streamwise vorticity distribution and the two-dimensional strain field alone. The spanwise vorticity of the two-dimensional roller plays an important role in the CP, and the ω_x distributions become more complicated. By $t = 4.4$, streamwise vorticity from farther up and downstream is drawn into the CP, creating two new outer lobes of ω_x (fig. 42(b)). This vorticity has the opposite sign of that already present in the CP (again because the initial distribution changes sign in x at fixed z). As the spanwise roller develops, core ω_x opposite in sign to that of the nearby rib is formed (fig. 40(c)). This creates two new inner lobes in the CP (fig. 42(c)) and results in a pattern that is more complex than that associated with the typical flow evolution (six lobes of ω_x in each spanwise half of the domain rather than three; compare with figure 17(a)).[20] Shortly after τ_r, yet another pair of ω_x lobes is formed near the centerline of the CP (fig. 42(d)).

Despite the more complicated CP ω_x distribution, a cup-generating mechanism similar to that of ROLLUP still exists. However, in OBLOUT the cups form at the same spanwise location on both sides of the roller. The early-time (up to $t = 8.9$, $\tau_r = 9.9$) evolution of the spanwise vorticity in the CP is shown in figure 43. The strong spanwise vorticity is present in regions that are being stretched by the ω_x distributions in figure 42. At $t = 4.4$ (figs. 43(a), 42(b)), this stretching is occurring at $y = 0$ near the spanwise boundaries ($\omega_{z\text{min}} = -4.2$) and, to a lesser extent, at the outer edges of the layer in the middle of the domain ($\omega_{z\text{min}} = -2.3$). The "vortex compression" in the center of the CP reduces the ω_z amplitude there ($\omega_{z\text{min}} = -0.9$). At $t = 6.9$ (figs. 43(b), 42(c)), the opposite-sign core ω_x has changed the stretching locations at the spanwise boundaries. At these locations, the centerline ω_z is now being reduced and cups are forming at $y = \pm 0.7$, that is, on both sides of the layer. The ω_z at the

---

[20] At this point (and from here on) the CP ω_y distribution, although exhibiting a similar number of lobes in a similar pattern, often has the opposite sign of ω_x at the same location.

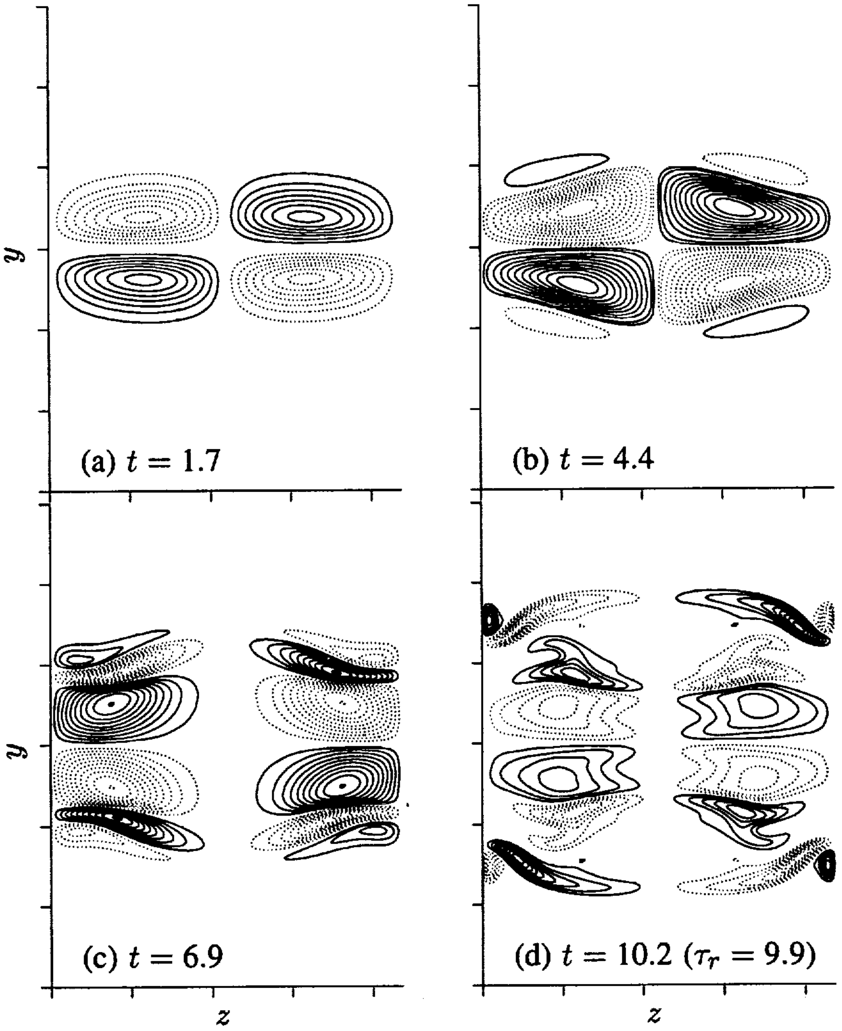

Figure 42. Contour plots of streamwise vorticity in the CP of OBLOUT. Contour increments are (a) ±0.03, (b) ±0.06, (c) ±0.2, and (d) ±0.3. In (b), there are two extra contours at ±0.03 to show the additional "lobes." Solid contours indicate positive vorticity, dotted contours indicate negative vorticity, and tic marks are at δ_ω^0 intervals.

center of the CP is now being stretched, and by $t = 8.9$ (fig. 43(c)), $\omega_{z\min} = -5.5$ at this location. At this time $\omega_{z\min} = -0.2$ on the centerline at the spanwise boundaries.

The development of the spanwise vorticity in the BP is shown in figure 44. The two cups in figure 43(b) can be seen in figure 44(a). As time progresses, these cups coalesce into a hoop-shaped structure (fig. 44(b)). The interior of the hoop is virtually irrotational (ω_x and ω_y are zero in the BP by symmetry). Vortex stretching is responsible for this depletion, as noted above.

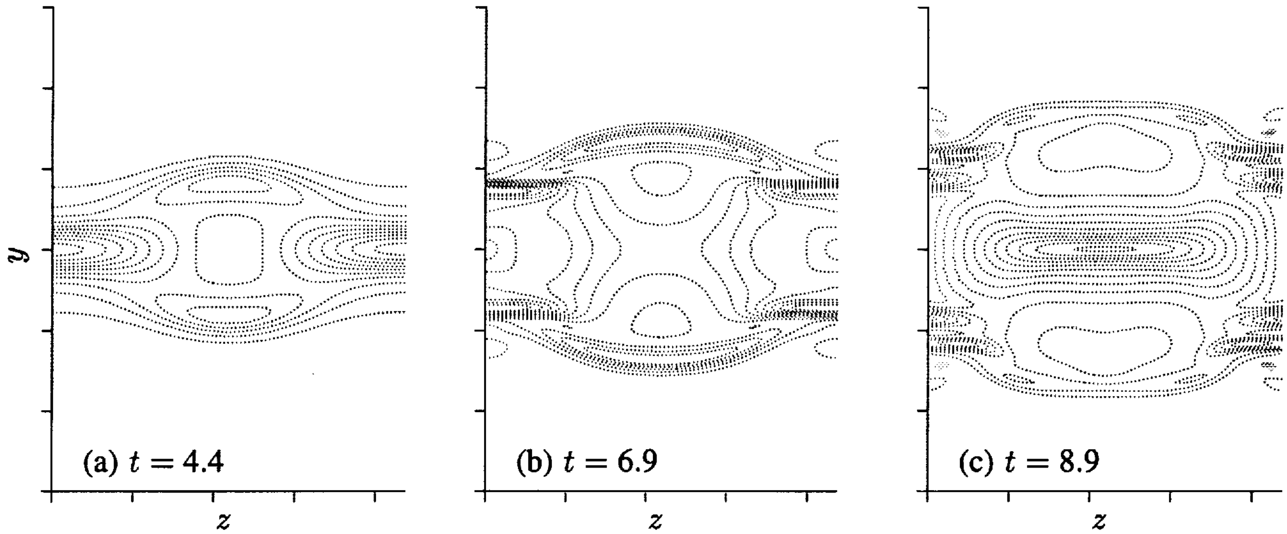

Figure 43. Contour plots of spanwise vorticity in the CP of OBLOUT at early times. Contour increments are (a),(b) -0.4; and (c) -0.5. Shaded regions indicate regions of positive ω_z (opposite in sign to the mean vorticity), solid contours indicate positive vorticity, dotted contours indicate negative vorticity, and tic marks are at δ_ω^0 intervals.

From this point on the layer evolution is quite complex and dominated by vortex stretching. The new lobes of ω_x in the CP at $t = 10.2$ (fig. 42(d)) once again switch the stretching and compression locations. The hoops at the spanwise boundaries become weak, but a new hoop forms in the center of the domain (fig. 45). From $t = 10.2$ (fig. 45(a)) to $t = 11.5$ (fig. 45(b)), $\omega_{z\text{min}}$ drops from -6.6 to -0.6 in the middle of the CP, and it is still decreasing in magnitude at $t = 11.5$. This relatively short time scale is an indication of the strength of the vortex-stretching processes involved. At the same time, vortex stretching at the centerline on the spanwise boundaries is creating strong ω_z. By $t = 14.0$ (figs. 44(c), 44(d), 45(c)), $\omega_{z\text{min}}$ reaches -24.9 at this location, over 10 times its initial level. Again, the fact that fluid in this region was nearly irrotational at $t = 10.2$ indicates how fast vortex stretching can change the vorticity levels.

At $t = 14.0$, another pair of ω_x lobes (opposite in sign to what was there previously) forms in the CP. The regions of stretching and compression change yet again, and a new hoop begins to form on the spanwise boundary. This roughly time-periodic standing oscillation is illustrated in the three-dimensional surface plots of ω_z shown in figure 46. The period of one complete cycle (from a hoop in one BP, through its destruction, to re-formation of another hoop in the same BP) appears to be $\Delta t \approx 8$.

At $t = 14.0$, it appears that the strong, thin ω_z layer created in the BP (fig. 44(c)) is undergoing a secondary, smaller-scale roll-up process of its own (fig. 44(d)). Examination of this vortex sheet indicates that it is locally two-dimensional, extending over approximately half the spanwise domain (fig. 45(c)). Its vorticity thickness is about one sixth that of the initial error-function profile. The expected most-unstable disturbance wavelength for this vortex sheet is thus one sixth of the streamwise computational domain extent, in agreement with the scale of the roll-up in figures 44(c) and 44(d)(the rectangle in these figures has a streamwise extent of $\lambda_x/6$ and is centered on the small-scale roll-up). In the enlarged view (fig. 44(d)), it can be seen that the roller proportions are similar to those in figure 44(a)(although it appears two-dimensional). Because this layer is much thinner than the original one (and yet is subjected

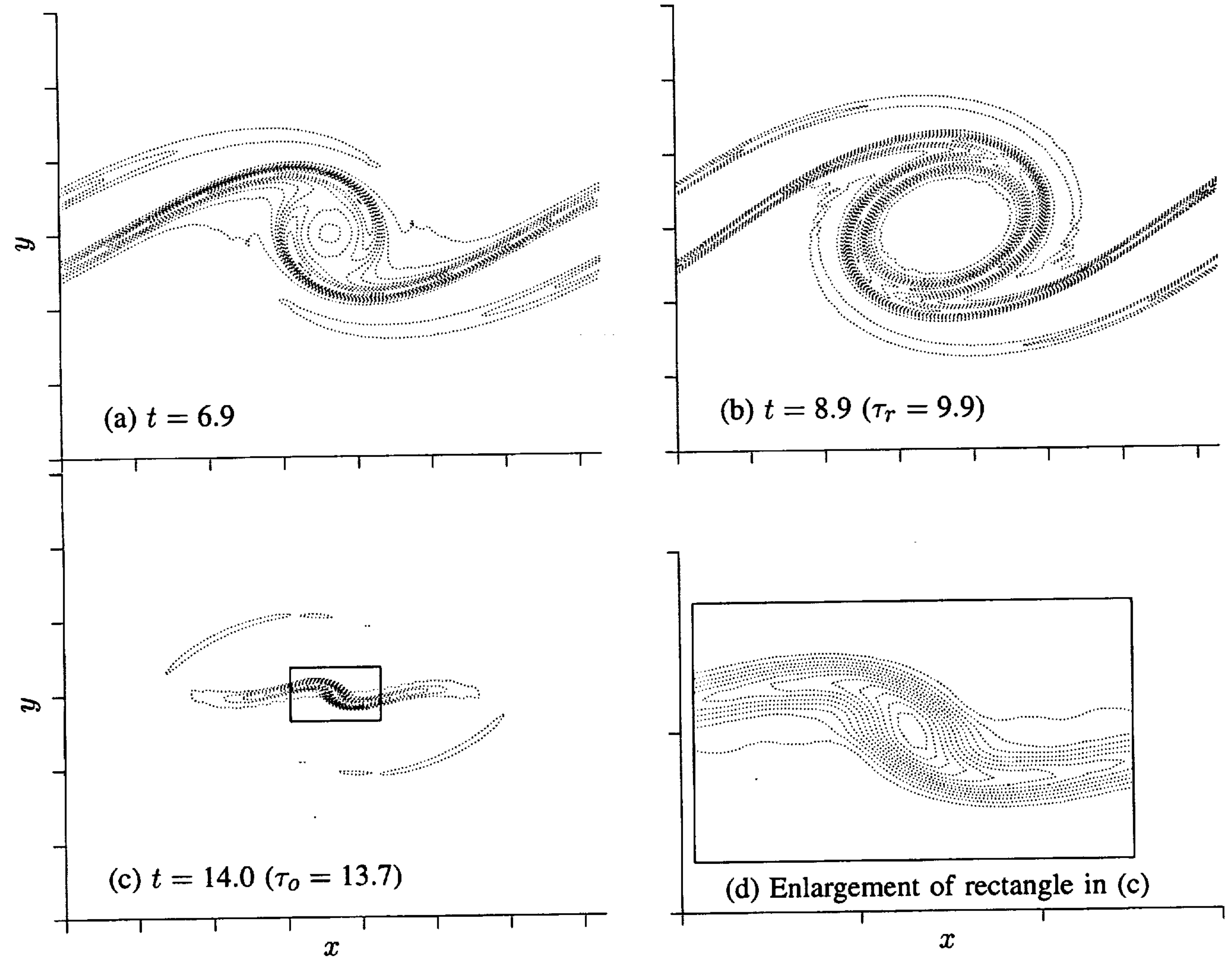

Figure 44. Contour plots of spanwise vorticity in the BP of OBLOUT. Contour increments are (a),(b) -0.5; and (c),(d) -2.0. The box in (c) and (d) is the central one sixth of the streamwise domain. Tic marks are at δ_ω^0 intervals, except for in (d), where they are at intervals of $0.5\delta_\omega^0$ ($3.0\delta_\omega^0 \leq x \leq 4.5\delta_\omega^0$ and $-0.5\delta_\omega^0 \leq y \leq 0.5\delta_\omega^0$).

to nearly the full velocity difference across the original layer), its time scale for roll-up is shorter (of the order of 1 to 2 time units for disturbances with amplitudes similar to those used in the initial condition). Similar small-scale roll-ups have been observed in other highly three-dimensional flows.

The evolution of the Fourier mode energies for this case is different from that of OBLIN. The growth and saturation of A_{10} is virtually identical to that of ROLLUP. Amplitude A_{11}, although similar to the OBLIN curve up to about $t = 2$, drops to about a third of the OBLIN level in the developed state. Although A_{01} initially grows more rapidly in OBLOUT than in OBLIN, it is almost an order of magnitude smaller by the end of the simulation. The absence of strong ribs is apparently responsible for this reduced energy in the three-dimensional modes.

The evolution of the vorticity extrema, of the mid-braid statistics, and of the momentum thickness is shown in figures 38 and 39 along with the results for OBLIN. As expected, the development of these

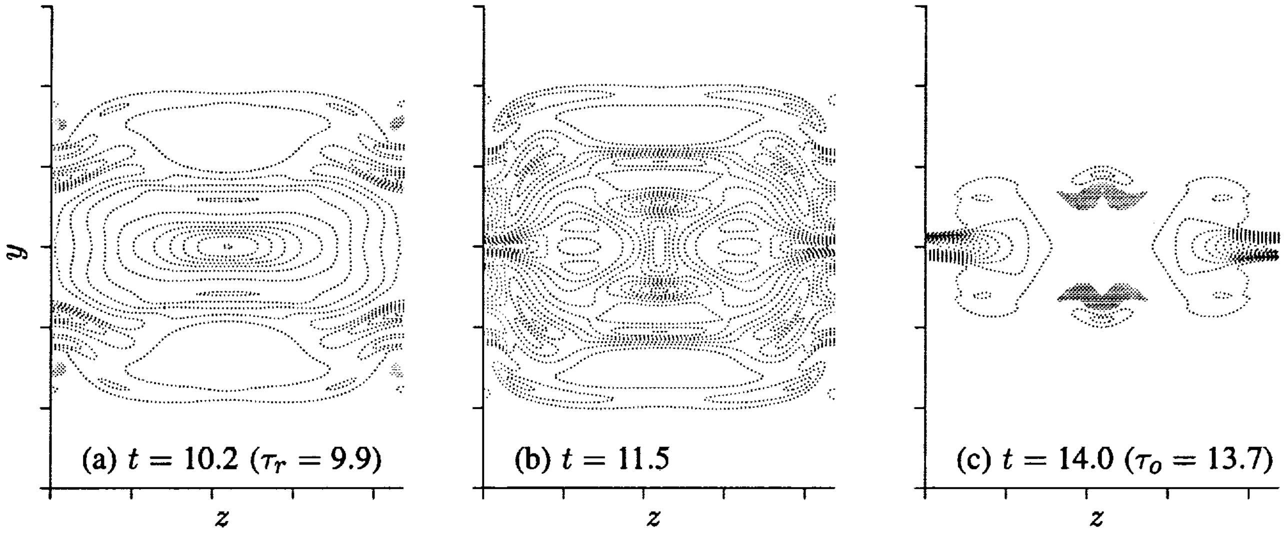

Figure 45. Contour plots of spanwise vorticity in the CP of OBLOUT at late times. Contour increments are (a) -0.6, (b) -0.3, and (c) -2.0. Shaded regions indicate regions of positive ω_z (opposite in sign to the mean vorticity), solid contours indicate positive vorticity, dotted contours indicate negative vorticity, and tic marks are at δ_ω^0 intervals.

quantities is different from that in the OBLIN case. As can be seen in figure 38(c), the absence of developed rib structures seems to prevent the post-τ_r layer thickening observed in the typical evolution (indeed the layer thickness for the OBLOUT case is similar to the corresponding two-dimensional flow; fig. 8(c)).

4.4.3 Intermediate phasing– The OBLMID simulation evolved from an initial condition halfway between those of the OBLIN and OBLOUT cases. Its development is by far more similar to OBLIN than to OBLOUT. Well-defined rib structures do evolve, and, associated with them, A_{11} and A_{01} both become larger than A_{10} after $t \approx 16$ (a behavior exhibited by OBLIN but not OBLOUT). The circulation evolution (fig. 37(a)) parallels OBLIN at a lower level since the initial MP level is reduced for this phasing. The layer thickness (fig. 38(c)) is intermediate between OBLIN and OBLOUT, but is closer to that of OBLIN. The mid-braid strain-rate (fig. 38(b)), the mid-braid spanwise vorticity (fig. 38(a)), and the vorticity extrema (fig. 39) are all closer to those of OBLIN as well. It seems that the "typical evolution" is indeed typical and that the OBLOUT phasing leads to a singular flow evolution, analogous to the two-dimensional subharmonic resonance phenomena (Riley and Metcalfe 1980; Monkewitz 1988) in which two-dimensional pairings are significantly delayed for a narrow range of relative phasings of the two-dimensional subharmonic to the two-dimensional fundamental.

This intermediate phasing does not have a point-reflection symmetry point, and therefore, the ribs that evolve are not fixed at $z = L_z/4$ and $z = 3L_z/4$ (fig. 47). For the particular intermediate phasing used here, the ribs form in $+/-$ pairs (as one moves in the positive z-direction). Another intermediate phasing exists that would form $-/+$ rib pairs. The spacing between pairs is nearly double the spacing between ribs of a pair at $t = 12.2$ (a time between τ_r and τ_o). Similar behavior was observed in the wake-component simulations discussed in section 4.3.7. Because the ribs are no longer equally spaced, they have a net self-induced motion that moves them below the domain centerline in the MP (indicated by the middle tic mark in figure 47).

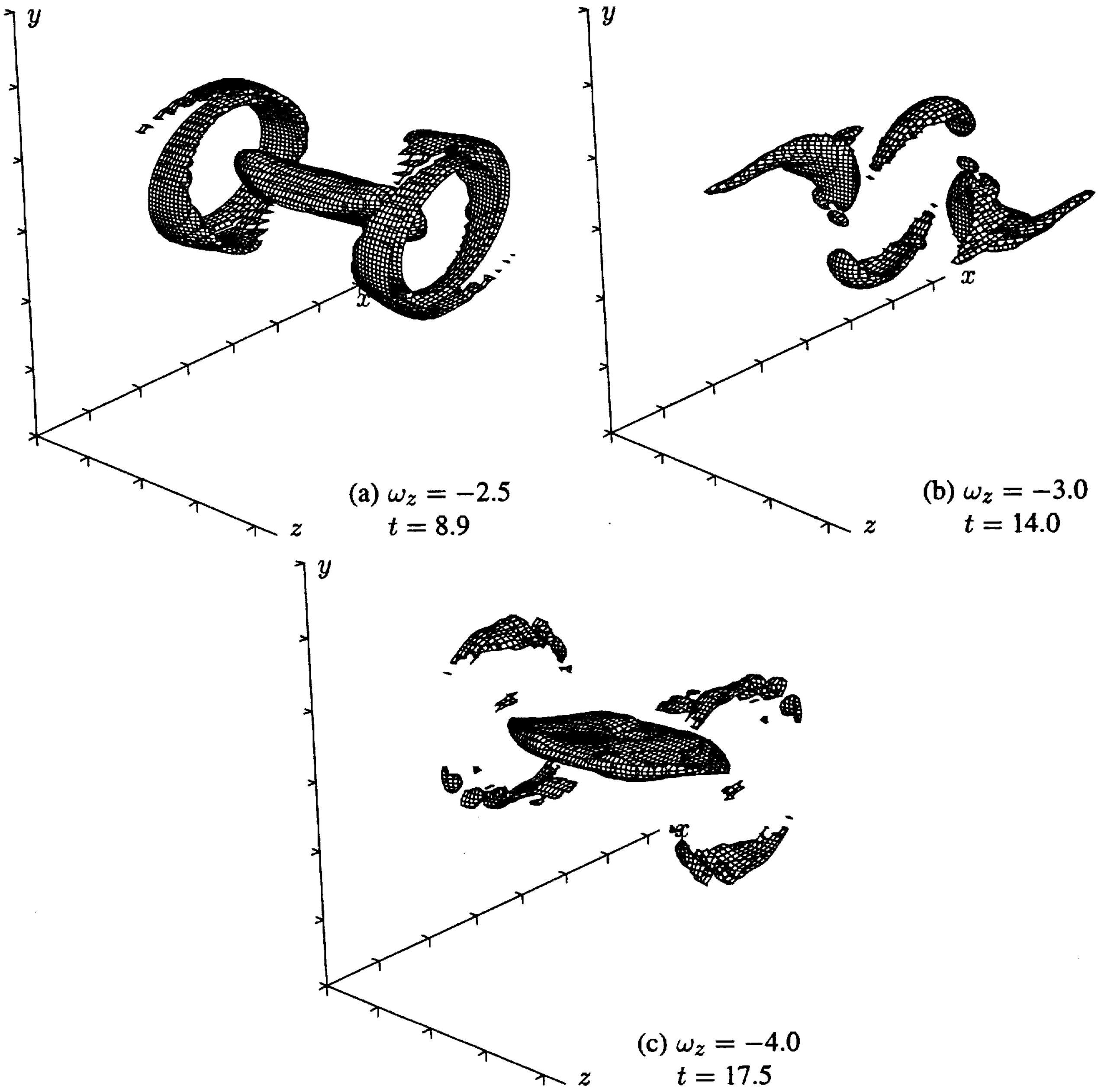

(a) $\omega_z = -2.5$
$t = 8.9$

(b) $\omega_z = -3.0$
$t = 14.0$

(c) $\omega_z = -4.0$
$t = 17.5$

Figure 46. Surfaces of constant spanwise vorticity magnitude in OBLOUT. Tic marks are at δ_ω^0 intervals.

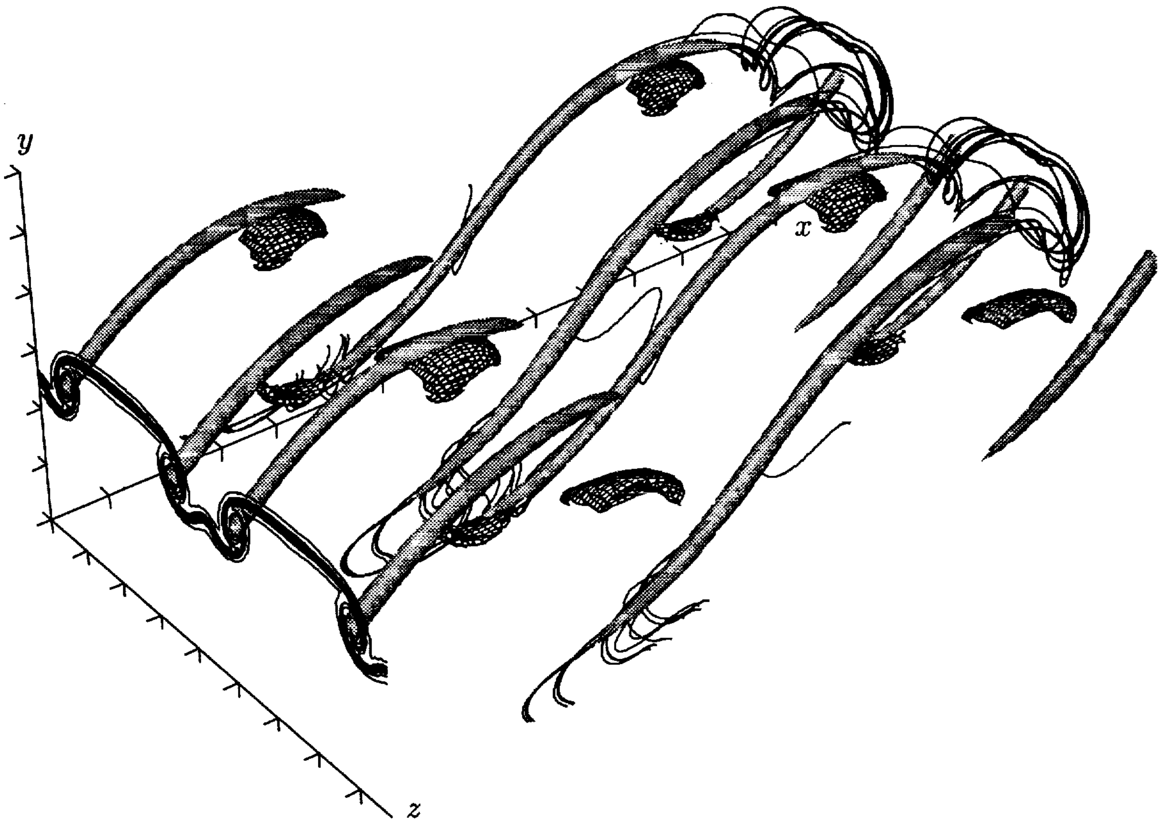

Figure 47. Surfaces of constant vorticity magnitude, rib vortex lines, and contours of the passive scalar quantity in the MP of OBLMID at $t = 12.2$ ($\tau_r = 10.0$ and $\tau_o = 13.0$). Cross-hatched surfaces represent $\omega_z = -4.0$, and shaded surfaces represent $\sqrt{\omega_x^2 + \omega_y^2} = 4.0$. The rib structures contain ω_x and ω_y of the same sign, and the sign alternates in z (positive for the closest rib). Periodicity has been used to extend the domain in both the streamwise and spanwise directions, and the same vortex lines go through both of the counterrotating rib vortex pairs (concealed by the rib surface contour). Contour increment for the passive scalar quantity is 0.16 from 0.02 (bottom) to 0.98 (top). Tic marks are at δ_ω^0 intervals.

4.4.4 Single oblique-mode initial disturbances– Two simulations (SOBL1 and SOBL2) with single oblique-mode initial disturbances of different amplitude were made. As mentioned above, for this case there is no issue of phasing relative to the two-dimensional fundamental disturbance. Surface contours of the initial ω_x distribution are shown in figure 48. Again, it should be noted that these surfaces do not correspond to vortices, but rather simply indicate regions where the predominantly spanwise-oriented vortex lines are slightly kinked. Also, because the ω_x disturbance is oblique, the initial ω_z distribution is three-dimensional.

It is immediately apparent from figure 48 that the spanwise flow symmetry found in the previous three-dimensional simulations is no longer present. Because of this, the peak positive and negative ω_x (and ω_y) will no longer have the same magnitude. Also, the A_{11} energy is no longer composed of equal amounts of A_{11}^+ and A_{11}^-. Here, only A_{11}^+ has been initialized. The evolution of A_{11}^+ and A_{11}^- (along with their sum A_{11}) is shown for the low-initial-amplitude simulation (SOBL1) in figure 49. The results for the high-amplitude case up to about τ_o can be obtained by multiplying the ordinate scale by a factor of 2 (the initial amplitude ratio between these cases), again indicating that the Fourier mode energies

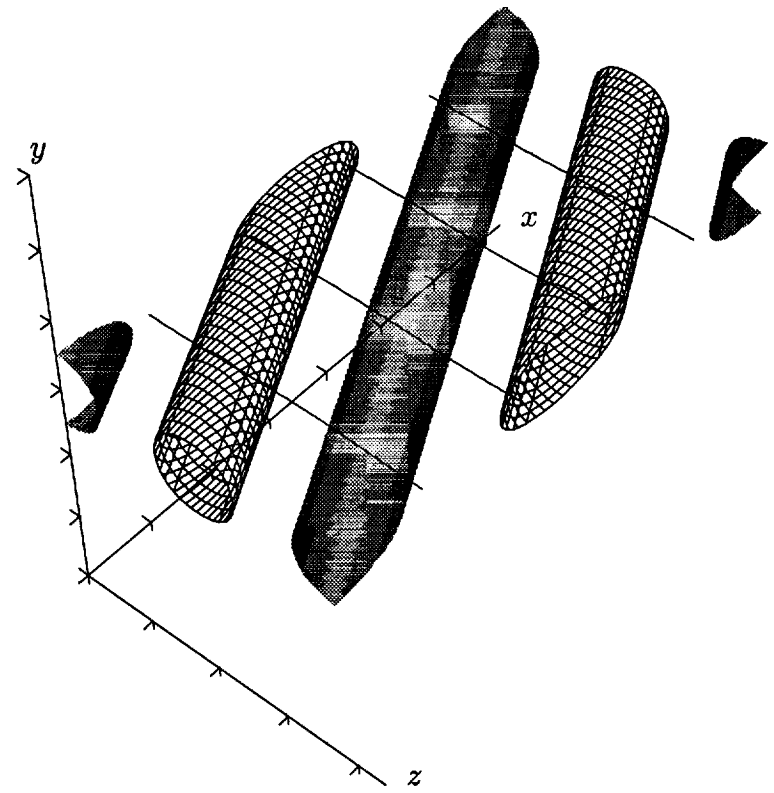

Figure 48. Surfaces of constant streamwise vorticity magnitude and some vortex lines of SOBL1 at $t = 0$. Cross-hatched surfaces represent $\omega_x = -0.04$, and shaded surfaces represent $\omega_x = 0.04$. Tic marks are at δ_ω^0 intervals.

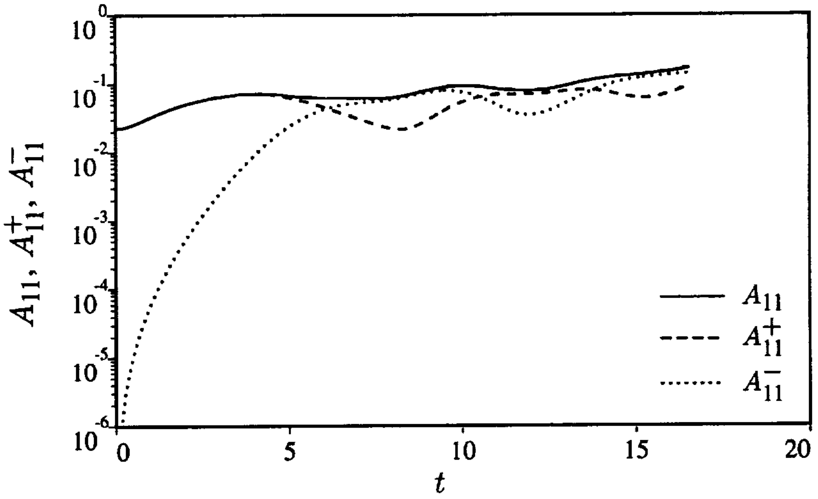

Figure 49. Time development of low-wavenumber amplitudes for SOBL1.

are interacting linearly with a few low-wavenumber modes. The $(1,-1)$ mode amplitude $(A_{\bar{1}1}^{-})$ grows rapidly from energy transfer through the nonlinear wavenumber triad involving $(1,1)$ (initialized) and $(2,0)$ (the first two-dimensional harmonic resulting from interactions of the two-dimensional disturbance with itself) and through interaction with the mean flow. For $t > 6$ $(\tau_r = 12.5)$, it can be seen that A_{11}^{+} and $A_{\bar{1}1}^{-}$ are similar in amplitude and are oscillating in time.

By placing the two-dimensional roller in the center of the domain in figure 48, it can be seen that the streamwise location of ω_x relative to the roller at $z = 0, L_z/2$, and L_z is similar to that of OBLIN, whereas that at $z = L_z/4$ and $3L_z/4$ is like that of OBLOUT. It might thus be expected that these simulations will result in some combination of characteristics of OBLIN and OBLOUT. In reality, it seems that the OBLOUT behavior dominates. Neither of the SOBL simulations forms well-organized rib structures; therefore, they stay more two-dimensional than OBLIN (the Fourier mode energies resemble those of the OBLOUT simulation where A_{10} is greater than A_{01} and A_{11} for all time).

The flow evolution seems to be dominated by twisted vortex lines, with some regions being twisted tighter (stronger vorticity) than others. Vortex lines in the rolled-up roller core are shown in figure 50 at times $t = 12.2$ and $t = 15.2$. Their appearance is similar to that of a rope formed by several strands that has been twisted so as to unravel the strands (weaken the vorticity) at some location. The position of this unraveled section then propagates in the spanwise direction. The peak ω_x and ω_y occur in the roller core and are the streamwise and vertical components of the "twisted" roller. The weaker ω_x and ω_y present in the braid region are also associated with twisted vortex lines, not with streamwise rib vortices.

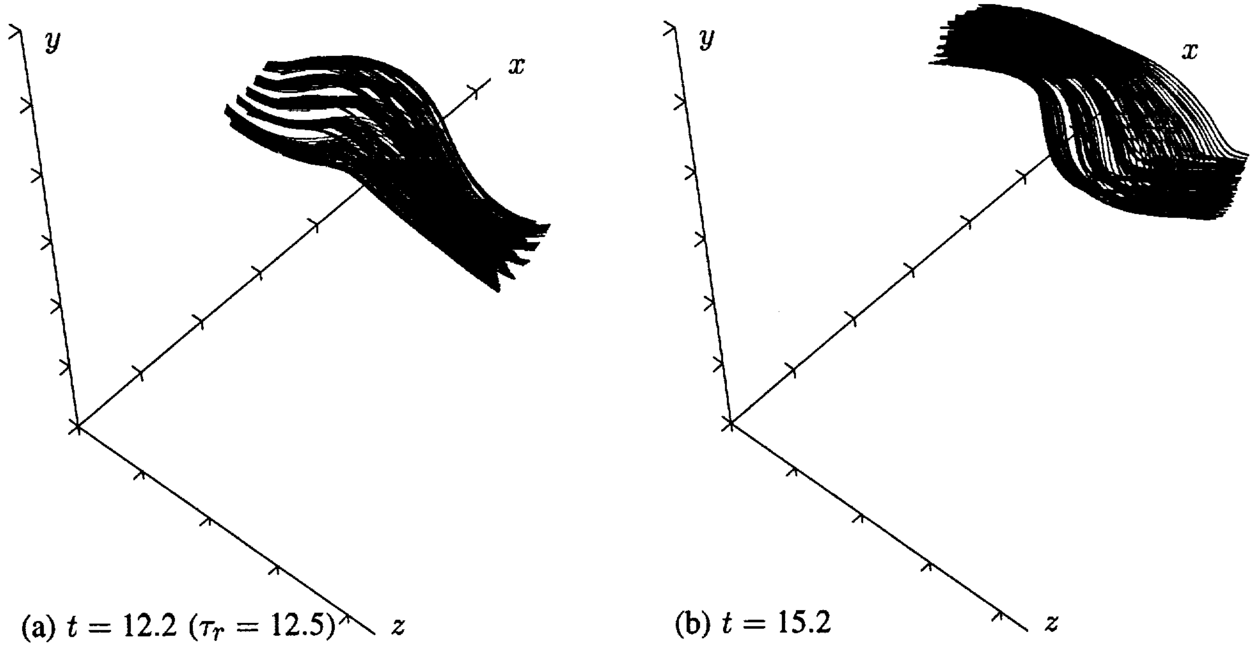

(a) $t = 12.2$ $(\tau_r = 12.5)$ (b) $t = 15.2$

Figure 50. Vortex lines through the roller core of SOBL1. Tic marks are at δ_ω^0 intervals.

4.5 Combinations of Streamwise and Oblique Initial Disturbances

Three simulations were run from initial conditions with energy in both the oblique $(1, \pm 1)$ modes and the streamwise $(0, 1)$ mode. The first, OBST1, was begun from the same initial condition as OBLIN for the oblique modes and enough energy in the $(0, 1)$ mode to result in zero streamwise vorticity in the MP. The initial streamwise vorticity distribution for this case thus has maximum amplitude in the roller core, is zero in the MP, and has the same sign in x at any given z-location. The initial disturbances in OBST2 were phased to produce maximum streamwise vorticity in the MP and zero streamwise vorticity in the mid-roller. Again, streamwise vorticity at a given z-location has the same sign in x. This phasing results from combining the STI disturbance used for OBST1 with the negative of the OBLIN initial condition. Finally, OBST3 combines the initial disturbances used in OBLOUT with the same $(0, 1)$ mode disturbance used in the other OBST simulations. The result is an initial ω_x distribution that is zero at $x = \lambda_x/4$, of maximum amplitude at $x = 3\lambda_x/4$, and at the same intermediate level in both the mid-braid region and the roller core.

All three simulations lead to flows that are similar to the typical flow evolution described in section 4.2. This is perhaps expected of OBST2, which was begun from an initial condition that combined disturbances that both led to the typical evolution by themselves. The initial condition for OBST1 also consisted of a combination of initial disturbances that individually lead to the typical evolution. However, since the initial condition had no streamwise vorticity in the mid-braid plane, it might be thought that the evolution would be more like that of OBLOUT (which also initially has $\Gamma_x^{\mathrm{MP}} = 0$). The fact that OBST3 also evolves typically implies that roughly equal energy in the STI (typical) and OBLOUT (atypical) modes in the initial condition leads to domination by the typical behavior. Addition of ω_y to the initial condition does not significantly alter the flow evolution.

Unlike most of the other simulations described so far, which have two flow symmetries, the OBST3 flow exhibits only one.[21] This is because the point-reflection symmetry points for the OBLOUT and STI (i.e., ROLLUP) disturbances are at different locations; thus, their combination does not possess any point-reflection symmetry. The spanwise plane-reflection symmetry is still present, however. In the absence of a point-reflection symmetry point at the $y = 0$ mid-braid location in the RP, the rib midpoints are not constrained to remain at the quarter-domain locations as in the ROLLUP and OBLIN simulations. The ribs in the OBST3 simulation do not move all the way to the boundary as they do in OBLOUT and do not remain at the quarter-domain locations as in ROLLUP. Instead, they move partway toward the domain boundary, but continue to develop "typically." This results in $-/+$ rib pairs (again, as one moves in the positive z-direction) and is similar to the rib structure of the wake flows described in section 4.3.7 and the OBLMID flow of section 4.4.3, where the point-reflection symmetry was also broken. For the relative STI/oblique mode energies used in OBST3, the effect is small, the spacing between rib pairs being only about 25% larger than the distance between the ribs. Presumably, increasing the initial oblique energy while using the same initial STI energy (i.e., approaching the OBLOUT flow) would increase this number until, as in OBLOUT, healthy ribs could no longer be sustained.

---

[21] The other single symmetry flows were discussed in sections 4.3.7 and 4.4.3, in which the point-reflection symmetry (eq. (11)) is broken, and in section 4.4.4, in which there is no plane-reflection symmetry (eq. (10)).

5 SUMMARY AND DISCUSSION

The simulations described in sections 3 and 4 provide a detailed description of the evolution of a plane mixing layer through the first Kelvin–Helmholtz roll-up. The results are also relevant to forced experimental mixing layers, where pairing is suppressed. In this section, the results are briefly summarized, and inferences that can be made from these results are discussed.

As discussed in section 2.1, the simulations presented here are of a temporally evolving mixing layer, though spatially developing layers are more usual and of greater technological relevance. The temporally evolving layer was selected because of its computational advantages and because it provides a simpler model for the evolution of the plane mixing layer and yet exhibits the same vortex dynamics as the spatially evolving case (Buell, Moser, and Rogers, to appear). In particular, the temporally evolving mixing layer supports two symmetries, one of which is not present in the spatially developing flow. These symmetries make the analysis of the results in section 4 considerably simpler by allowing the unambiguous definition of the rib circulation and the precise definition of the rib-vortex position. Furthermore, even when the symmetries are broken (secs. 4.3.7, 4.4.3), the same flow structures result. Thus, the inferences to be drawn in the following paragraphs should also be applicable to spatially developing mixing layers.

It is known that the plane mixing layer is sensitive to initial (or inlet) conditions. Unfortunately, there is little detailed experimental information available about the inlet conditions existing in mixing-layer facilities. The simulations reported in the previous sections used deterministic low-wavenumber disturbances chosen to mimic those *expected* in experimental mixing layers. These include the two-dimensional "roll-up" disturbance and streamwise invariant (STI) vorticity disturbances. In addition, the disturbances were selected because they lead to the types of structures commonly observed in experimental mixing layers (spanwise rollers and streamwise ribs).[22] It was found that the dynamics of the evolution of the mixing layer were insensitive to reasonable variations in many of the parameters describing these initial disturbances (e.g., functional form in y, wavelength, and initial amplitude of the disturbance; the initialization of different vorticity components; and the presence of a wake in the initial velocity profile).

5.1 Typical Evolution

Despite the fact that the details of the mixing-layer evolution are sensitive to the initial condition chosen, a large number of simulations, begun from different initial conditions, exhibit a "typical evolution." In agreement with many experimental observations (e.g., Breidenthal 1981; Bernal and Roshko 1986; Lasheras, Cho, and Maxworthy 1986; Lasheras and Choi 1988), such flows develop a corrugated spanwise roller and predominately streamwise rib vortices. By the completion of the Kelvin–Helmholtz roll-up (τ_r), the vorticity in the rib vortices is collapsing in the sense of Lin and Corcos (1984) into compact, nearly circular vortices (see τ_c in table 2 and fig. 13(b)). The vortex lines that connect the ribs are kinked in the same direction as the initial perturbation. However, the roller vortex lines are bent in the opposite direction. Because of this, the streamwise and normal vorticity located in the roller

---

[22] Note that long-wavelength phenomena, for example, dislocations (Browand and Troutt 1980), are not studied here.

has the opposite sign of that in the ribs at the same spanwise location. At the "bends" of the corrugated spanwise roller, cup-shaped regions of intense spanwise vorticity form. These cups are created by vortex stretching resulting from the strain field produced by the bent roller and the rib vortices. The opposite sense of bending in the ribs and the roller is critical to forming the strain field that produces the cups. These cups alternate from the top to the bottom of the layer in the spanwise direction and exhibit peak vorticity levels that can be over 5 times the peak vorticity level of the initial mean profile. The spanwise roller is thus highly three-dimensional. The strong three-dimensionality of the rollers has important consequences for the development of the flow during a pairing (it leads to small-scale transition, as will be shown in Part 2).

The vortex lines of a rib connect to neighboring ribs of opposite-sign vorticity through a wisp of diffuse spanwise vorticity between the ribs. This wisp is on the opposite side of the layer from the cups, well removed from the main roller vorticity. Wisp vorticity and consequently the rib vortex lines do not get drawn into the main roller; instead, they are convected over the roller into the next braid region. This lack of connection between the roller and rib vortex lines is contrary to the speculated interaction of the ribs and rollers (Hussain 1983; Bernal and Roshko 1986; Lasheras and Choi 1988). Entry of wisp vorticity and rib vortex lines into the neighboring braid regions is largely responsible for the sudden increase in rib circulation that occurs in these flows. However, in these single roll-up simulations, this is a consequence of oversaturation. When a pairing is allowed (see Part 2), a similar phenomenon occurs, but the details are different. As the rib vortex lines are drawn over the roller, they become convoluted. Typically, they become horseshoe-shaped at the tips, creating regions of spanwise vorticity opposite in sign to that of the initial mean profile; they may become twisted or helical as well. This development of opposite-signed spanwise vorticity is one indicator of a highly three-dimensional layer with collapsed ribs.

Because of the ribs, the typical three-dimensional flow spreads more rapidly, particularly at late times, than the two-dimensional layer. The ultimate state of these flows is very three-dimensional (even though begun from weak three-dimensional disturbances), and the three-dimensional Fourier mode amplitudes overtake the two-dimensional fundamental amplitude in the oversaturated state (after τ_O).

5.2 Sensitivity to Initial Conditions

Although the mixing-layer evolution discussed above is insensitive to variations of many initial condition parameters, there were simulations that exhibited qualitatively different behavior. One of the initial parameters that can affect such changes is the circulation of the streamwise vorticity disturbance. When the circulation is too low (the LOROLL simulation, sec. 4.3.1), the rib vortices do not collapse in the sense of Lin and Corcos (1984). Such uncollapsed vortices do not induce a significant distortion of the passive scalar contours and therefore cannot be responsible for the mushroom-shaped patterns observed in flow-visualization experiments (e.g., Bernal and Roshko 1986). Thus, experiments that exhibit these mushrooms must have large enough rib circulations to produce collapsed vortices. In experiments in which flow visualization does not indicate the presence of rib vortices (e.g., Thorpe 1971, 1985; some flows in Lasheras, Cho, and Maxworthy 1986), noncollapsed vortices may, in fact, be present. The circulation required to produce collapsed ribs is well predicted by the Lin and Corcos (1984) collapse criterion.

Results presented in section 4.3.1 indicate that the circulation attained by the ribs depends on the strength of the initial three-dimensional disturbance. This is because initially (before τ_0), the circulation can grow only until the spanwise vorticity is depleted from the braid region, thus limiting the growth in circulation. This dependence of the late-time rib strength on the initial disturbance amplitude is contrary to the concept of an instability, in which one expects the saturated state to be independent of the initial disturbance strength (see sec. 5.3).

Very large initial three-dimensional disturbances also produce qualitatively different flow evolutions (HIROLL, sec. 4.3.1). In this case, the rib vortices have complicated internal dynamics, and the roller core is more complex than the simple cup structures. This leads to an apparently turbulent state at late time. Further, the rib vortices are larger in diameter and produce scalar mushroom patterns that are more pronounced and fatter. It is not clear if these differences in the scalar mushroom pattern would be clearly discernible in flow visualizations. If they were, one could bound from above the circulations present in experiments. Thus, we tentatively conclude that the rib circulations present in the experiments cited here are of the same order as the plateau level in our baseline (ROLLUP) simulation (within a factor of 4). This range of circulations ($0.018\Gamma_z$ to $0.3\Gamma_z$) covers the early-development circulation estimates of $0.07\Gamma_z$ and $0.1\Gamma_z$ by Bell and Mehta (1990) and Jimenez (1983), respectively. Note that Jimenez (1983) and Jimenez, Cogollos, and Bernal (1985) are widely quoted as having circulation levels of order Γ_z, but this is for the late stages of development (after several pairings and mixing transition).

As an obvious extension to the STI vorticity disturbance discussed above, oblique Fourier modes were also used. Such disturbances are relevant because they develop rapidly from the STI modes interacting with the two-dimensional roll-up, and because they are suggested by the linear stability studies of Pierrehumbert and Widnall (1982). Except in one special case, flows with such disturbances, or with such disturbances combined with STI modes, also evolve according to the standard scenario followed by the STI cases (see secs. 4.4.1, 4.4.3, 4.5). The most notable exception is a particular phasing of the oblique modes relative to the two-dimensional fundamental (OBLOUT, sec. 4.4.2). Pierrehumbert and Widnall (1982) referred to this type of disturbance as the "bulging" mode and found it to have no appreciable instability.

In OBLOUT, the streamwise vorticity circulation at the mid-braid location is identically zero for all time. An antisymmetric double-rib structure forms initially in the rib plane (RP), but is convected by its own self-induced motion toward another double-rib structure of opposite sign. The resulting quadrupole is held in place by the compressive component of the roller strain field and eventually is viscously destroyed. The roller behavior for this case is also different. Cuplike structures form on both sides of the layer at the same spanwise location and eventually coalesce to form a hoop of spanwise vorticity with a nearly irrotational core. This "hooped" roller then undergoes a quasi-periodic standing oscillation whereby hoops are destroyed and re-formed at locations halfway between the original hoops by strong vortex stretching.

This atypical evolution has not been observed experimentally. There are two possible explanations for this. First, the OBLOUT case appears to be a singular case; that is, if other modes (e.g., STI modes) are present, or if the phasing is not sufficiently close to that of OBLOUT, then the standard evolution occurs. Thus, experiments would be unlikely to have inlet conditions that would lead to the OBLOUT evolution. Second, even if this atypical evolution were to occur in experimental mixing layers, it would probably be difficult to detect by the standard flow-visualization techniques.

5.3 Instability Mechanisms

It is instructive to see how well previous theoretical predictions and experimental inferences agree with the results presented here. The most widely cited results on the secondary instability of mixing layers are those of Pierrehumbert and Widnall (1982). Pierrehumbert and Widnall found the unstable three-dimensional eigenmodes of a two-dimensional time-independent base flow (Stuart (1967) vortices). For linear disturbances of the type discussed here, they found that the flow was unstable to a "translative" instability. The strength of the instability is only weakly dependent on the spanwise wavelength. Also, visualizations of the spanwise vorticity of the eigenfunction (see their fig. 8) can be interpreted as the kinking of the spanwise roller and, in light of the current results, the beginning of cup formation. Pierrehumbert and Widnall do not show the streamwise vorticity of the eigenfunction, so we have repeated their calculation using the standard wavelengths reported here ($\lambda_x = 1.16(2\pi)$, $\lambda_z = 0.6\lambda_x$) with their choice of the Stuart vortex-core size parameter ($\rho = 0.25$ in their notation, see their eq. 1). This value of the core-size parameter was found by Browand and Weidman (1976) to give a reasonable representation of ensemble-averaged experimental roller-core vorticity distributions. Our computations yielded the same growth rates as those of Pierrehumbert and Widnall. The eigenfunctions do indeed indicate that there are rib vortices with vortex lines kinked opposite to those in the core. However, there is a problem with these computed eigenfunctions (both ours and those of Pierrehumbert and Widnall). An analysis of the stability equations near the symmetry point in the middle of the ribs suggests that the streamwise and cross-stream vorticity of the eigenfunction are singular there. Such a singularity makes it impossible to represent the eigenfunction accurately with the spectral numerical methods used here and by Pierrehumbert and Widnall. Fortunately, resolution sufficient to accurately represent the base flow (the Stuart vortices) is adequate to obtain a good approximation to the eigenvalue, regardless of how poorly the eigenfunction is resolved. This is reflected in the fact that the eigenvalues computed here and by Pierrehumbert and Widnall agree, though the current computations had 16 times better resolution in both coordinate directions. Another difficulty with these stability computations is that the Stuart vortices are not a good approximation to a rolling-up mixing layer (they have too much vorticity in the braid region, as also noted by Browand and Weidman (1976)), and they do not evolve in time as a mixing layer does.

These problems associated with the stability analysis of Pierrehumbert and Widnall were avoided in the linear perturbation computations performed by Corcos and Lin (1984). In their computations, three-dimensional infinitesimal disturbances were allowed to evolve in the presence of a rolling-up two-dimensional mixing layer at finite Reynolds number. The initial conditions were similar to those used in our OBLIN simulation (sec. 4.4.1), and the Reynolds number as defined here was 100. The calculations of Corcos and Lin show that by the time the mixing layer has rolled up, the three-dimensional perturbation exhibits the bending core characteristic of the translative instability, as well as rib vortices in the braid region. We have performed a similar calculation using parameters and initial perturbations identical to the STI disturbance cases reported in sections 4.2 and 4.3.1, except that an infinitesimal amplitude was used for the three-dimensional disturbance. This calculation can, therefore, be directly compared with the ROLLUP, LOROLL, and HIROLL simulations. Contour plots of the infinitesimal-perturbation streamwise vorticity in the RP and the roller core plane (CP) are shown in figure 51. These should be compared to figures 11(b) and 17(b) for the ROLLUP simulation. The similarity between the linear perturbation structures and those from ROLLUP is truly remarkable. The only nonlinear effects visible in ROLLUP at this time (τ_r) are the collapsing ribs and the forming cups (visible in the

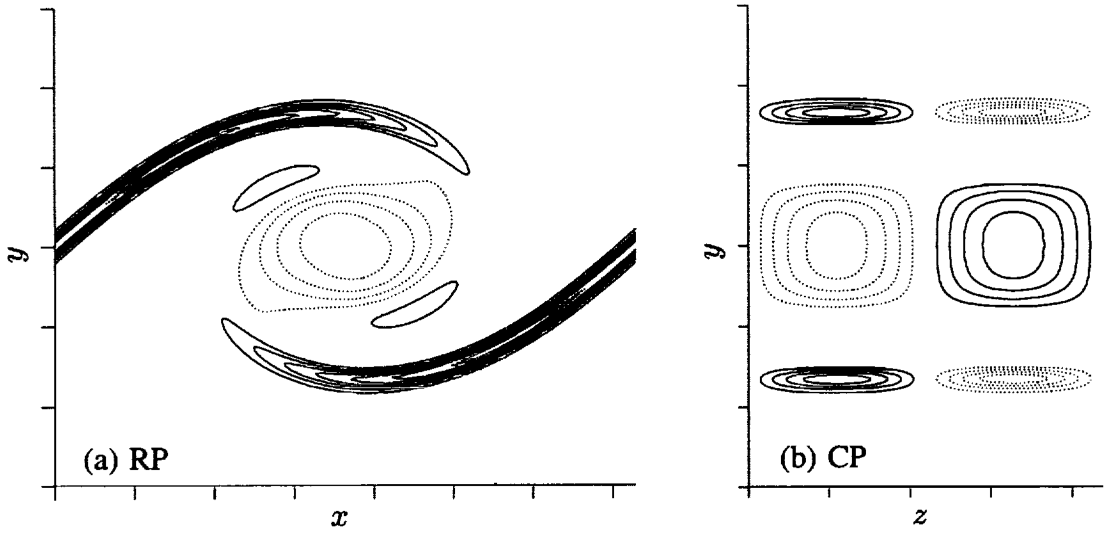

Figure 51. Contour plots of streamwise vorticity in the RP and CP for the three-dimensional linear perturbation at $t = 9.8$ ($\tau_r = 10.1$). The contour increment is $0.4\Gamma_x(t = 0)/\Gamma_r$, where Γ_r is the streamwise circulation (Γ_x) for the ROLLUP case (sec. 4.2) at $t = 0$. Note that this scaling makes (a) and (b) exactly comparable to figures 11(b) and 17(b), respectively. Tic marks are at δ_ω^0 intervals.

perturbation spanwise vorticity, not shown). The remaining features (e.g., sub-ribs and the opposite-signed streamwise vorticity in the core) of the linear perturbation are identical to those in ROLLUP. Also, the quadrupoles identified in section 4.2 as the cause of the vortex stretching leading to the "cups" are present in the linear perturbation.

The circulation of the rib vortices is an important measure of the three-dimensionality of the flow. The evolution of this circulation for the linear perturbation discussed above is shown in figure 52(a) along with that for the three directly comparable cases. In ROLLUP, the evolution of the circulation is consistent with linear theory until τ_o. This is consistent with the observations in section 4.2 that the evolution is governed by the removal of spanwise vorticity from the braid region, an essentially two-dimensional process. In LOROLL the circulation evolves according to linear theory even after τ_o, and in HIROLL the evolution is nonlinear before τ_r. The occurrence of the plateau in circulation of the linear perturbation before τ_o suggests that the energy in the three-dimensional perturbation may not be growing at this time. The evolution of the amplitude of the entire three-dimensional perturbation ($A_{3\text{D}} = \sqrt{\sum_i A_{i1}^2}$) and the mid-braid plane (MP) circulation (Γ_x^{MP}) are shown in figure 52(b). The early-time increase in $A_{3\text{D}}$ is associated with the corrugation of the layer's spanwise vorticity by the perturbation streamwise vorticity (this is also the cause of the early-time increase in A_{01} in fig. 7). This corrugation is necessary to support circulation growth (see sec. 4.2.3), and it is only after $A_{3\text{D}}$ has leveled off that the circulation begins to increase. At about $t = 10$ the perturbation amplitude begins to grow again. This time corresponds to that of the initial introduction of new spanwise vorticity into the braid region as indicated by the growth of rib circulation away from the MP (see fig. 14). The growth of $A_{3\text{D}}$ appears to be exponential only for late times. From $t = 10$ to $t = 25$, $A_{3\text{D}}$ and Γ_x^{MP} grow by approximately the same factor, indicating that the ribs are strengthening at a rate commensurate with the rest of the perturbation.

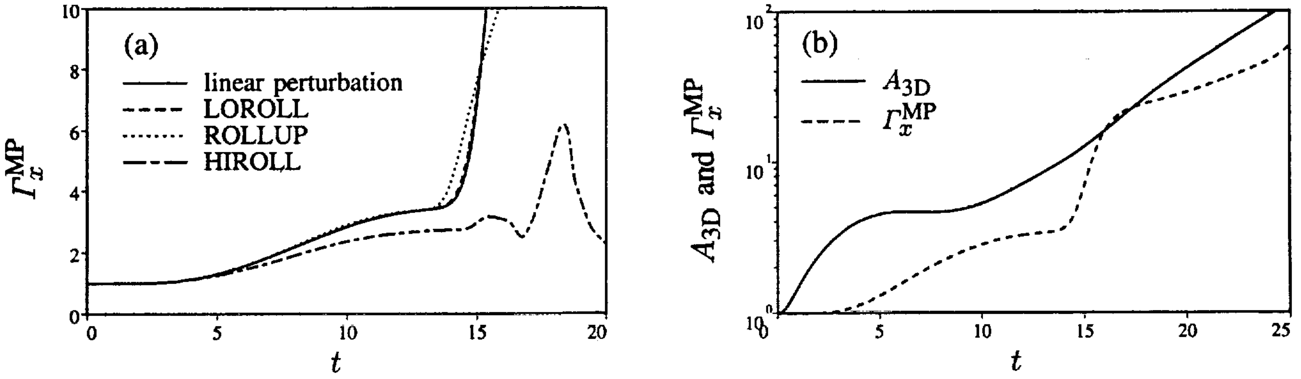

Figure 52. Time development of (a) Γ_x^{MP} of the linear perturbation and nonlinear flows, and (b) $A_{3\mathrm{D}}$ and Γ_x^{MP} of the linear perturbation. All quantities are normalized by their values at $t = 0$.

As pointed out by Corcos and Lin (1984), the analysis of the linear stability of an evolving base flow is more subtle than that for a nonevolving flow. One can safely say that an evolving base flow is unstable if there are linear perturbations that exhibit long-term exponential growth. By this definition, it appears that the translative instability is in fact an instability for this evolving base flow.[23] However, from the discussion above there is a qualitative difference in the behavior of the three-dimensional perturbation before and after τ_o. The perturbations used here are apparently not unstable until roller spanwise vorticity is brought back into the braid region. Some perturbations could also be unstable before this time by another mechanism (e.g., the large-spanwise-wavelength oblique disturbances used by Corcos and Lin). It is the late-time instability of the oversaturated roller that can be identified with the translative instability. This is consistent with the results of Pierrehumbert and Widnall since the Stuart vortices have significant spanwise vorticity in the braid region, like the oversaturated rollers. Note that this was not evident in the calculations of Corcos and Lin, because at low Reynolds numbers the plateau in the circulation evolution does not occur. The identification of the translative instability as an instability of the late-time oversaturated rollers has two important consequences. First, most of the results in section 4 (the presence of cups, behavior of rib vortex lines, etc.) are for times only up to and shortly after τ_o, so little growth caused by the translative instability has occurred for these results. Thus, the degree of three-dimensionality in the flow is determined by the degree of three-dimensionality specified in the initial conditions. Second, as will be seen in Part 2, pairing of the rollers delays oversaturation and the associated return of spanwise vorticity to the braid region. Pairing is therefore expected to delay the onset of the translative instability. This is in part responsible for the observed "suppression" of three-dimensionality by pairing (Corcos and Lin 1984; Metcalfe et al. 1987).

Both Pierrehumbert and Widnall, and Corcos and Lin (1984) observed that the three-dimensional perturbation energy was concentrated in the spanwise roller. This led them to speculate that the translative instability was in essence an instability of the roller core. Corcos and Lin state that "it is likely that the strong streamwise vorticity that appears and persists in the central part of the braids . . . is caused early on by the original shear instability rather than the translative instability, and thereafter leads a fossil life." Following this reasoning, various researchers have interpreted their experiments or computations as evidence of a core instability (e.g., Nygaard and Glezer 1990), or alternatively, as a braid instability (e.g., Ashurst and Meiburg 1988; Lasheras and Choi 1988; Bell and Mehta 1989b). The term "braid

---

[23] However, the flow-evolution time studied here is limited, so one could argue this point.

instability" is usually used in reference to the mechanism investigated by Lin and Corcos (1984), by which the rib vortices collapse (see sec. 4.3.1). It is clear from the results presented here that this distinction (or perhaps controversy) between two "instability" mechanisms is unfounded. The energy in the perturbation is concentrated in the core, but the exponential growth of the perturbation appears to occur only as spanwise vorticity is brought back into the braid region, allowing the rib circulation to grow. Further, as discussed in section 4.2.4, the presence of the rib vortices is required to form the quadrupole in the roller core, which leads to the growth of three-dimensionality in the core. Thus, the description of the translative instability as an instability of the roller is incomplete. On the other hand, identification of the Lin and Corcos collapse mechanism with a braid instability is not appropriate (they do not make such an association). The growth of the rib vortices requires the introduction of three-dimensional spanwise vorticity into the braid region from the roller, because an array of vortices in a plane strain field is not in itself unstable. Collapse of the vortices is a nonlinear process that does not increase their strength. The translative instability must therefore be viewed as an instability of the two-dimensional mixing layer as a whole (rollers and braids).

6 CONCLUSIONS

The evolution of three-dimensional, temporally evolving, plane mixing layers starting from "clean" initial perturbations and progressing through the first Kelvin–Helmholtz roll-up has been studied by direct numerical simulation. The "ribs" and "rollers" observed in experiments were found to be associated with a "typical" evolution of the layer, and their interaction has been studied in detail. New vortical structures, here referred to as "cups," "hoops," and "wisps," have been identified in the simulations as well. The sensitivity of the mixing layer to changes in initial conditions has been studied by varying the inital condition parameters, and this has resulted in an understanding of the variability of the vortex structures. This, in turn, provides a basis for speculation about the nature and strength of the disturbances present in experimental mixing layers.

The origin of the typical vortex structures can be understood by examining the linear evolution of a three-dimensional perturbation on an evolving two-dimensional base flow. Such calculations suggest that the onset of three-dimensionality and the appearance of rib vortices are not the results of either a "braid" instability or a "core instability," as has often been speculated, but rather are a natural consequence of the evolution of the two-dimensional base flow as a whole.

The results presented in sections 5.3 and 4.3.1 demonstrate the remarkable predictive power of two analytical (or quasi-analytical) tools for this flow: the linear perturbation analysis of Corcos and Lin (1984) and the nonlinear streamwise vortex-collapse analysis of Lin and Corcos (1984). The linear perturbation analysis allows one to predict the degree of three-dimensionality and, to a large extent, the structure of the three-dimensionality for flows even into the nonlinear regime. It is used in Part 2 to predict the strength of the rib vortices at the beginning of a pairing. The vortex-collapse analysis of Lin and Corcos (1984) was seen in section 4.3.1 to accurately predict the onset and evolution of one of the important nonlinearities of the three-dimensional flow (i.e., the collapse of the rib vortices).

These tools cannot, however, provide a complete description of the three-dimensionality associated with the early evolution of a mixing layer. In particular, the linear analysis of Corcos and Lin (1984) cannot describe flow behavior that is essentially nonlinear (e.g., the formation of cup vorticity, the evolution of vortex lines, and the collapse of the rib vortices). The rib-vortex collapse is addressed by Lin and Corcos (1984), but their analysis cannot predict the circulation growth observed in the oversaturated state, the deformation of the rib vortices observed here, or the interaction of the ribs with the rollers. The insights obtained from the numerical results presented here, supplemented by the analytical models, provide a comprehensive understanding of the evolution of the plane mixing layer in the absence of pairing. In Part 2, knowledge of this early mixing-layer evolution will be critical to understanding pairing and the transition to turbulence.

REFERENCES

Acton, E.: The Modelling of Large Eddies in a Two-Dimensional Shear Layer. J. Fluid Mech., vol. 76, 1976, pp. 561–592.

Ashurst, W. T.; and Meiburg, E.: Three-Dimensional Shear Layers via Vortex Dynamics. J. Fluid Mech., vol. 189, 1988, pp. 87–116.

Bell, J. H.; and Mehta, R. D.: Three-Dimensional Structure of a Plane Mixing Layer. AIAA Paper 89-0124, 1989a.

Bell, J. H.; and Mehta, R. D.: Three-Dimensional Structure of Plane Mixing Layers. JIAA TR-90, Dept. Aeronaut. and Astronaut., Stanford Univ., Stanford, Calif., 1989b.

Bell, J. H.; and Mehta, R. D.: Effects of Streamwise Vorticity Injection on Turbulent Mixing Layer Development. AIAA Paper 90-1459, 1990.

Bernal, L. P.: The Coherent Structure of Turbulent Mixing Layers. Ph.D. thesis, California Institute of Technology, Pasadena, Calif., 1981.

Bernal, L. P.; and Roshko, A.: Streamwise Vortex Structure in Plane Mixing Layers. J. Fluid Mech., vol. 170, 1986, pp. 499–525.

Breidenthal, R.: Structure in Turbulent Mixing Layers and Wakes Using a Chemical Reaction. J. Fluid Mech., vol. 109, 1981, pp. 1–24.

Browand, F. K.; and Troutt, T. R.: A Note on Spanwise Structure in the Two-Dimensional Mixing Layer. J. Fluid Mech., vol. 97, 1980, pp. 771–781.

Browand, F. K.; and Weidman, P. D.: Large Scales in the Developing Mixing Layer. J. Fluid Mech., vol. 76, 1976, pp. 127–144.

Brown, G. L.; and Roshko, A.: The Effect of Density Difference on the Turbulent Mixing Layer. Turbulent Shear Flows, AGARD Conf. Proc. 93, 1971, pp. 23-1–23-11.

Brown, G. L.; and Roshko, A.: On Density Effects and Large Structures in Turbulent Mixing Layers. J. Fluid Mech., vol. 64, 1974, pp. 775–816.

Buell, J. C.; and Huerre, P.: Inflow/Outflow Boundary Conditions and Global Dynamics of Spatial Mixing Layers. CTR-S88, Proc. 1988 Summer Program, Center for Turbulence Research, Stanford Univ., Stanford, Calif., 1988.

Buell, J. C.; and Mansour, N. N.: Asymmetric Effects in Three-Dimensional Spatially Developing Mixing Layers. Proc. Seventh Intl. Symp. on Turbulent Shear Flows, Stanford Univ., Stanford, Calif., 1989a, pp. 9.2.1–9.2.6.

Buell, J. C.; and Mansour, N. N.: Near-Field Structures in Three-Dimensional Spatially Developing Wakes. 10th Australasian Fluid Mech. Conf., Melbourne, 1989b.

Cain, A. B.; Reynolds, W. C.; and Ferziger, J. H.: A Three-Dimensional Simulation of Transition and Early Turbulence in a Time-Developing Mixing Layer. TF-14, Dept. Mech. Eng., Stanford Univ., Stanford, Calif., 1981.

Chandrsuda, C.; Mehta, R. D.; Weir, A. D.; and Bradshaw, P.: Effect of Free-Stream Turbulence on Large Structure in Turbulent Mixing Layers. J. Fluid Mech., vol. 85, 1978, pp. 693–704.

Corcos, G. M.; and Lin, S. J.: The Mixing Layer: Deterministic Models of a Turbulent Flow. Part 2. The Origin of the Three-Dimensional Motion. J. Fluid Mech., vol. 139, 1984, pp. 67–95.

Corcos, G. M.; and Sherman, F. S.: The Mixing Layer: Deterministic Models of a Turbulent Flow. Part 1. Introduction and the Two-Dimensional Flow. J. Fluid Mech., vol. 139, 1984, pp. 29–65.

Ho, C.-M.; and Huang, L.-S.: Subharmonics and Vortex Merging in Mixing Layers. J. Fluid Mech., vol. 119, 1982, pp. 443–473.

Ho, C.-M.; and Huerre, P.: Perturbed Free Shear Layers. Ann. Rev. Fluid Mech., vol. 16, 1984, pp. 365–424.

Ho, C.-M.; Zohar, Y.; Moser, R. D.; Rogers, M. M.; Lele, S. K.; and Buell, J. C.: Phase Decorrelation, Streamwise Vortices and Acoustic Radiation in Mixing Layers. CTR-S88, Proc. 1988 Summer Program, Center for Turbulence Research, Stanford Univ., Stanford, Calif., 1988.

Huang, L.-S.; and Ho, C.-M.: Small-Scale Transition in a Plane Mixing Layer. J. Fluid Mech., vol. 210, 1990, pp. 475–500.

Huerre, P.; and Monkewitz, P. A.: Absolute and Convective Instabilities in Free Shear Layers. J. Fluid Mech., vol. 159, 1985, pp. 151–168.

Hussain, A. K. M. F.: Coherent Structures and Incoherent Turbulence. Turbulence and Chaotic Phenomena in Fluids, T. Tatsumi, ed., North-Holland, 1983, pp. 453–460.

Jimenez, J.: A Spanwise Structure in the Plane Shear Layer. J. Fluid Mech., vol. 132, 1983, pp. 319–336.

Jimenez, J.; Cogollos, M.; and Bernal, L. P.: A Perspective View of the Plane Mixing Layer. J. Fluid Mech., vol. 152, 1985, pp. 125–143.

Kelly, R. E.: On the Stability of an Inviscid Shear Layer which is Periodic in Space and Time. J. Fluid Mech., vol. 27, 1967, pp. 657–689.

Konrad, J. H.: An Experimental Investigation of Mixing in Two-Dimensional Turbulent Shear Flows with Applications to Diffusion-Limited Chemical Reactions. Internal Report CIT-8-PU, California Institute of Technology, Pasadena, Calif., 1976.

Lasheras, J. C.; Cho, J. S.; and Maxworthy, T.: On the Origin and Evolution of Streamwise Vortical Structures in a Plane, Free Shear Layer. J. Fluid Mech., vol. 172, 1986, pp. 231–258.

Lasheras, J. C.; and Choi, H.: Three-Dimensional Instability of a Plane Free Shear Layer: An Experimental Study of the Formation and Evolution of Streamwise Vortices. J. Fluid Mech., vol. 189, 1988, pp. 53–86.

Lin, S. J.; and Corcos, G. M.: The Mixing Layer: Deterministic Models of a Turbulent Flow. Part 3. The Effect of Plane Strain on the Dynamics of Streamwise Vortices. J. Fluid Mech., vol. 141, 1984, pp. 139–178.

Lowery, P. S.; and Reynolds, W. C.: Numerical Simulation of a Spatially Developing, Forced, Plane Mixing Layer. TF-26, Dept. Mech. Eng., Stanford Univ., Stanford, Calif., 1986.

Mansour, N. N.; Ferziger, J. H.; and Reynolds, W. C.: Large-Eddy Simulation of a Turbulent Mixing Layer. TF-11, Dept. Mech. Eng., Stanford Univ., Stanford, Calif., 1978.

Metcalfe, R. W.; Orszag, S. A.; Brachet, M. E.; Menon, S.; and Riley, J. J.: Secondary Instability of a Temporally Growing Mixing Layer. J. Fluid Mech., vol. 184, 1987, pp. 207–243.

Michalke, A.: On the Inviscid Instability of the Hyperbolic-Tangent Velocity Profile. J. Fluid Mech., vol. 19, 1964, pp. 543–556.

Moin, P.; Leonard, A.; and Kim, J.: Evolution of a Curved Vortex Filament into a Vortex Ring. Phys. Fluids, vol. 29, 1986, pp. 955–963.

Monkewitz, P. A.: Subharmonic Resonance, Pairing and Shredding in the Mixing Layer. J. Fluid Mech., vol. 188, 1988, pp. 223–252.

Monkewitz, P. A.; and Huerre, P.: Influence of the Velocity Ratio on the Spatial Instability of Mixing Layers. Phys. Fluids, vol. 25, 1982, pp. 1137–1143.

Moser, R. D.; and Rogers, M. M.: Mixing Transition and the Cascade to Small Scales in a Plane Mixing Layer. Phys. Fluids A, vol. 3, 1991, pp. 1128–1134.

Neu, J.: The Dynamics of Stretched Vortices. J. Fluid Mech., vol. 143, 1984, pp. 253–276.

Nygaard, K. J.; and Glezer, A.: Core Instability of the Spanwise Vortices in a Plane Mixing Layer. Phys. Fluids, vol. 2, 1990, pp. 461–464.

Patnaik, P. C.; Sherman, F. S.; and Corcos, G. M.: A Numerical Simulation of Kelvin–Helmholtz Waves of Finite Amplitude. J. Fluid Mech., vol. 73, 1976, pp. 215–240.

Pierrehumbert, R. T.; and Widnall, S. E.: The Two- and Three-Dimensional Instabilities of a Spatially Periodic Shear Layer. J. Fluid Mech., vol. 114, 1982, pp. 59–82.

Pullin, D. I.; and Jacobs, P. A.: Inviscid Evolution of Stretched Vortex Arrays. J. Fluid Mech., vol. 171, 1986, pp. 377–406.

Riley, J. J.; and Metcalfe, R. W.: Direct Numerical Simulation of a Perturbed Turbulent Mixing Layer. AIAA Paper 80-0274, 1980.

Rogers, M. M.; Ho, C. M.; Zohar, Y.; and Moser, R. D.: Evolution of Mixing Layers with a Spanwise Thickness Variation. Bull. Amer. Phys. Soc., vol. 33, 1988, p. 2274.

Rogers, M. M.; and Moser, R. D.: The Development of Three-Dimensional Temporally Evolving Mixing Layers. Proc. Seventh Intl. Symp. on Turbulent Shear Flows, Stanford Univ., Stanford, Calif., 1989, pp. 9.3.1–9.3.6.

Sandham, N. D.; and Reynolds, W. C.: Some Inlet Plane Effects on the Numerically Simulated Spatially Developing Two-Dimensional Mixing Layer. Turbulent Shear Flows 6: Sixth Intl. Symp. on Turbulent Shear Flows, Toulouse, 1987, pp. 22.4.1–22.4.6.

Spalart, P. R.; Moser, R. D.; and Rogers, M. M.: Spectral Methods for the Navier–Stokes Equations with One Infinite and Two Periodic Directions. J. Comp. Phys., vol. 96, 1991, pp. 297–324.

Stuart, J. T.: On Finite Amplitude Oscillations in Laminar Mixing Layers. J. Fluid Mech., vol. 29, 1967, pp. 417–440.

Thorpe, S. A.: A Method of Producing a Shear Flow in a Stratified Fluid. J. Fluid Mech., vol. 32, 1968, pp. 693–704.

Thorpe, S. A.: Experiments on the Instability of Stratified Shear Flows: Miscible Fluids. J. Fluid Mech., vol. 46, 1971, pp. 299–319.

Thorpe, S. A.: Experiments on Instability and Turbulence in a Stratified Shear Flow. J. Fluid Mech., vol. 61, 1973, pp. 731–751.

Thorpe, S. A.: Laboratory Observations of Secondary Structures in Kelvin–Helmholtz Billows and Consequences for Ocean Mixing. Geophys. Astrophys. Fluid Dynamics, vol. 34, 1985, pp. 175–199.

Turner, J. S.: Buoyancy Effects in Fluids. Cambridge University Press, 1973.

Winant, C. D.; and Browand, F. K.: Vortex Pairing: The Mechanism of Turbulent Mixing-Layer Growth at Moderate Reynolds Number. J. Fluid Mech., vol. 63, 1974, pp. 237–255.

REPORT DOCUMENTATION PAGE

Form Approved
OMB No. 0704-0188

1. AGENCY USE ONLY *(Leave blank)*	**2. REPORT DATE** September 1991	**3. REPORT TYPE AND DATES COVERED** Technical Memorandum

4. TITLE AND SUBTITLE

The Three-Dimensional Evolution of a Plane Mixing Layer
Part 1. The Kelvin-Helmholtz Roll-Up

5. FUNDING NUMBERS

6. AUTHOR(S)

Michael M. Rogers and Robert D. Moser

7. PERFORMING ORGANIZATION NAME(S) AND ADDRESS(ES)

Ames Research Center
Moffett Field, CA 94035-1000

8. PERFORMING ORGANIZATION REPORT NUMBER

A-91115

9. SPONSORING/MONITORING AGENCY NAME(S) AND ADDRESS(ES)

National Aeronautics and Space Administration
Washington, DC 20546-0001

10. SPONSORING/MONITORING AGENCY REPORT NUMBER

NASA TM-103856

11. SUPPLEMENTARY NOTES

Point of Contact: Michael M. Rogers, Ames Research Center, MS 202A-1, Moffett Field, CA 94035-1000;
(415) 604-4732 or FTS 464-4732

12a. DISTRIBUTION/AVAILABILITY STATEMENT

Unclassified — Unlimited
Subject Category 34

12b. DISTRIBUTION CODE

13. ABSTRACT *(Maximum 200 words)*

The Kelvin-Helmholtz roll-up of three-dimensional, temporally evolving, plane mixing layers has been simulated numerically. All simulations were begun from a few low-wavenumber disturbances, usually derived from linear stability theory, in addition to the mean velocity profile. The spanwise disturbance wavelength was taken to be less than or equal to the streamwise wavelength associated with the Kelvin-Helmholtz roll-up. A standard set of "clean" structures develop in most of the simulations. The spanwise vorticity rolls up into a corrugated spanwise roller, with vortex stretching creating strong spanwise vorticity in a cup-shaped region at the bends of the roller. Predominantly streamwise rib vortices develop in the braid region between the rollers. For sufficiently strong initial three-dimensional disturbances, these ribs "collapse" into compact axisymmetric vortices. The rib vortex lines connect to neighboring ribs and are kinked in the opposite direction of the roller vortex lines. Because of this, these two sets of vortex lines remain distinct. For certain initial conditions, persistent ribs do not develop. In such cases the development of significant three-dimensionality is delayed. When the initial three-dimensional disturbance energy is about equal to, or less than, the two-dimensional fundamental disturbance energy, the evolution of the three-dimensional disturbance is nearly linear (with respect to the mean and the two-dimensional disturbances), at least until the first Kelvin-Helmholtz roll-up is completed. This includes cases in which the three-dimensional disturbance is strong enough to result in "collapsed" rib vortices of the type visualized in experiments. Because of this, the evolution of infinitesimal three-dimensional perturbations on the developing two-dimensional base flow contains many of the same features present in the full three-dimensional simulations. Nonlinear effects are important in the rib collapse process, in the generation of the strong cup vorticity at the bends of the roller, and late in the flow evolution after the two-dimensional modes have saturated. The appearance of collapsed rib vortices and strong cup vorticity will be shown in Part 2 of this report (to be published as a NASA TM) to be the first step in the transition to turbulence.

14. SUBJECT TERMS

Mixing layers

15. NUMBER OF PAGES

86

16. PRICE CODE

A05

17. SECURITY CLASSIFICATION OF REPORT Unclassified	**18. SECURITY CLASSIFICATION OF THIS PAGE** Unclassified	**19. SECURITY CLASSIFICATION OF ABSTRACT**	**20. LIMITATION OF ABSTRACT**